Univerzita Karlova v Praze

Matematicko-fyzikální fakulta

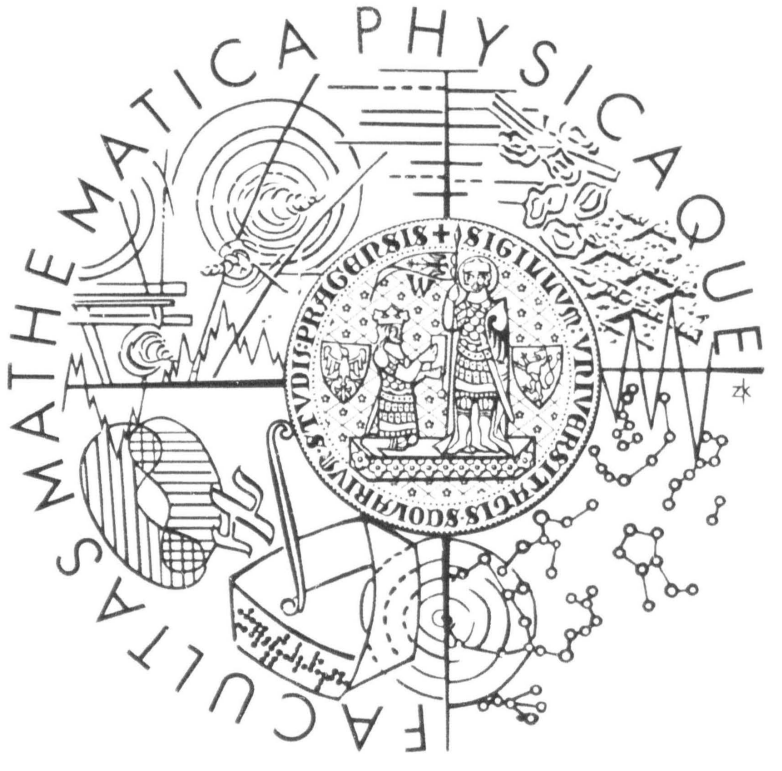

Rigorózní práce

Deformační chování perspektivních hořčíkových a hliníkových slitin

Mgr. Aleš Jäger

Školitel: Prof. RNDr. **Pavel Lukáč**, DrSc.

Oborová rada: F-3: Fyzika kondenzovaných látek a materiálový výzkum

Charles University in Prague

Faculty of Mathematics and Physics

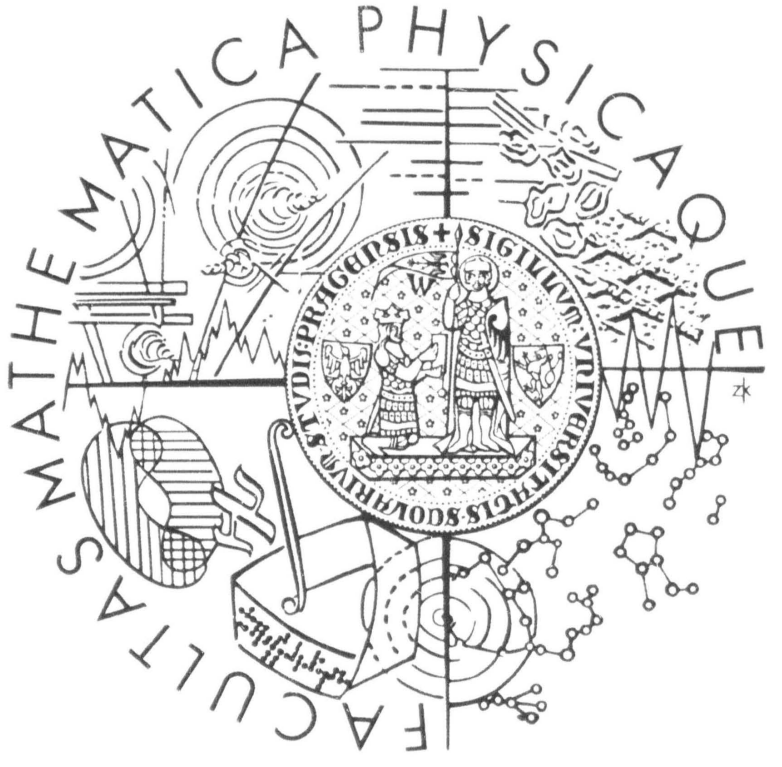

Deformation behaviour of advanced magnesium and aluminium alloys

Mgr. Aleš Jäger

Adviser: Prof. RNDr. **Pavel Lukáč**, DrSc.

Field-of-study board: F-3: Physics of condensed matter and material research

Abstract

Aluminum and magnesium alloys are often considered as promising materials due to high strength/density ratio. In general, light alloys are very attractive structural materials for applications where environmental protection or weight reduction play essential role. Therefore, it is of interest to investigate microstructure and its changes during plastic deformation because it helps to understand the nature of solute effect and processes taking place during plastic deformation. The aim of this work is to reveal microstructures, deformation characteristics and micromechanisms of plastic deformation at different strain rates and temperatures in selected light alloys. Two commercially available alloys were used in this work: AZ31 rolled magnesium alloy and AA6082 extruded aluminium alloy. These alloys were studied with the help of various experimental techniques such as tensile testing, light microscopy, electron backscatter diffraction (EBSD) and X-ray diffraction.

Abstrakt

Hliníkové a hořčíkové slitiny jsou považovány za vysoce perspektivní materiály, protože nabízejí velmi dobrý poměr pevnosti k hustotě. Tyto lehké slitiny nalézají uplatnění především v aplikacích, kde je kladen důraz na ochranu životního prostředí a nebo snížení hmotnosti. Detailní studium jejich mikrostruktury a deformačního chování umožňuje pochopit vliv příměsových atomů a procesů odehrávajících se při plastické deformaci, a vede k systematickému zlepšování vlastností. Cílem této práce je stanovit deformační chování a mikrostrukturu ve vybraných slitinách lehkých kovů a korelovat jejich vztah. Pro tento účel byly zvoleny dvě komerčně dostupné slitiny: válcovaná hořčíková slitina AZ31 a protlačovaná hliníková slitina AA6082. Výzkum byl prováděn s využitím experimentálních technik jakými jsou tahové testy při různých rychlostech a teplotách, optická mikroskopie, difrakce zpětně odražených elektronů a rentgenová difrakce.

Table of content

Abbreviations and symbols

α	Constant
a	Vector of hexagonal lattice
AIP	Ab initio pseudopotential calculations
ARB	Accumulative role bonding
α'	Numerical constant
β	Constant, $\beta=\alpha.n$
b	Burgers vector
bcc	Body centred cubic
c	Vector of hexagonal lattice
$c_{1,2}$	Constant
C_C	Constant in GB diffusion
CDRX	Continuous DRX
c_f	Solute concentration in atomic fractions
C_{NH}	Constant in lattice diffusional creep
CRSS	Critical resolved shear stress
d	Grain size
D	Diffusivity
D_0	Pre-exponential factor
DDRX	Discontinuous DRX
D_gw	Coefficient of diffusion along GB
DRV	Dynamic recovery
DRX	Dynamic recrystallization
ε	True strain
E	Young's modulus
e	Engineering strain
EBSD	Electron backscatter diffraction
ECAE	Equal channel angular extrusion
$\dot{\varepsilon}$	Strain rate
F	Force acting on the specimen
Φ	2Φ is the angle between K_1 and K_2 (or K_1 and K_2)
fcc	Close packed face centred cubic
FWHM	Full width in half of maximum
G	Shear modulus
GB	Grain Boundary
GBS	Grain boundary sliding
GPT	Generalized pseudopotential theory
η_1 (η_2)	Shear direction (Conjugate direction)
HAB	High Angle Boundary
hcp	Close packed hexagonal
ϑ	Coefficient of hardening

K_1 (K_2)	Twinning plane (Conjugate plane)
k	Boltzmann constant
k_i	i=number or letter: constant, factor
K_2	Plane specifying the only section which remain after twins transformation circular
l	Length of crystal
LAB	Low Angle Boundary
LM	Light microscopy
LMTO	linear muffin-tin orbitals
m	Strain rate sensitivity
M	Taylor factor
n	Strain hardening exponent
ND	Normal direction
Ω	Atomic volume
p	Grain size exponent
PD	Plastic deformation
PM	Powder metallurgy
Q (Q_{GB})	Activation energy (Activation energy for GB diffusion)
R	Correlation coefficient
ρ	Density of dislocations
RD	Rolling direction
RE	Rear Earths
ρ_f	Density of forest dislocations
R_m	Molar Gas Constant, R_m=k N_A , N_A is Avogadro's number
rt	Room temperature
σ	True stress
S	Cross section
s	Magnitude of the shear strain
σ_{02}	Yield stress
SEM	Scanning electron microscope
σ_{max}	Maximum stress
SP	Superplasticity, superplastic
S_p	Shear plane
SRX	Static recrystallization
t	Time
T	Temperature in [K] (unless otherwise noted)
τ	Shear stress
TD	Transversal direction
U_t	Toughness
V	Activation volume
w	GB width
X_R	Parameter of recovery
Xv	Recrystallized fraction
Z	Zener-Hollomon parameter

1. An overview of the problematic

1.1. Introduction to magnesium and aluminium alloys

1.1.1. Historical perspective

Magnesium as a new element was already recognised in 1755. But metallic magnesium was first isolated by Sir Humpry Davy in England in 1808 via electrolysis of anhydrous magnesium chloride with a mercury cathode and named according to the Greek word "Magnesia", a district of Thessaly former region of ancient Greece. In fact, the original name suggested by Davy was "magnium" but today magnesium is used [webelements]. In 1852 Robert Bunsen constructed a small laboratory cell for the electrolysis of fused $MgCl_2$ [Polmear94]. Commercial production commenced in Germany in 1886 but had reached only ~10 t worldwide by 1900. This rose to 350 t in 1915 and then jumped to more than 3000 t by the last year of the First World War. In 1920, after the First World War, production falls down to 330 t and increases again under the impetus of the Second World War in the first of 1940' (32000 t in 1939) [Polmear94]. In 1943 the production reaches ~240000 t [Kammer00 (p.22)]. At the end of the wartime, the production declines again to ~30000 t in the late 1940'.

Nowadays, worldwide production of raw magnesium is reported to be about 600000 tons per year [Aghion06]. Diagram of magnesium consumption in Western world is depicted in **Fig. 1.1**.

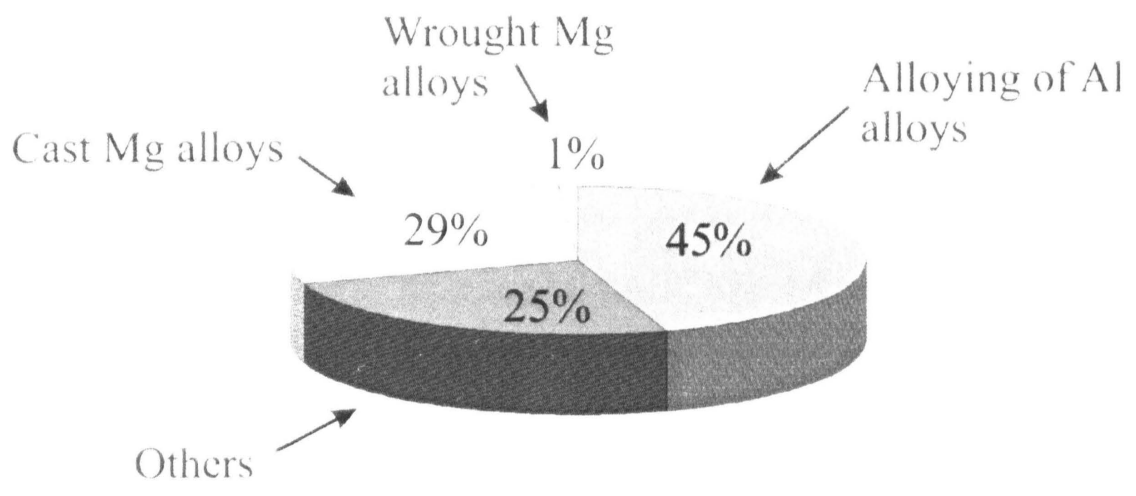

***Fig. 1.1**: Consumption of Mg in Western world in 1997 [Avedesian99 (p.5)].*

In contrast, primary production of Al is about two orders of magnitude higher [Polmear96, Aghion06]. In many cases, both aluminium and magnesium are commonly added to each other as alloying elements. Aluminium is the most common constituent of Mg alloys and, similarly, Mg is one of the most common elements in both wrought and cast Al alloys [ASMAluminum94 (pp.41-45, 91].

The history of aluminium containing compounds is dated as early as the ancient Greek and Roma where alum was used in medicine. In 1761 de Morveau proposed the name "alumine" for the base in alum and, later the name "aluminium" has been adopted. Aluminium metal was isolated in 1825 by Hans Christian Oersted in Denmark [webelements].

1.1.2. Advantages of magnesium and aluminium alloys

One of the most attractive properties of Mg and Al is their lower density and comparable specific strength (strength to density ratio) to iron based alloys. The density of Mg and Al based alloys is usually less than 2000 kg/m^3 and 3000 kg/m^3, respectively. Abundant resources of Mg are available from the see water (~1 kg/m^3) which is environmentally favourable. Moreover, Mg is fully recyclable. Advantages of Al in comparison with Mg are excellent forming capacities and better corrosion resistance. On the other hand, Mg offers better damping capacity and lower weight-of-products due to its lower density. Both metals are easily machinable (magnesium even more easily) with low energetic requirements and long life-time of the tools. The relatively low melting points (650 °C for Mg and 660.5 °C for Al) and specific heat capacities (C_{Mg}= 1020 J/(kg.K) and C_{Al}= 900 J/(kg.K)) insure significantly lower energetic requirements than needed for the melting of iron [wikipedia1, wikipedia2].

1.1.3. Magnesium alloys

Designation of Mg alloys is usually based on the naming method used by American Society for Testing and Materials (ASTM) [Avedesian99 (p.16)]. This method comprises letter-number-letter system which consists of i) code letters (**Tab. 1.1**) indicating the two principal alloying elements, ii) the weight percentage of these two elements and iii) an assigned letter (e.g. X-indicates experimental alloy, C indicates third specific composition registered, etc).

Letter	Element	Letter	Element
A	Aluminium	M	Manganese
C	Cooper	Q	Silver
E	Rear earth metals	S	Silicon
H	Thorium	X	Calcium
J	Strontium	W	Yttrium
K	Zirconium	Z	Zinc
L	Lithium		

***Tab. 1.1**: Code letters for the designation system of magnesium alloys [Avedesian99 (p.18)].*

From "usability" point of view magnesium alloys can be divided into three groups.

Alloys designed for ambient temperatures can be used up to 100-120 °C. In this group we can mainly find Mg-Al-Zn based alloys, which differ in Al and Zn content. Commercially available alloys are designed as AZ91, AZ80 and AZ31, for example. In automotive industry Mg-Al-Mn based alloys are often favoured because of excellent impact properties [Brungs06 (p.253)]; typical examples are AM20 and AM50 varying in Al content.

Alloys for elevated temperatures are based on Mg-Al-Si system. These alloys offer good combination of mechanical properties and production costs up to 150 °C. Typical examples are AS21 and AS41 alloys used in VW Beetle (e.g. [Polmear96])

Alloys for higher temperatures (up to 250 °C) contain in all cases a mix of rear earth elements (Nd-based mixture prevails at present days), Y, Sr or Sc. Typical examples are QE22 (Mg-Ag-Nd) and WE54 (Mg-Y-Nd). Separation of pure Nd is technologically possible but expensive. This is because chemical properties of all elements are mainly determined by upper electron shell. The lanthanides have upper $5p^6$ shell fully occupied and this shell shields the partially occupied 4f shell (Nd ~ $4f^4$). This results in similar chemical properties of lanthanides and makes problem with their separation. Therefore, a mix of RE with predominant content of Nd or Ce (approx. 80%) is usually used for production of commercially available Mg alloys.

Special subcategory is Mg-Th group. Thorium improves mechanical properties and Mg-Th based alloys are creep resistant up to 350 °C [Polmear94]. However, its low radioactivity (half-live of the most stable isotope ^{232}Th is 10^{10} years, and decay chain ends with an isotope of lead ^{208}Pb [wikipedia3]) makes Mg-Th alloys environmentally inappropriate.

The purpose of alloying elements is shown in **Tab. 1.2** [Avedesian99 (p.15), Mordike06 (p.80)].

Element	Purpose
Aluminium	Improves castability; at least 2% are necessary for successful casting. Al is the most common alloying element in Mg alloys. The excess of Al in Mg forms intermetallic compound $Mg_{17}Al_{12}$.
Zinc	Alloying with Zn offer improvement of mechanical properties (better than Al). Alloys of ZK series are reported to be ones of the strongest Mg alloys for ambient temperatures. High concentration of Zn causes cracking during solidification (i.e. hot shortness). The excess of Zn is able to precipitate.
Manganese	Small amount of Mn (as in case of Mg-Al-Zn alloys) improves corrosion resistance by bonding of heavy impurities (mainly Fe) into relatively harmless compounds. Provided that Mn is used as a main alloying element (e.g. AM20 alloy), high toughness (i.e. resistance to cracking) is observed.
Calcium	Calcium improves creep resistance because of precipitation/segregation at grain boundaries. Greater Ca level adversely affect die-castability due to hot-cracking.
Silver	Silver improves precipitation hardening in Mg-RE alloys during artificial aging.
Neodymium	Neodymium improves mechanical properties at higher temperatures. It is not usually used in Mg alloys containing Al due to formation of very stable Al-RE compounds, e.g. [Zou05]. In some cases, however, it is possible to suppress formation of Nd-Al compounds by controlling of cooling rate.

Lithium	Lightest metallic element. Very good solid solubility in Mg. Beyond solid solubility limit, Li gradually changes the structure of Mg from hcp to bcc. Low corrosion resistance. Li increases ductility but decreases strength.
Cerium	Cerium improves corrosion resistance and mechanical properties at elevated temperatures (up to 200 °C). However, Nd provides better results.
Zirconium	Effective grain refinement. Zr cannot be used in Mg alloys containing Al due to formation of Al-Zr compounds.
Yttrium	Improves mechanical properties at higher temperatures and ductility even at room temperature. Y has relatively high solubility limit in the solid solution of Mg.
Silicon	Increases the fluidity of molten alloy. Improve mechanical properties up to 150 °C. Make relatively hard and stable Mg_2Si intermetallic compounds. Si is practically insoluble in Mg.
Iron	Grain refinement. Strong detrimental influence on the corrosion behaviour. Fe can be eliminated by the addition of Mn.
Strontium	Improves corrosion resistance, creep resistance and tensile properties at elevated temperatures.

***Tab. 1.2**: The meaning of alloying elements in Mg [Avedesian99 (p.15), Mordike06 (p.80)].*

1.1.4. Aluminium alloys

Designation system of Al alloys describes wrought and cast products separately [ASMAluminum94, Kaufman00]. Aluminium alloys are grouped by the alloying element present in the greatest mean percentage as listed in **Tab. 1.3**. The meaning of alloying elements is summarised in [ASMAluminum94].

Pure Al is relatively soft metal with remarkable ductility even at room temperature (rt). This is a consequence of several factors such as fcc structure and metallic bonding. Strong aluminium alloys date from accidental discovery of the phenomenon of "age hardening" by Alfred Wilm in Berlin at the turn of the 19th century

Wrought Al	Group	Cast Al	Group
Aluminium ≥ 99.00%	*1xxx*	Aluminium ≥ 99.00%	*1xx.x*
Copper	*2xxx*	Cooper	*2xx.x*
Manganese	*3xxx*	Silicon with added Cu and/or Mg	*3xx.x*
Silicon	*4xxx*	Silicon	*4xx.x*
Magnesium	*5xxx*	Magnesium	*5xx.x*
Magnesium and Silicon	*6xxx*	Zink	*7xx.x*
Zinc	*7xxx*	Tin	*8xx.x*
Other elements	*8xxx*	Other elements	*9xx.x*
Unused series	*9xxx*	Unused series	*6xx.x*

***Tab. 1.3**: Designation system for Al alloys [ASMAluminum94 (p.18), Kaufman00 (p.9)].*

[Polmear96]. His work led to the development of the alloy known as *Duralumin*. Another remarkable increase of the strength was achieved in the new family of amorphous alloys which are produced by novel processing methods such as rapid melt quenching and intense deformation (σ_{02} up to 1.5 GPa) [Polmear96]. In addition to the crystalline and glassy phases, a quasicrystalline phase without periodic lattice has been recognized to be the third phase in metallic materials [Shechtman84]. Remarkable strength was achieved in Al-based alloy with high volume fraction of quasicrystalline phase. For example, the fracture strength ~1.3 GPa at rt has been reported for the melt-spun $Al_{92}Mn_6Ce_2$ and $Al_{94.5}Cr_3Ce_1Co_{1.5}$ alloys [Inoue00].

1.1.5. Crystallography and allotropy of magnesium and aluminium

Both magnesium and aluminium form *close packed structures*. As shown in **Fig. 1.2**, "*Close packing*" can be fulfilled in two ways; according to the packing of subsequent layers in the holes (or saddle points) of previous one, one can distinguish a formation of ABABAB structure which is referred to as *close packed hexagonal* (hcp) and ABCABC structure called *face centred cubic* (fcc). While magnesium and most of its alloys form *close packed hexagonal* structure, aluminium has *face centred cubic* structure.

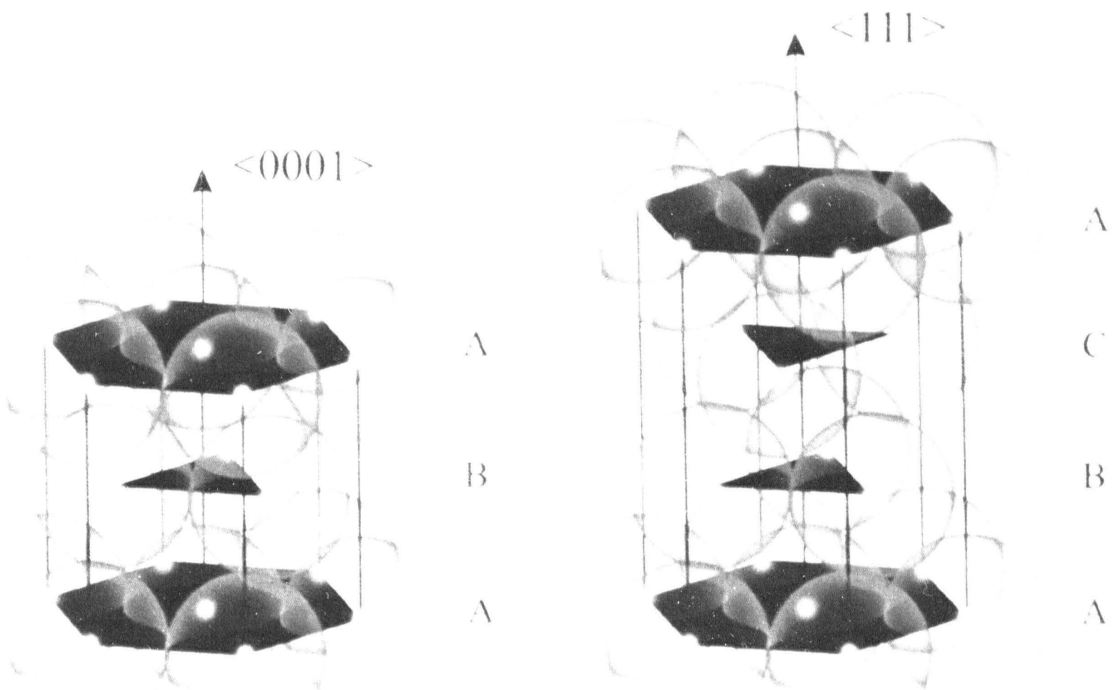

***Fig. 1.2**: hcp structure of magnesium (left); fcc structure of aluminium (right), as viewed from close packing; the atomic centres are highlighted.*

The elements with negligible or limited solubility may tend to form, if present at sufficient amount, intermetallic phases. As an example being mentioned Mg_2Si (Si is practically insoluble in Mg at rt) and $Al_{12}Mg_{17}$ (solubility limit of Al in Mg is about 2.5 at.% at rt) that are commonly observed in AS and AZ series of Mg alloys, respectively. In this regard, it is interesting to note that Mg_2Si undergoes to the polymorphic transformation from the fcc to the hexagonal lattice, a=7.20 Å, c=8.12 Å, at ~2.5 GPa and temperatures above 900 °C. The high-pressure phase is indefinitely metastable at ambient conditions [Shunk69 (p.495), Cannon64].

Hydrostatic compression of pure Mg at rt in a diamond-anvil cell to ~50 GPa shows a transition to bcc structure [Young91 (p.80)]. Calculations at 0 K based on linear muffin-tin orbitals (LMTO) and generalized pseudopotential theory (GPT) predict the sequence hcp → bcc → fcc. LMTO gives the two transitions at 57 GPa and 180 GPa, while GPT predicts them at 50 GPa and 790 GPa. Ab initio pseudopotential calculations (AIP) predict the hcp-bcc transition at 60 GPa. It is readily seen that all used theories are in reasonable agreement with experiment. On the contrary, no change of the structure was found in Al compressed at rt up to 150 GPa. Nevertheless, theory shows that the fcc→hcp transition is to be expected at pressures 120 GPa (LMTO), 240 GPa (AIP) or 360 GPa (GPT) [Young91 (p.89)].

1.2. Scientific issues of magnesium and aluminium alloys

1.2.1. Non-basal slip and ductility of magnesium

Ductility is the ability of a material to deform plastically without fracturing. It is usually expressed by some measure of the strain at fracture. It is recognized that the ductility of a given metal is not a unique property, but rather that it varies with method of loading, specimen shape, temperature, strain rate and environment. The strength, and also the ductility, of a metal during deformation are governed by the balance between work hardening and dynamic softening processes. If work hardening predominates, strength is high but ductility is usually low; if softening predominates, strength is low but ductility is usually high [Tegart68].

A major problem accompanying magnesium alloys is limited low-temperature formability of polycrystals (usually less than 10% at rt) [Avedesian99]. There is a general agreement that low crystallographic symmetry of the magnesium is responsible for detrimental ductility. The dominant slip mode in all hcp metals has the shortest Burgers vector $\vec{b} = (1/3)a\ 11\bar{2}0$, whether the primary slip plane is basal (e.g. Mg, Cd, Zn) or prismatic (e.g. Ti, Zr). Thus, perfect dislocations with Burgers vector $\vec{b} = (1/3)a\ 11\bar{2}0$ and slip plane (0001) are energetically the most favoured in Mg alloys, **Fig. 1.3**.

Under some circumstances (e.g. elevated temperature, improper orientation of basal planes to external loading, ...) another slip planes with $(1/3)a\ 11\bar{2}0$ slip vector can be considered: pyramidal $\{10\bar{1}1\}$ and prismatic $\{10\bar{1}0\}$ (**Tab. 1.4**, **Fig. 1.3**). Any of these dislocations can move, in principle, in this direction. However, since the $11\bar{2}0$ direction is parallel with basal plane, strain accommodation along c-axis is still missing. Even if all slip planes with the $11\bar{2}0$ direction operate, there is still no way to accommodate strains along the c-axis.

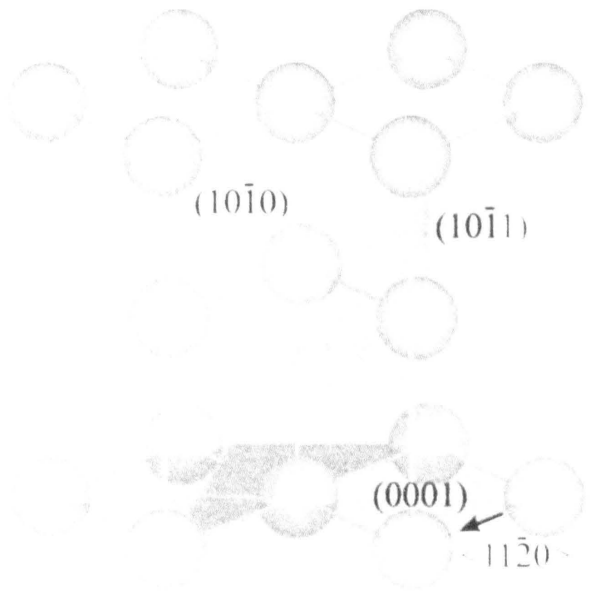

***Fig. 1.3**: Slip elements of the hcp metals: possible slip planes with glide along <a> vector (i.e. in $\langle 11\bar{2}0 \rangle$ direction).*

In order to accommodate a slip in the c-direction, the activity of second-order pyramidal glide is desirable. With glide elements $\langle 11\bar{2}3 \rangle$ and $\{11\bar{2}2\}$ von Misses criterion can be easily fulfilled. The remarkable feature is the large size of the slip vector $1/3\langle 11\bar{2}3 \rangle$ that is the sum of the **c** vector and an **a** vector. Each slip plane contains one slip vector and each slip vector lies in one slip plane. Glide elements, that is slip plane and slip vector, are depicted in **Fig. 1.4**.

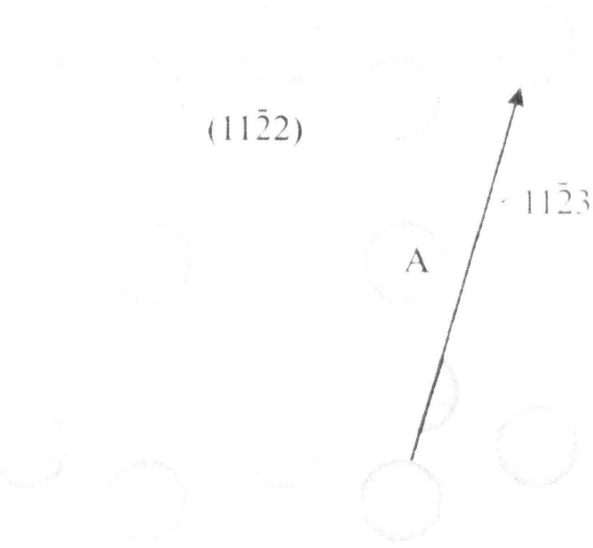

***Fig. 1.4**: Glide elements of the second-order pyramidal plane. Note that glide plane $(11\bar{2}2)$ intersect atom A.*

Experimental evidence of the $1/3\langle 11\bar{2}3 \rangle$ $\{11\bar{2}2\}$ slip in Mg was given by e.g. Obara et al. [Obara73] and Stohr & Poirier [Stohr72]. Slip systems as observed in fcc and hcp metals are listed in **Tab. 1.4**.

Lattice	Slip plane	Slip direction	Number of systems				Examples
			Planes	Directions	Total	Independent *	
fcc	{111}	$\langle 1\bar{1}0 \rangle$	4	3	4x3=12	5	Cu, Ag, Al
hcp	{0001}	$\langle 11\bar{2}0 \rangle$	1	3	1x3=3	2	Zn, Mg, Cd
	$\{10\bar{1}0\}$	$\langle 11\bar{2}0 \rangle$	3	1	3x1=3	2	Ti, Zr
	$\{10\bar{1}1\}$	$\langle 11\bar{2}0 \rangle$	6	1	6x1=6	4	Ti, Mg, Zr
**	$\{11\bar{2}2\}$	$\langle 11\bar{2}3 \rangle$	6	1	6x1=6	5	Zn, Cd, Mg

***Tab. 1.4**: Slip systems for the close-packed lattice structures [Wigley71 (p.10)]. *) [Kelly00 (p.196)]; **) [Kelly00 (p.189, 271)].*

Table 1.5 presents the magnitudes of relative energies for perfect dislocations in hcp structures as derived from the elastic theory.

Type of dislocation	Burgers vector		Relative energy
	Direction	Size	
a	$1/3\langle 11\bar{2}0 \rangle$	a	a^2
c	$\langle 0001 \rangle$	c	$c^2 = (8/3)a^2$
c+a	$1/3\langle 11\bar{2}3 \rangle$	$a^2 + c^2$	$a^2+c^2 = (11/3)a^2$

***Tab. 1.5**: Relative energies of perfect dislocations in hcp metals, e.g. [Kettunen03 (p.73)].*

Slip planes at low temperatures are usually parallel with close packed atomic planes, but this rule has many exceptions. On the other hand, at moderate temperatures, whilst the slip direction remains fixed the slip plane in a given slip line may vary, see **Fig. 1.3** [Kelly00 (p.187)]. However, as T increases gradual activity of slip elements with <**c**+**a**> components should arise because the critical resolved shear stress for second order pyramidal slip system decreases rapidly with increasing temperature.

As mentioned above, ductility of Mg and most of its alloys is strongly limited due to two independent slip systems (basal) available at ambient temperatures. Von Mises derived that the homogenous deformation of polycrystal requires at least 5 independent slip systems [Mises28]. Considering the influence of alloying elements and structure, ductility in Mg alloys can be markedly improved even at ambient

temperatures. Aspects contributing to the ductility enhancement may be summarized as follows:

i) Strong texture with hard orientation for basal slip (i.e. applications of thermomechanical treatments).

ii) Using of suitable alloying elements (Mn, Li, Ce...).

iii) Grain refinement (if i) and ii) are fulfilled, then good ductility can be achieved even with medium grain size).

1.2.2. Twinning

Low crystallographic symmetry accompanied by low number of equivalent slip systems in hexagonal close packed metals (hcp) underline the need to introduce another mode of deformation, by means of which plastic deformation may occur. A benefit of the twinning follows from two reasons: i) to reorient the lattice from one to another orientation and, thus, facilitate a slip, and ii) substitute a lack of slip systems due to possibility to accommodate a strain. Despite minor ability of many twinning modes to accommodate substantial strain during plastic deformation, it plays crucial role in all hcp metals.

Twinning is defined as a homogeneous shear, which restores the lattice in a new orientation; i.e. twinning reproduces the initial structure of a crystal but changes its orientation. Twin formation does not only occur during deformation, but may also occur during solid state phase transformation, during solidification and during annealing [Humphreys04 (p.262)]. It is interesting to note that martensitic transformation is also a shear process very similar to twinning but transforms the crystal into a crystallographically different structure.

Twinning elements are described by K_1 and η_1 where K_1 define twinning plane and η_1 shear (twinning) direction, **Fig. 1.5**. Alternatively the homogeneous shear can occur on a second (so called conjugate or reciprocal) plane K_2 in the direction η_2 [Hall54 (p.43), Crocker62, Klassen64 (p.7), Serra91, Crocker94]. The traces of K_1 plane with the sphere (or with ellipsoid) and $\overline{K}_2$ plane with the sphere (or with ellipsoid) specify the only sections which remain after transformation circular (i.e. the traces of intersection of sphere with ellipsoid). More detailed description of the twinning usually

requires a specification of shear plane S_p ($S_p \perp K_1 \wedge \eta_1 \in S_p$) and crystallographic shear s (i.e. magnitude of the shear strain) [Klassen64 (p.7)]. It can be derived from **Fig. 1.5** that the magnitude of the shear strain s in the unit sphere is given by the angle 2Φ between the two undistorted planes K_1 and K_2, e.g. [Hertzberg83 (p.109)]

$$s = 2\,\mathrm{cotg}(2\Phi). \tag{1.1}$$

However, a mode of twinning is completely defined if K_1, K_2, η_1, η_2 are all known [Hill73 (p.622)]. Only some of the twinning elements need to be experimentally determined, e.g. K_1, η_1 and s, or K_1 and η_2. The remaining elements then follow from the geometry of a simple shear [Kelly00 (p.329)].

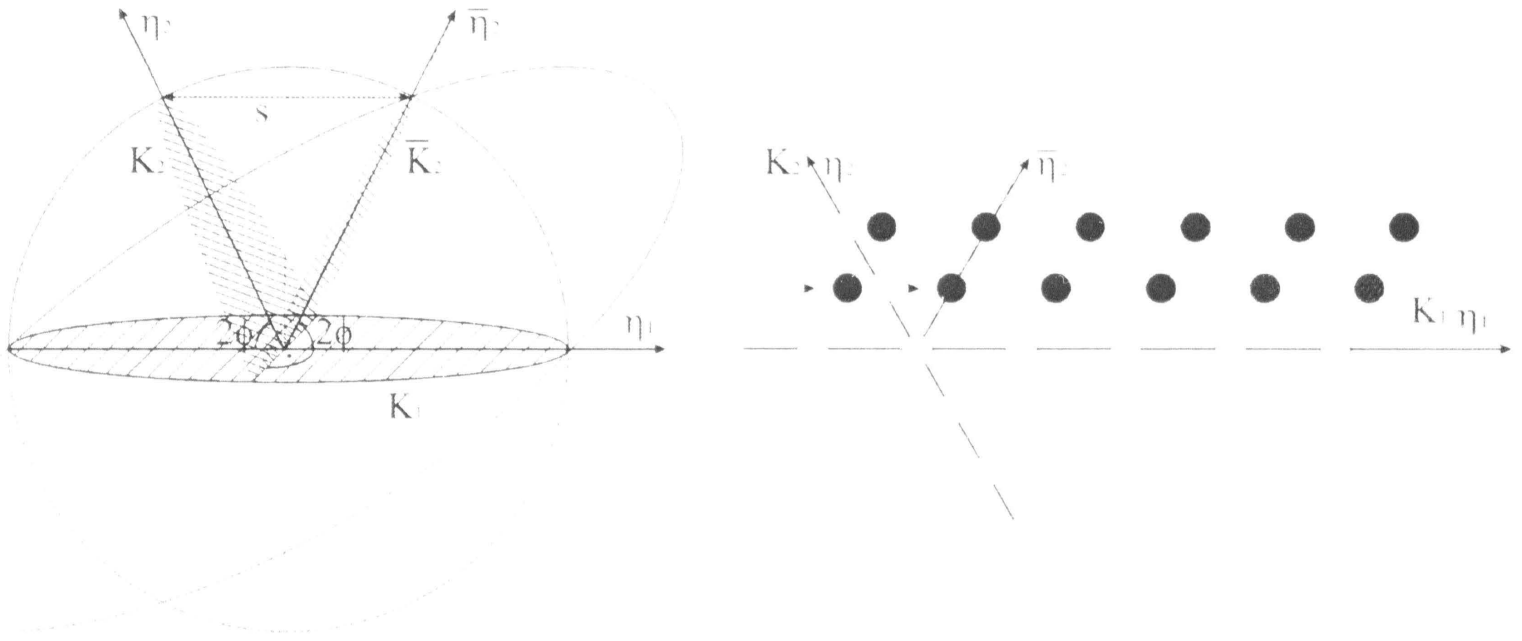

Fig. 1.5: Twinning elements, adopted from [Hall54].

Considering the most prominent mode of twinning in all hcp structures [Serra96, Kelly00 (p.326], i.e. $\{10\bar{1}2\}$, s can be expressed in the simplified form, e.g. [Hertzberg83 (p.113)]

$$s = \frac{1}{\sqrt{3}}\left(\left(\frac{c}{a}\right)^2 - 3\right)\frac{a}{c} \tag{1.2}$$

where axial ratio c/a =1.623 for Mg. Hall showed that the total strain accommodated by completely twinned crystal may be expressed as [Hall54 (p.45), Hertzberg83 (p.110)]

$$\frac{l}{l_0} = \left(1 + s\frac{s \pm \sqrt{s^2+4}}{2}\right)^{\frac{1}{2}} \tag{1.3}$$

where s is crystallographic shear; l_0 and l is initial and final length of the crystal, respectively. The large values of s are not preferred because the strain energy associated

with twins is proportional to s^2 [Hertzberg83 (p.115)]. It means that twins with large s are able to accommodate large strain but, due to an expected energetic requirement, material will be able in most cases to attain the strain accommodation by different way or macroscopic failure occurs rather than twinning.

The composition plane of a twin has been defined as the plane which separates the sheared from unsheared region. It is, therefore, the visible boundary between a twin and the matrix. In very narrow twins, the composition plane and the twinning plane K_1 usually have almost identical orientations because the energy of the twin boundary is a minimum when the composition plane coincides with the plane of twinning. Thus, determination of K_1 can be based on measurements of the orientation of the composition planes of thin twins [Hill73 (p.622)].

The above analysis indicates that a complete description of the twinning requires the knowledge of many parameters. In the scope of this work, however, it is sufficient to define twinning plane K_1 and the angle between basal planes in the twin and a matrix.

As indicated above, Mg and its alloys usually twin along $K_1=\{10\bar{1}2\}$ with disorientation angle between basal planes of 86.3°, e.g. [Avedesian99 (p.8), Nave04, Hauser55, Morozumi76, Barnett04, Christian95 (p.29)]. For completeness, full description of the $\{10\bar{1}2\}$ mode would be following: $K_1=\{10\bar{1}2\}$, $K_2=\{\bar{1}012\}$, $\eta_1=\langle 10\bar{1}\,\bar{1}\rangle$, $\eta_2=\langle\bar{1}01\,\bar{1}\rangle$, $S=\{1\bar{2}10\}$ and s=0.131 [Christian95 (p.24)], **Fig. 1.6**.

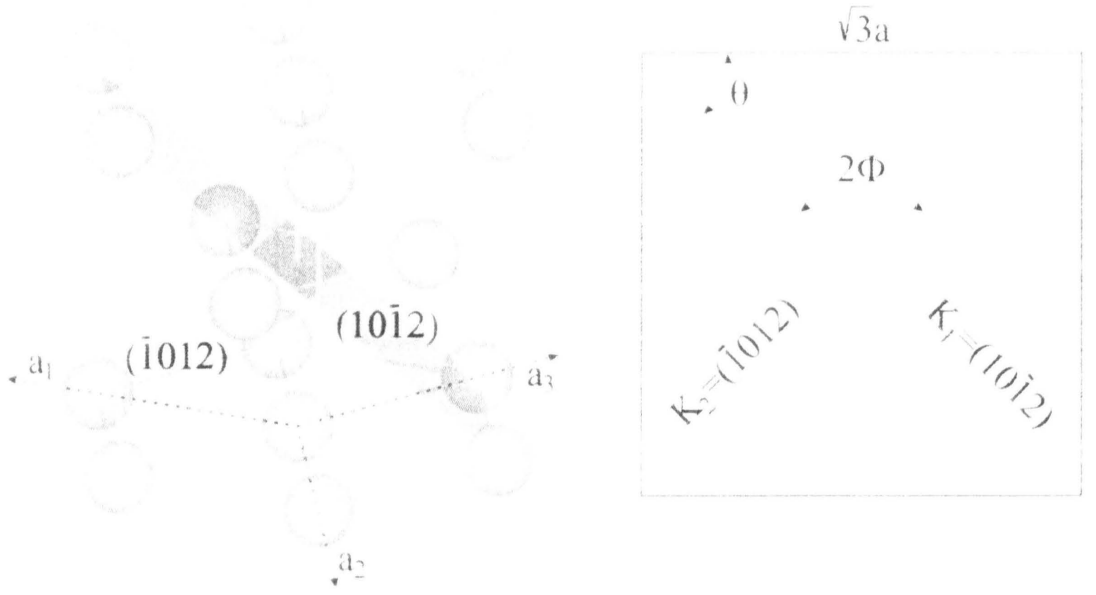

***Fig. 1.6**: $\{10\bar{1}2\}$ twinning elements in hcp structure and their relation to the general description in **Fig. 1.5** [Hertzberg83 (p.113)].*

Another twining modes commonly, but not so often like $\{10\bar{1}2\}$, observed in Mg are $\{10\bar{1}1\}$ (56°) and $\{10\bar{1}3\}$ (64°) [Hill60, Nave04, Hill57]. These twining planes

require higher concentration of elastic strains i.e. high value of s because elastic strain energy is proportional to s^2. Some authors observed at higher temperatures $\{30\bar{3}4\}$ twining system, [Hill57, Avedesian99 (p.8)]. However, as pointed out by Christian & Mahajan [Christian95 (p.26)] and Crocker [Crocker62] on the base of experiments of other authors, the twins $\{30\bar{3}4\}$ are rather secondary twins $\{10\bar{1}1\}$-$\{10\bar{1}2\}$. Secondary twins were reported in $\{10\bar{1}1\}$-$\{10\bar{1}2\}$ (38°) [Ion82, Nave04, Barnett04, Crocker62, Wonsiewicz67] and $\{10\bar{1}3\}$-$\{10\bar{1}2\}$ (22°) [Hill60].

Christian & Mahajan [Christian95 (p.133)] emphasized that twinning in hcp metals is often ductilizing rather than an embrittling agent, inasmuch as twin formation helps to compensate for the small number of operative slip systems, and in particular the difficulty of achieving pyramidal slip.

Spacing in magnesium for both equivalent and nearest planes is illustrated in **Fig. 1.7** and **Tab. 1.6**. The (0001) plane is largely preferred for slip; in $\{10\bar{1}2\}$ most easily twinning occurs; in $\{10\bar{1}1\}$ twinning as well as slip is observed and, furthermore, this twinning plane can serve as a source for secondary twinning; slip may also be observed in $\{10\,1\,0\}$.

Recently, deformation twinning has been found even in fcc nanocrystalline aluminium after microintendation [Chen03]. On the other hand, the occurrence of twins in Al ingots solidified by continuous or semicontinuous casting has already been reported a long time ago [Aust52].

Although twins have been extensively studied, the atomistic mechanism of their formation remains unclear [Humphreys04 (p.263)]. It is considered that twin nuclei may form under the action of applied stress in a near-perfect region of a crystal (*homogeneous nucleation*) or, alternatively, may form only when a suitable defect configuration is present (*heterogeneous nucleation*). To date, however, theoretical calculations and experimental evidence do not support the concept of homogeneous nucleation of twins [Christian95 (p.45)]. Probably, the energy necessary for the creation of homogeneous twin is higher than that for the activity of non-basal slip systems in Mg. Theories based on defect-assisted nucleation usually involve the dissociation of some dislocation configuration into stacking fault which then serves as the twin nuclei, see review [Mahajan02].

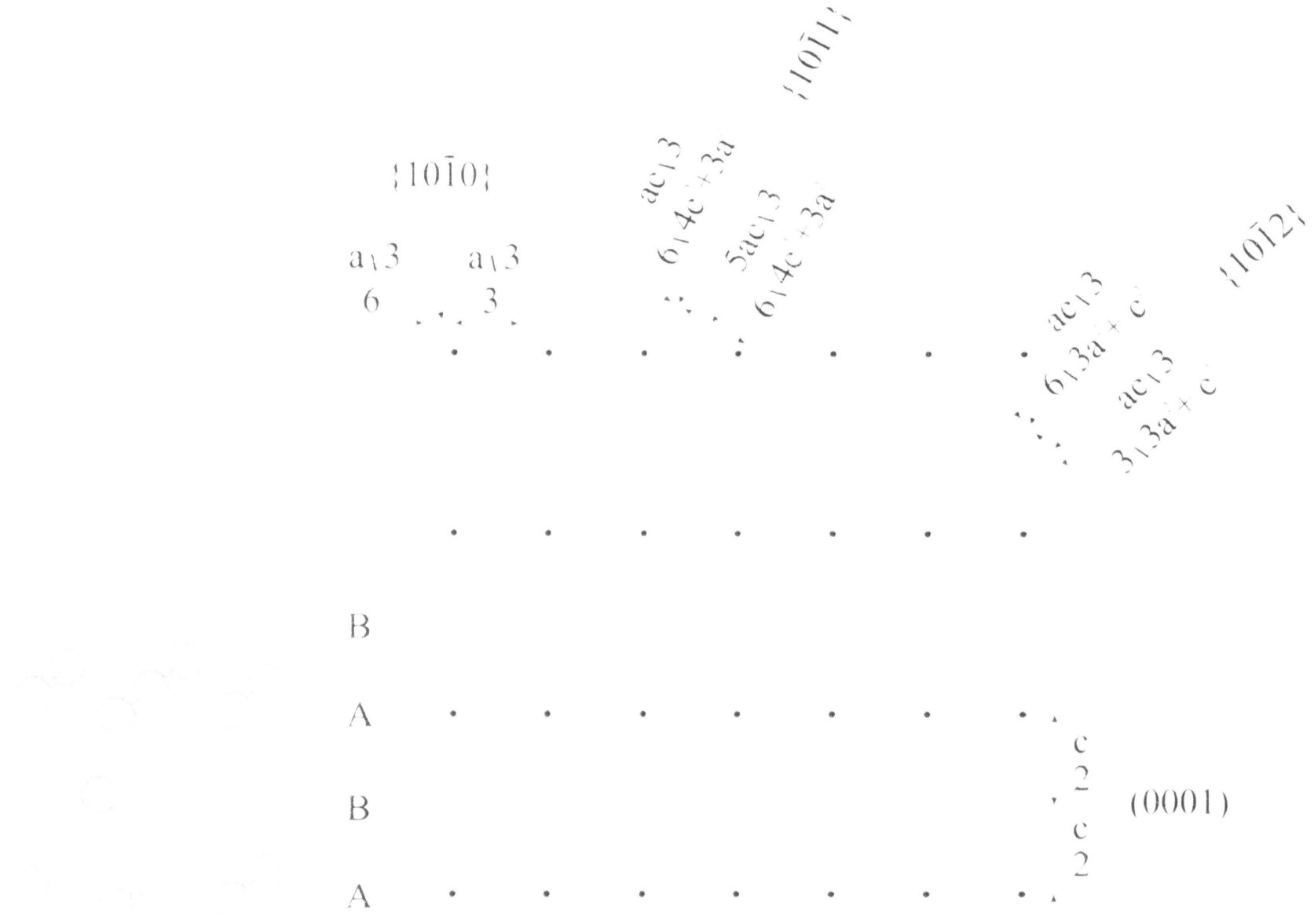

***Fig. 1.7**: Section in the hcp structure (right) revealing interplanar spacing and atom positions [Hertzberg83 (p.76)] as viewed in the normal direction to the inserted plane in the left figure (i.e. inserted plane in the left figure indicates plane of drawing in the right figure).*

Plane	$\{10\bar{1}0\}$	$\{10\bar{1}1\}$	$\{10\bar{1}2\}$	(0001)
Nearest plane [nm]	0.09264	0.04087	0.06336	0.26053
Equivalent plane [nm]	0.18528	0.20435	0.12672	0.26053

***Tab. 1.6**: Spacing between planes in magnesium (a = 0.32092 nm, c = 0.52105 nm) calculated according to **Fig. 1.7**.*

1.2.3. Forming capacities

Many industrial metal-forming methods, such as rolling and extrusion impart large plastic strain and very fine grained microstructures may in certain cases be formed [Humphreys04 (p.499)]. The limit of grain refinement by means of conventional thermomechanical processes is about 10 µm for Al alloys [Humphreys99]. In order to obtain even finer grain structure, *severe plastic deformation* is usually employed. Sub-micron grained alloys may have extremely good mechanical properties. In the past few

years, there has been a considerable interest in using such methods to produce alloys with ultrafine grains, **Tab. 1.7**.

Severe Plastic Deformation	Redundant*	Note
Reciprocal Extrusion	Yes	Rarely used
Torsion under Hydrostatic Pressure	Yes	Pressures about 5 GPa
Equal Channel Angular Extrusion (ECAE)	Yes	Usually in angle 90°
Direct Extrusion	No	
Accumulative Role Bonding (ARB)	Yes	Easily scalable
Multiple Forging	Yes	High T is needed
Friction Stir Welding	Yes	Usually used for joining

***Tab. 1.7**: Methods of deforming metals to very large strains [Humphreys99, Humphreys04 (p.499)]. * "Redundant" means large strain processing method in which a sample can be deformed without any net change in its dimensions.*

While forming of metals leads to the breaking of the structure into smaller peaces which are characterised by low angle and/or special boundaries, preferential orientation of the crystallites (texture) often develops as a by-product. Deformation textures are still a subject of some controversy. If the forming is realized at lower temperatures than necessary for full recovery, a considerable amount of additional energy is stored in material in the form of defects.

1.2.4. Recovery and recrystallization

The accumulation of dislocations and other defects during plastic deformation results in storage of the energy in a material. Due to high mobility of vacancies and interstitials at higher temperatures, point defects do not contribute significantly to the stored energy except the deformation at low temperatures [Humphreys95 (p.12)]. In the common case of deformation at ambient temperatures almost all of the stored energy is derived from the accumulation of dislocations and the essential difference between the deformed and the annealed states lies in the dislocation density and arrangement. It may be shown that the rate of energy storage divided by the rate of work done should be of order 1% in single phase materials with cubic symmetry [Kocks87 (p.10), Humphreys95 (p.12)]. However, it may be quite high (especially at low strains) in two-

phase materials and polycrystals of a lower symmetry such as hcp structure [Kocks87 (p.10)]. Experimental determination of this energy typically gives value about 3% of the work done. These several percent are responsible for all changes occurred in the material. The excess of the energy is released in three main processes: *recovery*, *recrystallization* and *grain coarsening* [Doherty97 (p.220)]. Quantitative measurements of the stored energy are typically realized by calorimetry or X-ray line broadening. It is interesting to note that some qualitative result may also be extracted from SEM-EBSD image quality map.

1.2.4.1. Recovery

Recovery is a tendency of the material to restore energetically more favourable microstructure and to approach the equilibrium state. It may be defined as a process in which the stored energy is released without migration of high angle grain boundaries [Doherty97 (p.220)]. Recovery generally involves only a partial restoration of properties [Humphreys04 (p.3)]. It is primarily described as the changes in the dislocation structure [Humphreys04 (p.169)]. In principle, we can distinguish two modes of the recovery processes which may operate simultaneously: i) annihilation and ii) redistribution of dislocations (e.g. polygonization).

Annihilation may occur either by a) an interaction of mobile (at least one) dislocations by pair reactions or b) an absorption of dislocations by the grain boundaries [Montheillet02]. To explain the annihilation by pair reactions, it is assumed that dislocations which, at the early stages of the deformation, were bound to their original slip planes come into a position to leave these slip planes with increasing dislocation density. The atomic mechanisms considered to be responsible for the process are climb and cross slip. The former mechanism is assumed to occur mainly at high temperatures; the latter is though to place at lower temperatures [Lucke73]. Consequently, the dislocations may annihilate by interaction with dislocations of opposite sign.

If unequal numbers of dislocations of two signs are produced during deformation then the excess cannot be removed by annihilation. Consequently a softening may also occur by redistribution of the dislocations into the configurations possessing lower energy. Typical example of such behaviour is the rearrangement of dislocations to walls, so called polygonization. The process of polygonization results in formation of the low angle boundaries (LABs).

Time for the recovery may range, depending on temperature, from few seconds to many days. Microstructural changes due to the recovery cannot be usually revealed by light microscopy. The recovery is often measured by the changes in a single parameter X_R, such as hardness, yield stress, resistivity or heat evolution. If the change of such a parameter from annealed condition is X_R, then the kinetics of the recovery (i.e. dX_R/dt) may be determined experimentally. However, such analysis gives only partial insight into recovery because the relationship between X_R and microstructure is usually very complex and because recovery may involve several concurrent or consecutive atomistic mechanisms each with its own kinetics [Humphreys95 (p.132)].

Basically, there are two most commonly reported empirical relationships quantitatively describing isothermal recovery [Humphreys95 (p.133)]. First of them may be expressed as

$$\frac{dX_R}{dt} = -\frac{c_1}{t} \qquad 1.4$$

which integrates to

$$X_R = c_2 - c_1 \ln t$$

where c_1 and c_2 are constants. It is clear that this relationship cannot be valid during early stages of recovery ($t \to 0$) when $X_R \to X_0$ or at the end of recovery ($t \to \infty$) when $X_R \to 0$.

Second type of the recovery kinetics is

$$\frac{dX_R}{dt} = -c_1 X_R^h \qquad 1.5$$

which integrates for $h > 1$ to

$$X_R^{-(h-1)} - X_0^{-(h-1)} = (h-1)c_1 t$$

and for $h = 1$

$$\ln X_R - \ln X_0 = -c_1 t$$

where X_0 is the value of X_R at $t = 0$.

Both equations 1.4 and 1.5 were successfully used to describe recovery kinetics in single-crystals as well as in polycrystals. For instance, equation 1.4 fitted well

recovery measured via the changes of the yield stress in zinc single crystal within the simple shear, and equation 1.5 described successfully the dipole annihilation in LiF crystals [Humphreys95 (p.134-136)].

Sharp et al. [Sharp65] studied recovery in 99.99% magnesium. They found that in slightly deformed (up to 5% at rt) magnesium recovery occurs on subsequent annealing at and above 80 °C.

The softening which occurs during the deformation is called *dynamic recovery*, in contrast to the *static recovery* which occurs (during annealing) after the (cold) deformation is completed. The dynamic recovery occurs when the stress-strain curves of metals change with increasing deformation from a rather steep to a flatter course. This may often be explained by the assumption that with increasing deformation the initially dominating hardening processes are supplemented by softening processes. The same situation is observed for increasing temperature; the higher the temperature the flatter is the course of the stress-strain curve. Nevertheless, the recovery need not be confined to plastically deformed materials, but may occur in any crystal into which the defects have been introduced. This can be realized e.g. by irradiation or by quenching from high temperatures. In these situations the recovery will occur on subsequent annealing [Humphreys04 (p.169)].

1.2.4.2. Recrystallization

As mentioned in the preceding paragraph, the recovery often involves only a partial restoration of the properties because enhanced dislocation density is not completely removed. Generally, a more profound restoration process is *recrystallization*. *Conventional* (i.e. *discontinuous*[*]) *recrystallization* involves the formation of new strain-free grains in certain parts of the specimen and their subsequent growth to consume the deformed or recovered microstructure [Humphreys04 (p.215)]. In this process nucleation of new grains and migration of their high angle boundaries (HABs) driven by stored energy is the basic mechanism. The microstructure of a material at any time is divided into recrystallized and non-recrystallized regions

---

[*] Alternatively, continuous recrystallization (CDRX) may occur. CDRX is characterized by continuous transformation of low angle boundaries (LABs) into high angle boundaries (HABs).

(therefore discontinuous). When it occurs during deformation, it is called *dynamic recrystallization* (DRX) or more precisely discontinuous DRX (DDRX). In contrast, recrystallization during annealing of the cold-worked material is then called *static recrystallization* (SRX). The physical mechanisms responsible for DRX are similar in many respects to those controlling SRX [Doherty97 (p.241)]. Recrystallization of the deformed microstructure is often called *primary recrystallization* to distinguish it from the process of *secondary recrystallization* (i.e. *abnormal grain growth*) which may occur in fully recrystallized material [Humphreys04 (p.215)]. The driving force of the secondary recrystallization is the reduction of interfacial energy of grain boundaries [Hill73 (p.319), Titorov92].

Recrystallization is most directly measured by quantitative metallography, wherein its extent is often characterised by recrystallized fraction Xv. For example, the kinetics of primary recrystallisation is in the simplest case described by the Johnson-Mehl-Avrami-Kolmogorov (JMAK) equation, e.g. [Humphreys04 (p.232)]

$$X_v = 1 - \exp\left(-k_0 . t^{\delta}\right) \qquad 1.6$$

where k_0 and δ are constants, t is the time.

The effect of impurities on the recrystallization kinetics is analysed in [Dimitrov78 (p. 137), Montheillet02]. Generally, all types of recrystallization are delayed by the presence of impurities. **Tab. 1.8** gives the temperatures necessary to achieve complete SRX after large deformation by rolling.

Element	Commercial pure metal [°C]	Zone refined metal [°C]
Al	200	50
Cu	180	80
Fe	480	300
Ni	600	300
Zr	450	170

***Tab. 1.8**: Comparison of the recrystallization temperatures for selected metals of different purity [Dimitrov78 (p. 137)]. Unfortunately, the amount and type of impurities is not specified in this work.*

The effect of the second phase particles in cold rolled aluminium single crystals (thickness reduction from 25 to 95%) was examined by Humphreys [Humphreys77]. Recrystallization originates within a region of high dislocation density and large lattice misorientation at the particles, and proceeds by a rapid polygonization process. Montheillet & Le Cosa [Montheillet02] discussed the influence of the purity on DRX. They summarized that purity can strongly influence the kinetics of DRX; e.g. they put forward clear evidence that aluminium changes kinetics from CDRX to DDRX in high purity aluminium grades. DRX during high temperature deformation of Mg-0.8wt.%Al was studied by Ion et al. [Ion82]. They showed that dynamic recrystallisation is a consequence of the relative difficulty of operating non-basal slip systems below 600 K. The mechanism of DRX involved dynamic polygonisation of rotated lattice (mantle) regions adjacent to grain boundaries. At higher strains the deformation is localized into the shear zones wherein DRX takes place.

1.2.5. Superplasticity

Superplasticity (SP) is the capability of polycrystaline materials to undergo extensive tensile neck-free plastic deformation [Padmanabhan80 (p.1), Nieh97 (p.1), Sherby89 (p.171), Langdon94 (p.9)]. Nowadays, there is no doubt that superplastic deformation occurs by "*grain boundary sliding*" (GBS). It remains unclear, however, how GBS is accommodated in the material subjected to superplastic (SP) deformation. It is expected that GB dislocations [Kaibyshev02] and diffusional processes (e.g. [Padmanabhan80 (p.85)]) may play crucial role. However, atomic level understanding of the grain boundary accommodation mechanism is limited. No direct experimental visualization technique is available that allows nonintrusive investigation of grain boundary structures during deformation. [Swygenhoven02].

Based on experimental work of many authors, some structural characteristics of the SP materials may be outlined:

Equiaxed grains: Retention of an approximately equiaxed grain structure following extreme superplastic elongation has been verified repeatedly many times (see [Padmanabhan80 (p.89)]). When the initial structure consisted of elongated grains, superplastic flow converted the grains to an equiaxed shape.

Fine grains: Due to important role of grain boundaries (GBs), fine grain size (~1 μm) is conducive to superplasticity because larger portion of GBs may operate.

Microstructural stability: In order to maintain fine grain size in SP forming range, the presence of stabilising constituent (e.g. second phase) at GB is required. In case of very unstable materials such as nanocrystalline metals at least slowing down of the grain grow is desirable.

Type of GBs: There is no doubt that high angle grain boundaries are responsible for SP.

The course of the stress-strain ($\sigma(\varepsilon)$) curves during SP mode differs from conventional plastic deformation. It is observed that stress is usually (see e.g. [McFadden99]) insensitive to strain (i.e. $\sigma \neq f(\varepsilon)$) which results in the flat $\sigma(\varepsilon)$ curves (steady state flow stress) with low pulling force needed for plastic flow. In contrast with deformation of ductile metals which failure by necking at elongation of tens percent, SP is characterised by neck-free deformation with high elongation to failure (many hundreds of percent). High value of strain rate sensitivity parameter m ($m \geq 0.3$) is a common aspect of the SP.

Environmental conditions at which SP may develop comprise high homologous temperatures during deformation ($T > 0.4T_m$, T_m is melting point) and low strain rates.

A relation for the plastic flow stress was originally considered in the form $\sigma = f(\varepsilon, \dot{\varepsilon}, T)$. It was found by Dorn in 1949 that such function did not exist if changes in T were allowed [Padmanabhan80 (p.10)]. As mentioned above, stress during superplastic deformation is strain insensitive and, therefore, at isothermal conditions it is sufficient to take into account $\sigma = f(\dot{\varepsilon})$ [Padmanabhan80 (p.9)]. For the deformation of superplastic materials a new term has been developed to indicate ability of the material undergo neck-free deformation; strain rate sensitivity parameter m is defined as [Backofen64]

$$m = \left(\frac{\partial \ln \sigma}{\partial \ln \dot{\varepsilon}} \right)_T \approx \left(\frac{\ln(\sigma_2 / \sigma_1)}{\ln(\dot{\varepsilon}_2 / \dot{\varepsilon}_1)} \right)_T \qquad 1.7a$$

where σ_1 and σ_2 is the stress at strain rate $\dot{\varepsilon}_1$ and $\dot{\varepsilon}_2$, respectively.

The strain rate sensitivity parameter m is usually determined by changing the crosshead speed incrementally during tensile straining or by measuring the steady-state stress in separate tests at different strain rates. If the two methods yield identical values, then the steady-state flow stress must be independent of the previous deformation

history[†] [Woodford69]. This situation does generally occur at high homologous temperatures and low $\dot{\varepsilon}$ associated with SP behaviour.

Strain rate sensitivity m is principally a function of $\dot{\varepsilon}$, T and grain size [Padmanabhan80 (p.54)]. However, collected data justify the validity of equation 1.7a and hence m as expressed above is a useful index of strain rate sensitivity [Backofen68 (p.281)]. A convenience stress-strain rate relationship following from equation 1.7a is accordingly

$$\sigma = k_1 \dot{\varepsilon}^{m} . \qquad 1.7b$$

This may be rewritten in the expanded form as (see section 2.2)

$$\dot{\varepsilon} = k_{15} \frac{DGb}{kT} \left(\frac{b}{d} \right)^{p} \left(\frac{\sigma}{G} \right)^{1/m} \qquad 1.8$$

where D is the diffusivity, G is the shear modulus, b is the Burgers vector, d is the grain size, k is the Boltzmann constant, T is the temperature, k_{15} is dimensionless constant, and p grain size exponent (usually between 2 and 3) [Humphreys04 (p.495), Mukherjee02].

In strain rate sensitive materials deformed at high temperatures, the control over the strain stability is undertaken by a large positive strain rate sensitivity parameter m. In order to insure the dominant effect of m, necessary but not sufficient condition is that deformation has to be conducted at high homologous temperatures (T_m>0.4). Then, thermally activated phenomena (i.e. rate controlling mechanisms) have chance to control plastic flow and, considering structural and other circumstances, SP can be developed.

To date, a number of quantitative (constitutive) models have been proposed for GB sliding. A summary of these theories can be found in the work of Nieh et al. [Nieh97 (p.43)] and Sherby & Wadsworth [Sherby89 (p.195)]. All of these models have

---

[†] However, creep tests indicate that this history independence is not always observed [Woodford69]

certain features that are in agreement with experimental observation in superplastic materials and they differ in various prerequisites about GB sliding accommodation.

Superplasticity has been observed in many magnesium alloys, e.g. [Nieh97 (p.69)]. Up-to-date papers on superplasticity have been published by e.g. [Mabuchi99] for AZ91, [Miyahara06] for AZ61, [Lin05] for AZ31, [Galiyev04, Watanabe02, Lapovok05] for ZK60, [Matsubara03] for Mg-9wt%Al, [Furui05] for Mg-8wt.%Li, and [Horita02] for Mg-0.6wt.%Zr. A number of publications deal with superplasticity in aluminium alloys, see e.g. books by Padmanabhan & Davies [Padmanabhan80] and Nieh et al. [Nieh97] and review paper by Sherby & Wadsworth [Sherby89].

Recent development in advanced structural materials [Nieh97 (p.155), Yan03, Watanabe01] enabled to observe SP in metal matrix composites such as PM ZK60 magnesium alloy containing 17vol.%SiC particles and AA6061 aluminium alloy containing βSi_3N_4 whiskers. Maximum tensile elongations about 450% were generally obtained in this class of materials.

2. Theory of the plastic deformation

Deformation process may be described as an ability of the body to transform external stress into strain (elastic or plastic) and, thereby doing a mechanical work in physical meaning.

2.1. Description of the stress-strain curves

In general, any solid exposed to the influence of an external force may undergo to straining accompanied by the change of the shape. The most conventional way occurs according to the following simplified scenario: i) ideal elastic deformation, ii) nonlinear homogeneous plastic deformation, iii) inhomogeneous plastic deformation, iv) failure. However, lots of alternatives are reported as well: e.g. nonlinear elastic; ideal plastic only; fracture in elastic region; linear elastic deformation + inhomogeneous plastic deformation, ...

For the sake of simplicity, in this section is considered tensile deformation test with a constant crosshead speed. The most natural way to define a strain (i.e. shape changes) is to say that strain is a change of the specimen length to the original length

$$e = \frac{l - l_0}{l_0} = \frac{\Delta l}{l_0} . \qquad 2.1$$

This is so-called *engineering* or *nominal* strain. Instead of defining the increments of strain by $de=dl/l_0$ (eq. 2.1) P. Ludwig and A. Leon [Ludwik09, Nadai50 (p.73)] suggested in 1909 that a strain ε (so called *natural* or *true* strain) is to be defined by the increments $d\varepsilon=dl/l$, i.e.

$$\varepsilon = \int_{l_0}^{l} \frac{dl}{l} = \ln\left(\frac{l}{l_0}\right) = \ln(1+e) . \qquad 2.2$$

It can be shown that in comparison with engineering strain true strain better describes the deformation behaviour in the incompressible solids [Ludwik09, Nadai50 (p.73)]. Similarly, one can define true stress as $\sigma = F/S$ where S is a cross section of the specimen changing with deformation and F is a force acting on the specimen.

It has become common practise to define several parameters that characterise material's response during straining. The *sole* true stress - true strain curve gives following information:

Yield stress σ_y is one of the most important material characteristics. By the terms "yield, yielding, yield stress, yield strength or yield point" one means the initiation of *clearly detectable* macroscopic plastic straining of the structure. It means that the yield stress is related to the onset of irreversible plastic deformation. Not all engineering stress-strain curves introduce a *clear yield point*, i.e. clear elastic plastic transition. In this case it is necessary to find approximate value "artificially". This value is referred to as σ_{02} and gives an engineering boundary between elastic and plastic deformation. Generally adopted method for determination of σ_{02} is a construct a line parallel to the elastic portion of the engineering s-e curve but offset from the origin by 0.2%. Then σ_{02} is defined as the intersection of the s-e curve and the offset line.

Maximum stress σ_{max}: Maximum value of the stress by which the specimen may be loaded.

Elongation to fracture (to failure) $A_0 = (\exp(\varepsilon_f)-1)*100$ [%] where ε_f is a true fracture strain.

*Strain hardening exponent (*also termed *strain sensitivity)* n for which following equation holds: $\sigma = k_2 \varepsilon^n$.

Coefficient of work hardening $\vartheta = d\sigma/d\varepsilon$ refers about ability of the material absorb plastic deformation.

Toughness (i.e. the amount of energy that a material can absorb before rupturing) U_t refers about the ability of material to absorb energy. Toughness is a commonly used concept which is difficult to pin down and define [Dieter76 (p.336)]. U_t can be calculated, for instance, as area under engineering stress-engineering strain curve. According to this definition U_t comprises elastic as well as plastic strain energy. Toughness is a parameter that comprises both strength given by σ_{02}, σ_{max} and ductility characterised by A_0. From this definition it is clear that the higher values of σ_{02}, σ_{max} and A_0 the higher U_t. The area under engineering stress strain

curve is an indication of the amount of the work per unit volume (J/m^3) which can be done on the material without causing it to rapture

$$U_t = \frac{\text{Work}}{\text{Initial volume}} = \frac{1}{V_0}\int F\,dl = \frac{1}{V_0}\int F\,v\,dt = \int_{S_0}^{}\frac{F}{l_0}\,dl = \int_0^{e_f}\sigma_0\,de. \qquad 2.3$$

Considering the definitions of the true stress $\sigma = \sigma_0(1+e)$ and the true strain $\varepsilon = \ln(1+e)$, and since $d\varepsilon = de/(1+e)$ the work per unit volume may also be expressed by [Nadai50 (p.79)]

$$U_t = \int_0^{\varepsilon_f}\sigma d\varepsilon \qquad 2.4$$

where σ is true stress and ε is true strain.

Many theoretical accounts have been presented to describe stress-strain curves in the region of *homogeneous* plastic deformation assuming various constitutive equations. The most convenience, simplest and generally accepted relation for *rate-insensitive* material is power law

$$\sigma = k_2\,\varepsilon^n \qquad 2.5$$

which is generally attributed to Hollomon [Hollomon45]. In eq. 2.5 k_2 represents a strength coefficient and n is a strain hardening exponent. Taking into account rate sensitivity m introduced in chapter 1.2.5 and yield stress σ_{02}, eq. 2.5 may be rewritten in the form

$$(\sigma - \sigma_{02}) = k_3\,\varepsilon^n\,\dot{\varepsilon}^m. \qquad 2.6$$

Apart from linear viscous flow ($\sigma_{02} = 0, n = 0, m = 1$) close to the melting point it has been proved, however, that constitutive relation 2.6 does not provide valid descriptions of the plastic deformation of metal specimens at elevated temperatures [Wray70]. For example, Appleby [Appleby70], on the basis of physical requirements outlined by Wray & Richmond [Wray 68], showed that the constitutive equation must contain at least four variables whereas in equation 2.6 there are only three: σ, ε and $\dot{\varepsilon}$. To date no reasonable equation describing general deformation behaviour in the form $\sigma = f(\varepsilon, \dot{\varepsilon}, T)$ has been found. Therefore, considerable efforts have been dedicated to find appropriate relationship in the region where flow stress is independent of strain $\sigma \neq f(\varepsilon)$ as

frequently observed at high temperatures. This is known as *steady state flow stress* and it plays crucial role in *hot working processes* and *secondary creep*. An effort to correlate data for both hot working and creep is therefore obvious. *Steady state* situation is also observed in metals deformed in tension at high homologous temperatures and such behaviour almost corresponds with creep [Poirier85 (p.76), Cadek88 (p.26)]. Additionally, creep equations are commonly incorporated in the theories for description of other deformation processes such as superplasticity. For these reasons brief overview of the creep laws is given in the next section.

2.2. Hot working processes and creep

At certain conditions micromechanims controlling plastic deformation strongly depends on T and $\dot{\varepsilon}$. At relatively low temperatures or high strain rates, it is known that stress depends principally on the strain $\sigma = f(\varepsilon)$ and dependence on $\dot{\varepsilon}$ is usually negligible $\sigma \neq f(\dot{\varepsilon})$, see **Fig. 2.1**. In this case, the change in stress with strain reflects a change in the structure of the metal known as work hardening ($\vartheta >> 0$), and the absence of a rate effect indicates that *recovery processes* are negligibly slow. On the other hand, at sufficiently high temperatures or slow strain rates, simple viscous behaviour prevails with the stress depending primarily on the strain rate $\sigma = f(\dot{\varepsilon})$ and not on the strain $\sigma \neq f(\varepsilon)$, **Fig. 2.1**. In this case, the structure remains essentially constant, recovery processes being sufficiently rapid to overcome any work hardening tendencies, and the change in strain rate with stress reflects the rate of reaction of the constant structure to the applied stress [Wray68]. Thus, *thermally activated processes* causing *recovery* are often called rate-controlling processes. As indicated in previous section, *creep* and *hot working processes* are typical representatives where *dynamic recovery* (DRV) plays a significant role and both of them are of enormous technological interest [McQueen02]. On the other hand, creep research deals with low strain rates (10^{-10} to 10^{-6} s^{-1}) and curtailment of total strain, and hot working research had the objective of reducing flow stress σ and raising the fracture strain at high strain rates (10^{-2} to 10^{2} s^{-1}).

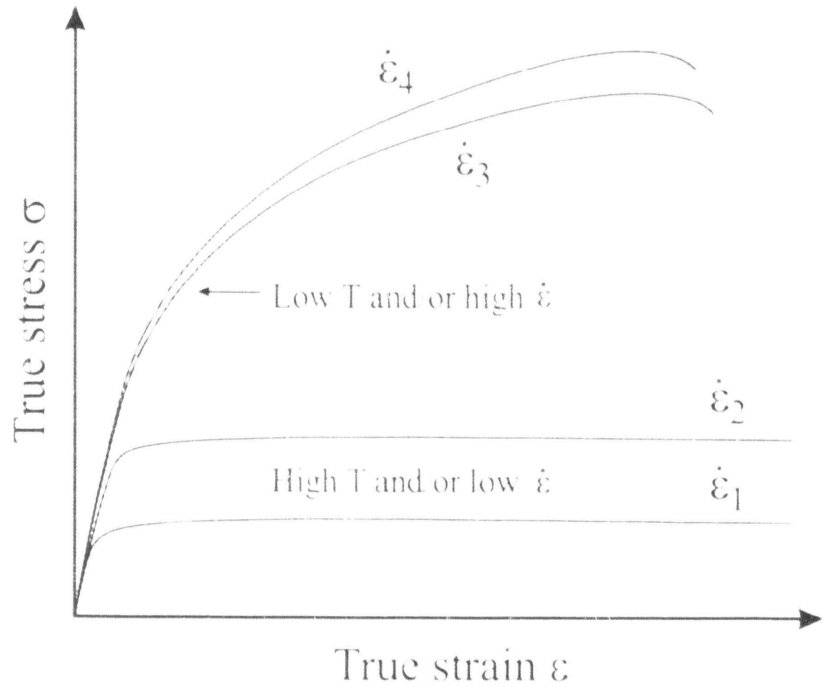

***Fig. 2.1**: Characteristic tensile true stress-true strain curves at different homologous temperatures T and strain rates* $\dot{\varepsilon}$*;* $\dot{\varepsilon}_1 < \dot{\varepsilon}_2 << \dot{\varepsilon}_3 < \dot{\varepsilon}_4$.

It was demonstrated by experiment that creep data at high stresses (i.e. high strain rates as well) correlate with equation, e.g. [Sherby68 (p.341, 360)]

$$\dot{\varepsilon} = k_4 \exp(\beta\sigma) \qquad 2.7$$

and at low stresses

$$\dot{\varepsilon} = k_5 \sigma^n \qquad 2.8$$

where n=1/m in equation 1.7b.

Considering diffusion processes which take place at low strain rates and high temperatures, $\sigma(\dot{\varepsilon})$ was derived in the form

$$\dot{\varepsilon} = C_{NH}\sigma \qquad 2.9a$$

regarding Newtonian viscous flow [Avery65]. It is worth to note that some Mg alloys (e.g. ZK60 alloy) behave in non-Newtonian manner [Karim69, Backofen68 (p.291)]. They need to reach some initial level of the stress (threshold stress) in order to initiate diffusion flow and this has been called Bingham flow. Agreement of equations 1.7b, 2.8 and 2.9a,b for $m = 1/n = 1$ is obvious. Constant C_{NH} can be determined in the Nabarro-Hering analysis of lattice diffusional creep [Herring50]. The same proportionality between σ and $\dot{\varepsilon}$ was derived by Coble for GB diffusion [Coble63]

$$\dot{\varepsilon} = C_C\sigma \qquad 2.9b$$

although constant C_C has different meaning [Karim69]

$$C_{NH} = \frac{k_6 \Omega D}{d^2 kT} \text{ and } C_C = \frac{k_7 \Omega D_g w}{d^3 kT}, \text{ where w is GB width.} \qquad 2.10$$

Numerical constant k_6 depends on the grain geometry. k_7 in Coble creep was derived on the assumption of spherical grains, $k_7 \approx 150/\pi$. k is the Boltzmann constant and Ω atomic volume. D is the coefficient of diffusion through lattice and $D_g w$ is the coefficient of diffusion along GB. They may be generally expressed as

$$D = D_0 \exp\left(-\frac{Q}{R_m T}\right) \text{ and } D_g w = D_{0g} \exp\left(-\frac{Q_{GB}}{R_m T}\right) \qquad 2.11$$

where Q and Q_{GB} is activation energy for lattice and GB diffusion, respectively, and D_0 is independent of temperature. R_m is molar gas constant. Since both lattice and GB diffusion contribute independently to creep it is convenient to represent the overall creep rate by the sum of the two expressions, (eq. 2.9a,b) [Burton77 (p.4)]. Thus

$$\dot{\varepsilon} = (C_{NH} + C_C)\sigma. \qquad 2.12$$

The additional diffusion creep contribution by grain boundary diffusion has important consequences. This is because the activation energy for GB diffusion is less than that for lattice diffusion ($Q_{GB} \approx \frac{2}{3} Q$) and thus the GB contribution predominant at lower temperatures. It was pointed out by Garofalo [Garofalo63] that in creep the dependence $\dot{\varepsilon}_m = C\sigma$ ($\dot{\varepsilon}_m$ is minimum creep rate, C constant of proportionality, $C = C_{NH} \vee C_C$) holds at temperatures near the melting point at low stresses.

Successful attempt for general description of $\sigma(\dot{\varepsilon})$ relation at all stress levels has been made by Garofalo in 1963 by combining of equations 2.7 and 2.8 to the relation [Garofalo63]

$$\dot{\varepsilon} = k_8 (\sinh(\alpha\sigma))^n = k_9 (\exp(\alpha\sigma) + \exp(-\alpha\sigma))^n \qquad 2.13$$

where $\alpha = \beta / n$. This assumption follows from the course of sinus hyperbolic that can be fitted by linear (exponential) dependence of $\dot{\varepsilon}$ at low (high) stresses. Equation 2.13 describes probability of moving (~exp($\beta\sigma$)) and back-moving (~exp(-$\beta\sigma$)) of dislocations under an external stress. While the equation 2.13 is ascribed to Garofalo, the relation $\dot{\varepsilon} \sim \sinh(\sigma)$ was known and used for description of the $\dot{\varepsilon}(\sigma)$ earlier [Conrad61 (p.179)].

Next step in phenomenological description of the hot working processes appears to be that of Sellars and Tegart [Tegart68] who proposed relation between strength σ, temperature T and strain rate $\dot{\varepsilon}$ in the form

$$\dot{\varepsilon} = k_{10}(\sinh(\alpha\sigma))^{n} \exp\left(-\frac{Q}{R_m T}\right) \qquad 2.14$$

where k_{10}, α and n are temperature independent constants and Q is an activation energy defined in the next section 2.2.1. The relation of Sellars and Tegart is a development of the equation 2.13 proposed for creep by Garofalo.

It is worth to mention that Dorn [Mukherjee69] combined as early as 1956 equation 2.20 in section 2.2.1 and equation 2.8 (or 1.7b if $m = 1/n$) and obtained empirical mechanical equation of state for creep in the form

$$\dot{\varepsilon} = k_{11}\sigma^{n} \exp\left(-\frac{Q}{R_m T}\right) \qquad 2.15$$

where k_{11} differs greatly from metal to metal. Note that at low stresses, equation 2.14 reduces to the same relation as equation 2.15 [Tegart68]. According to Mitchell et al. [Mitchell02] this constitutive equation is not valid for materials with a high Peierls stress and then the derived quantities (Q, $n = 1/m$) are only apparent values. In 1961, McLean and Hale made an important observation that variation in k_{11} amongst the various metals and alloys seems to depend systematically on their moduli of elasticity (see [Mukherjee69] for reference). They have shown that the correlation of secondary creep rates among the various metals and alloys is considerably improved when equation 2.15 is rewritten as [Mukherjee69]

$$\dot{\varepsilon} = k_{12}\left(\frac{\sigma}{G}\right)^{n} \exp\left(-\frac{Q}{R_m T}\right) \qquad 2.16$$

where G is the shear modulus of elasticity. Similarly, Sherby suggested empirical relation in the form

$$\frac{\dot{\varepsilon}}{D} = k_{13}\left(\frac{\sigma}{E}\right)^{n} \qquad 2.17$$

where $D = D_0 \exp(-Q/R_m T)$ and E is Young's modulus of elasticity [Mukherjee69]. Some arguments, however, may be raised against equation 2.17 [Mukherjee69]: i) it is

not dimensionally correct and ii) is not wholly consistent with the requirements for thermally activated or diffusion-controlled mechanisms of creep.

Both requirements may be obeyed if we consider relationship (*Dorn equation*) proposed by Mukherjee et al. in 1969 [Mukherjee69] (compare with eq. 2.8)

$$\dot{\varepsilon} = k_{14} \frac{DGb}{kT} \left(\frac{\sigma}{G} \right)^n \qquad 2.18$$

where k_{14} is dimensionless constant. The introduction of a power low creep equation under the form proposed by Mukherjee et al. [Mukherjee69] is justified by the fact that the *activation energy* for many metals (see [Sherby68 (p.338)] for exceptions) deformed in creep is reasonably close to that for self-diffusion. Equation 2.18 can be further modified by the addition of grain size dependence to the form [Cadek88 (p.65)]

$$\dot{\varepsilon} = k_{15} \frac{DGb}{kT} \left(\frac{b}{d} \right)^p \left(\frac{\sigma}{G} \right)^{1/m} \qquad 2.19$$

where k_{15} is dimensionless constant, and p grain size exponent.

2.2.1. Activation energy

Thermally activated processes during plastic deformation are analysed on the base of knowledge of activation energy Q, because any strain-accommodating mechanisms has to overcome an energy barrier to contribute an elementary strain. The energy necessary to overcome the barrier is provided by the applied stress and the thermal agitation [Poirier85 (p.76)].

Based on experimental experience, strain rate at a constant stress is usually exponential function of temperature. This so called "*Arrhenius equation*" presented bellow is the relation of semi-empirical nature which is found to fit many rate controlled processes such as creep and diffusion in metals [Birchon65 (p.20)]. It may therefore be written

$$\dot{\varepsilon} = \dot{\varepsilon}_0 \exp\left(- \frac{Q}{R_m T} \right) \qquad 2.20$$

where Q is the *apparent activation energy* ($Q = Q_0 - V\sigma^*$, Q_0 is the stress-free activation energy, V is the activation volume and σ^* is a thermal component of the

applied stress $\sigma=\sigma_i+\sigma^*$). If the deformation process is controlled by a unique, thermally activated process, the apparent activation energy is equal to the activation energy of the controlling process. However, it is often the case that several potential rate-controlling processes exist and differ in the activation energies.

The activation energy Q for GB diffusion and dislocation core diffusion in magnesium is 92 kJ/mol, and for lattice self-diffusion 135 kJ/mol [Frost82 (p.44)]. The activation energy Q for self-diffusion in aluminium (99,99%) is 138 kJ/mol [Nowick51].

2.2.2. Zenner-Hollomon parameter

The first who proposed the quantitative description connecting $\dot{\varepsilon}$ with T were Zener & Hollomon in 1944 [Zener44] although qualitative equivalence of an increase of temperature to a decrease in rate of deformation upon the effect of the mechanical properties of metals was at that time well known. They found that relation may be expressed in the form

$$Z = \dot{\varepsilon} \exp \frac{Q}{R_m T} \qquad 2.21$$

where Z is the *Zener-Hollomon parameter*. The Zener-Hollomon parameter combines the two control variables: temperature of deformation and strain rate. The relation may be theoretically interpreted but exact determination has not yet been performed. The first experimental verifying of the equation 2.21 was done in subsequent work for steels in tension [Zener44a].

2.3. Work hardening

A term "*work hardening*" means gradual increasing of the stress σ with the strain ε during plastic deformation. Hardening can be caused by several large groups of mechanisms. First of all being mentioned dislocations accumulated during straining, second large group is connected with obstacles present prior deformation such as foreign atoms, precipitates and dispersoids; last but not least grain boundaries may introduce effective barrier for overcoming by dislocations.

2.3.1. Hardening due to dislocations

If dislocation density ρ is plotted vs. resolved shear stress τ in the operating slip system, all points fall within reasonable scatter around an equation [Wiedersich64]

$$\tau \approx \quad \rho \,. \qquad 2.22$$

Thus, for a wide variety of stress strain curves the resolved shear stress τ is proportional to the square root of the dislocation density ρ. This relation is found to be valid in a variety of materials and can be written as

$$\tau = \tau_{0} + \alpha' G b \quad \rho \qquad \text{(or similarly for polycrystals } \sigma = M\,\tau) \qquad 2.23$$

where τ_0 is the Peierls-Nabarro stress, G is the shear modulus, b is the Burgers vector, α' is a numerical constant ($\alpha' \approx 0.3$-0.6) and M is the Taylor factor ($M \approx 3$-6). In the past, several models have been suggested for mechanisms of work hardening by dislocations and all of these models lead essentially to the same relation between the flow stress and the dislocation density; the same as was found experimentally (eq. 2.23). The models are summarised in **Tab. 2.1**. Weidersich published a nice review on this subject [Wiedersich64]. The factor k_i (i=T, S, B, M or K) appearing in a variety of theoretical models does not differ too much from unity. Thus, constants α' for different models are very close to experimental value of α' introduced in eq. 2.23.

Model	Type of mechanisms	Derived equation
Taylor	Dislocation superlattice	$\tau - \tau_0 = \dfrac{1}{2\pi k_T} G b \sqrt{\rho}$
Seeger	Superlattice of pile-ups or glide zones	$\tau - \tau_0 = \dfrac{n}{2\pi k_S} G b \sqrt{\rho}$
Basinski	Elastic interaction between intersecting dislocations	$\tau - \tau_0 = \dfrac{1}{2\pi k_B} G b \sqrt{\rho_f}$
Mott-Hirsch	Dragging of superjogs	$\tau - \tau_0 = \dfrac{1}{2\pi k_M} G b \sqrt{\rho_f}$
Kuhlmann-Wilsdorf	Bowing-out between network points in dislocation tangles	$\tau - \tau_0 = \dfrac{1}{\pi k_K} G b \sqrt{\rho_f}$

***Tab. 2.1**: Comparison of five models for work hardening according to the review by Weidersich [Wiedersich64] (ρ denotes the dislocation density parallel to slip dislocations and ρ_f the density of forest dislocations).*

Recently, correlation between dislocation density and stress in Al and Al-Mg solid solution alloys has been studied by Guyot & Raynaud [Guyot91]. They have shown by using of several experimental techniques that dislocation density versus hardening follows a classical $\rho^{1/2}$ law for most of the strain range.

2.3.2. Hardening due to obstacles (foreign atoms,precipitates,dispersoids)

As mentioned by Mott [Mott56 (p. 31)] an explanation of hardening by means of foreign atoms distributed along dislocation lines was first given in 1948 by Cottrell [Cottrell48] and applied to the case of iron containing carbon. One of the consequences of Cottrell's hypothesis that impurities are lodged in the dislocations, is that impurities should cause a yield point. Another is that very minute traces of impurity may have a profound effect on the hardness. Theoretical treatment of hardening in random solid solutions predicts that *critical resolved shear stress* τ should vary as [Fleischer64]

$$\tau = k_F c_f^{1/2} \qquad 2.24$$

or as [Labusch70]

$$\tau = k_L c_f^{2/3} \qquad 2.25$$

of the solute concentration c_f in atomic fractions. The quantities k_F and k_L are parameters characterising material. Akhtar & Teghtsoonian [Akhtar71] applied both theories to measure concentration dependence in magnesium binary solid solutions. It appears that $\tau \sim c_f^{2/3}$ gives better results. The same conclusion has been verified by Lukáč for cadmium-based alloys [Lukac81].

Strengthening due to precipitates and dispersoids can be described by the analogous relation because dispersoids may be considered as incoherent precipitates. It has been derived that the critical resolved shear stress for particle-strengthened alloys relation has following form

$$\tau = \frac{k_p G b}{L} \qquad 2.26$$

where L is the mean distance between particles, and constant k_p depends on coherency or incoherency of the particles, their volume fraction etc. [Gerold79 (p.219)].

2.3.3. Hardening due to grain boundaries

The overall geometry of the grain boundary is defined by five degrees of freedom: two for GB plane and three for orientation of adjacent crystallites [Humphreys04 (p.91), Randle04]. Depending on the type of dislocation, its orientation to the grain boundary (GB), stress fields in the material and the type and orientation of GB, they may serve as effective barriers. The relation between the yield or flow stress σ and a mean grain size d (i.e. Hall-Petch relation)

$$\sigma = \sigma_0 + k_{HP} . d^{-1/2} \qquad 2.27$$

was first proposed by Hall [Hall51] and later extensively studied by Petch [Petch53] on steels. Although Hall and Petch supposed pile-up of dislocations of like sign generated from a Frank-Read source [Frank50], various prerequisites may lead to the same relation [Li63]. Equation 2.27 holds for broad range of grain sizes but for fine scale nanostructures with grain size bellow ~10-20 nm the Hall-Petch law breaks down [Nieh05].

Grain boundary character is of industrial significance because many properties of polycrystals (Coble creep, SP, intergranular fracture, intergranular (stress) corrosion, recrystallization, segregation) depend on the nature of GBs. In spite of extensive research in the area of GBs over the past few decades, there is still a great deal of uncertainty about their structure and properties [Humphreys04 (p.92)].

Ono et al. [Ono03] published temperature dependence of the Hall-Petch relation for pure magnesium polycrystals with medium grain size. Extensive research is now dedicated to the study of Hall-Petch relation in AZ series of alloys prepared by intensive forming [Wang06, Uematsu06, Barnett04a]. Summary of the results for pure aluminium and some Al-based alloys together with an attempt to correlate H-P relation in ultrafine-grained Al alloys in dynamic strain rate range ($\dot{\varepsilon} \propto 10^3 s^{-1}$) was published by Mukai et al. [Mukai98, Mukai95]. It is worth to note that all these studies confirmed relation 2.27.

3. Objectives of the thesis

The main object of this thesis is to contribute to the description of plastic deformation in selected light metal alloys. Herein microstructural evolution and mechanisms acting during plastic deformation are analysed. Particularly, following points are covered:

1. A study of deformation characteristics in two commercially available alloys:
   a) AZ31 rolled magnesium alloy
   b) AA6082 extruded aluminium alloy
2. Microstructural evolution in AZ31 alloy and its influence on plastic deformation.
3. Analysis of the micromechanisms of plastic deformation at various strain rates and temperatures in both alloys.

Since lots of studies are now available for both the microstructure and the deformation behaviour of aluminium, this work deals mainly with AZ31 magnesium alloy. Favourising of aluminium may stem from better castability without protective atmosphere, easer forming capacities caused by crystallographic structure and better corrosion resistance due to natural formation of protective surface layer. Although magnesium is known for a long time and its alloys are commonly processed in industry, there is incomplete picture about processes taking place during plastic deformation.

4. Experimental methods

4.1. Deformation testing

Mechanical testing was conducted by uniaxial loading (tensile tests) on the Instron type machines (Instron 1186, 5882). Specimens were deformed at constant crosshead speeds giving initial strain rates between ~10^{-4}-10^{-1} s^{-1}. Collected data was in the form of force versus time. Computer-aided data acquisition was further treated by commercially available software (MS Excell, Sigma Plot and TableCurve) in order to obtain true stress-true strain curves described in chap. 2.1. The yield stress σ_{02} was determined as the offset of 0.2% strain. An experimental error in determination of the stress (calibration of the machine, uncertainties in a measurement of the specimen cross section, etc.) is estimated to be ± 5 MPa.

4.2. Heating

Deformation testing at higher temperatures was performed with conventional furnace in air atmosphere. Before testing each specimen was hold approx. 15-30 min. at the desired T in order to insure thermal equilibrium.

Static annealing used for the microstructure evolution was conducted in air atmosphere. Specimens were inserted into warm furnace. After annealing, specimens were removed from furnace and air-cooled (unless otherwise noted).

4.3. Electron backscatter diffraction technique (EBSD)

Scanning electron microscope (SEM) equipped with EBSD detector (HKL Technology) was used in this study to reveal microtexture of AZ31 alloy. Detailed information about the method can be found in [Schwartz00] or in electronic form www.hkltechnology.com, www.ebsd.com, [Zaefferer] and [Edax].

4.4. Light microscope

Olympus X-86 light microscope equipped with digital camera was employed to study the microstructures at magnification of 50x-750x. The etched microstructures

were used to reveal and characterise structural parameters such as grain size and twinning.

4.5. Specimen preparation for microscopy observation

The specimens of AZ31 alloy for observation with the help of both light microscopy and electron back-scattered diffraction technique (SEM-EBSD) were prepared by conventional grinding and polishing technique up to 1μm diamond suspension. The differences were in final polishing and chemical treatment. Specimens for light microscopy were etched in [Avedesian99 (p.27)]: *Acetic-picral: 10 mL acetic acid, 4.2 g picric acid, 10 mL H_2O, 70 mL ethanol.* Specimens for SEM-EBSD need more attention. After grinding up to 1 μm the specimens were subjected to mechanical-chemical polishing by a solution of colloidal alumina (OPA). The main target was to remove distorted layer, at which stresses after mechanical polishing are accommodated and, thus, uncover pure structure which enable to reveal crystallographic orientation.

4.6. X-ray diffraction

Measurements were performed on Philips X'Pert PRO MRD diffractometer equipped with Eulerian cradle and laboratory X-ray lamp with characteristic CuKα radiation. For macrotexture measurement the following setting was used: X-ray lamp with point focus, poly-capillary optics in the incident beam, parallel plate collimator, graphite monochromator and a point detector in the diffracted beam.

Sample was mounted on an Eulerian cradle that enables sample (ϕ) rotation around the axis perpendicular to the sample surface and (ψ) tilting of this axis in the direction perpendicular to the diffraction plane. Preferred orientation of crystallites (i.e. pole figure measurement) can be characterized by recording diffracted intensity for a selected diffraction angle and for different ψ-tilts and ϕ-rotations.

The samples for X-ray diffraction were polished up to one micron but material with unprepared surfaces revealed qualitatively identical pole figures. The texture was measured in all cases near the surface. Collected X-ray intensities were corrected for experimental aberrations (defocusing etc.) and the background was subtracted. Incomplete pole figures (up to $\Psi=60°$) were measured and polar coordinates (Φ,Ψ)

were recalculated into Cartesian ones (x,y) by using of the relations depicted on x,y axes in the pole figures.

4.7. Values versus units

Constitutive analysis often requires the using of the complex functions such as logarithm, hyperbolic sinus, etc. in the respective graphs. It is apparent that these functions can only be applied on the unit-less variables. Therefore, in principle all variables should be compensated to be dimension-less (e.g. stress is usually compensated by elastic modulus, etc). For the sake of simplicity, however, only the values (i.e. unit-less numbers) are taken into consideration for the treatment by mathematical functions.

5. Results and their discussion

5.1. AZ31 magnesium alloy

5.1.1. Composition and properties

Commercial wrought AZ31B alloy sheets with thickness 1.6 mm in the H2 temper [Avedesian99 (p.18)] were used in this study. Nominal composition and the purpose of elements are listed in **Tab. 5.1**. The sheets have been supplied by GKSS-Research Centre, Germany [GKSS02].

Element	*Al*	*Zn*	*Mn*	*Mg*
Composition in wt.%	*3*	*0.9*	*0.15*	*Balance*
Purpose	*Improve casting*	*Strengthening effect better than Al*	*Improve corro-sion resistance*	

***Tab. 5.1**: Nominal composition of AZ31 magnesium alloy.*

AZ31 alloy is the most common magnesium alloy used for wrought products (mainly rolling). In comparison with the oldest magnesium alloy AZ91 (nominal composition Mg-9Al-1Zn-0.2Mn in wt.%), the occurrence of relatively brittle intermetallics compound $Mg_{17}Al_{12}$ is suppressed. This provides better forming capacities but reduce the strength. Compromise between strength (AZ91) and forming capacities (AZ31) was offered by e.g. AZ61 and AZ81.

Direct competitors of the AZ31 alloy can be considered AM50 (nominally Mg-5Al-0.5Mn in wt.%) and ZK60 (nominally Mg-6Zn-0.5Zr in wt.%). AM50 offers better formability and impact properties (higher toughness) but lower strength. ZK60 is the strongest Mg alloy for ambient temperatures due to i) grain refinement by zirconium and ii) strengthening by zinc. On the other hand, higher amount of zinc causes an increase in susceptibility to hot cracking during solidification, e.g. [Polmear92].

5.1.2. Characterisation of the as-received structure

A typical as-received microstructure is shown in **Fig. 5.1**. A lot of twins in the grains are result of rolling. The mean grain size is 45 ± 5 μm ($d = 1.74 \times \bar{d}$, where $\bar{d}$ is the mean linear intercept). Nevertheless, it should be pointed out that the grain size

distribution was often inhomogeneous and in some heavily deformed sites a loss of etching contrast and definition of grain boundaries (GBs) was observed. These sites were composed from networks of twins and shear zones [Ion82]. The twins may partly accommodate plastic strain induced by rolling. At higher initial strain rates (as expected in rolling) and suitable temperatures, twinning in magnesium alloys may be very important deformation mode that is often ductilizing rather than an embrittling agent [Christian95 (p.133)]. Purposely we use the term "suitable temperatures", because twinning activity may stem not only from low crystallographic symmetry (to compensate the lack of slip systems) or dissociation of dislocations but from dislocation reactions as well. In this case the activity of non-basal slip systems may give arise to twinning by means of mutual dislocation reactions [Christian95 (p.76)].

It can be expected that networks of twins induced by rolling may play an important role during annealing owing to the relaxation of accumulated energy (see section 5.1.3).

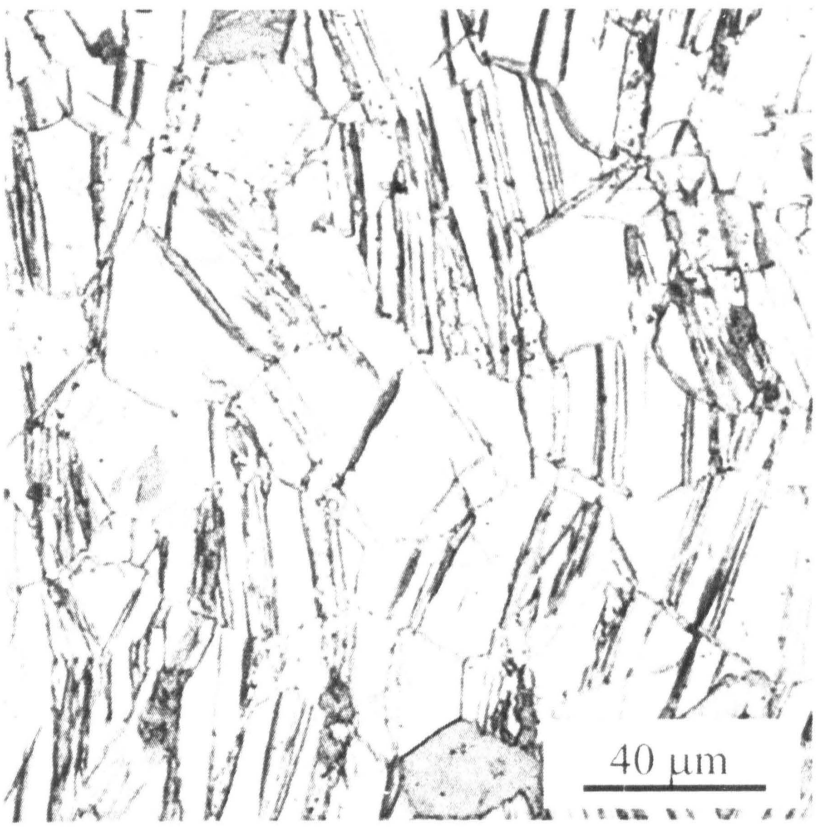

Fig. 5.1: *As-received microstructure of the AZ31 alloy. Rolling direction (RD) is horizontal and transversal direction (TD) is vertical. Light microscopy.*

It is well known that magnesium and its alloys subjected to forming exhibit a distinct texture. The (0002), $\{10\bar{1}0\}$, $\{10\bar{1}1\}$ and $\{10\bar{1}3\}$ pole figures of the as-received AZ31 sheets, obtained by X-ray diffraction technique, are shown in **Fig. 5.2**. Darker contrast corresponds to stronger X-ray intensity. It can be seen from the (0002) pole figure that the most of crystallites in the sample are oriented with plane (0001) nearly parallel to the plane of the sheet. Thus, c-axis of the most grains is almost perpendicular

to the plane of the sheet. Symmetrical maxima in pole figures $\{10\bar{1}1\}$ and $\{10\bar{1}3\}$ show pronounced preferred orientation of crystallites and $\langle 11\bar{2}0\rangle$ direction parallel to the rolling direction (RD). It has been recognised that rolling textures result from the combined effect of the c/a ratio and the activity of different slip and/or twinning systems [Agnew01]. Near ideal c/a ratio of Mg (c/a = 1.624) suggests developing ideal basal texture. However, ideal basal texture is rarely observed in Mg and a slightly off-basal texture is the norm [Agnew01]. The c-axis is a little bit inclined from the vertical direction most likely as a result of interaction between roll and rolled material.

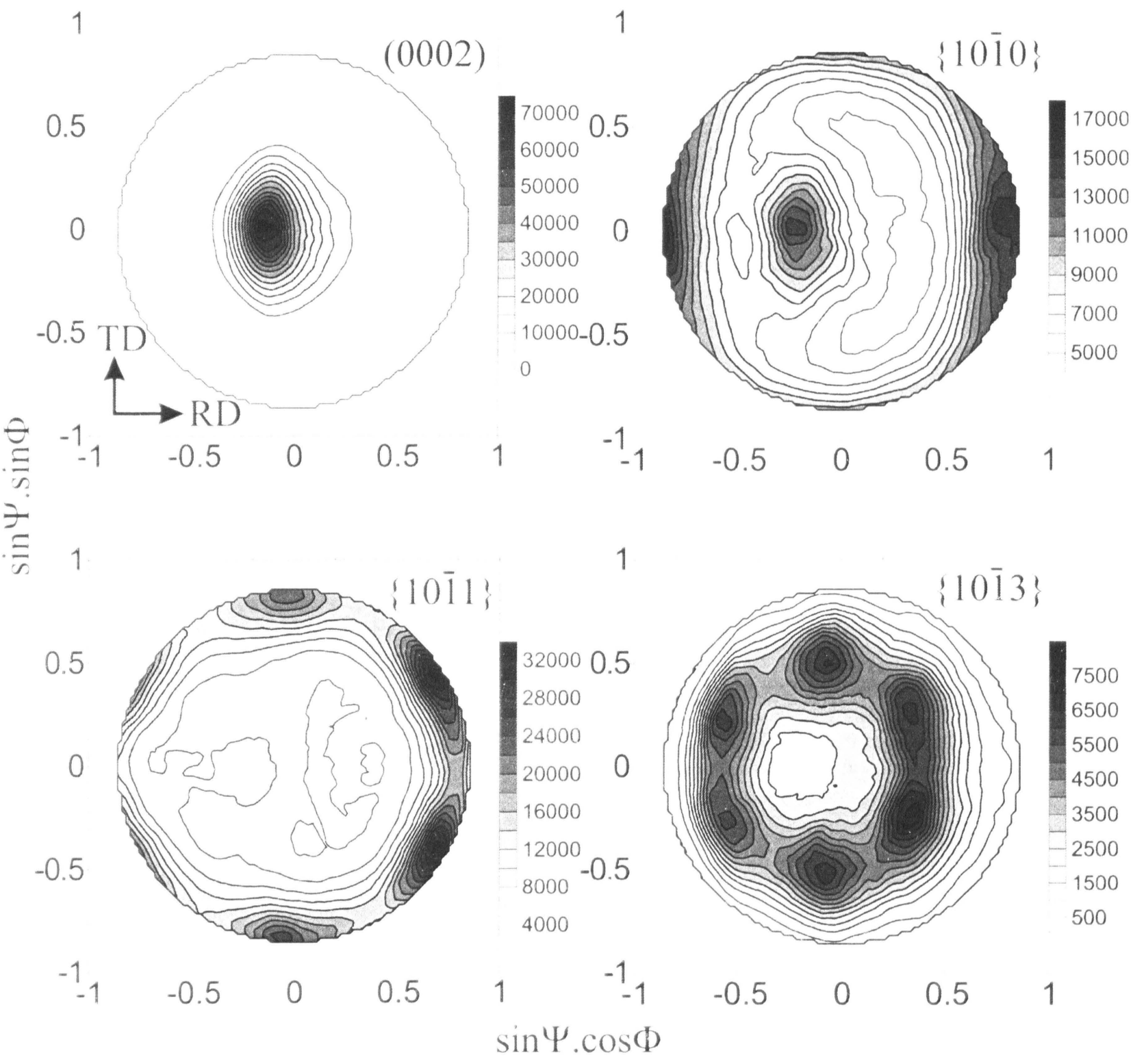

***Fig. 5.2**: Direct pole figures performed by X-ray diffraction on the as-received specimen. RD and TD indicate rolling and transversal direction, respectively [Jager06].*

5.1.3. Microstructure evolution during static annealing

It is obvious that the defects introduced by rolling increase the energy of the

alloy. As mentioned in chapter 1.2.4 this energy may be revealed by several processes. Jager et al. [Jager06] have shown that static recrystallization (SRX) takes place at $T \geq 200$ °C. In this section microstructure evolution during static annealing is analyzed.

Fig. 5.3 shows representative microstructure before and after SRX. Recrystallized microstructure is a result of annealing at 400 °C for 2 h. While the grain size before and after SRX is similar, annealing causes a more homogeneous grain size distribution. Only few twins were observed after SRX.

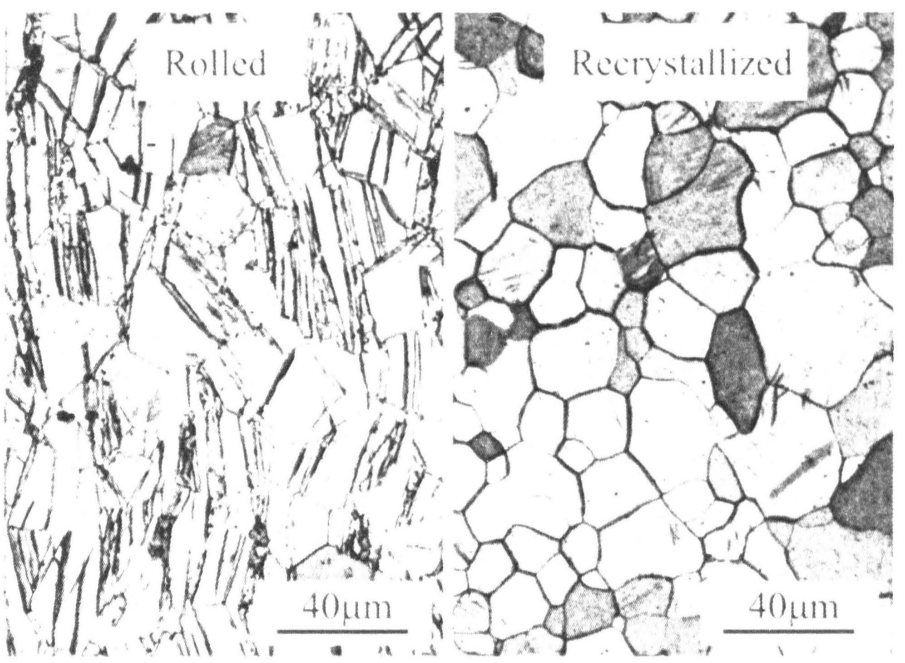

Fig. 5.3: Typical "as-received" (left) and completely recrystallized (right) microstructure. Rolling direction is horizontal and transversal direction is vertical.

Orientation map obtained by SEM-EBSD for specimen annealed at 200 °C for 1 h is shown in **Fig. 5.4**. Partly recrystallized structure with the indication of previous shear zones (in the direction of the marker in the lower right corner) is visible. Adjacent grains with misorientation angle less than 20° are in red. The small portion of low angle boundaries is apparent. Histogram of misorientation angles between nearest grains and direct pole figures is also given in **Fig. 5.4**.

Note a local maximum in the histogram between 80-90°. From "the rate of changes" point of view, the annealing conditions (200 °C for 60 min) represent relatively early stage of the microstructure evolution. Thus, these GBs may originate from very common $\{10\bar{1}2\}$ twins [Avedesian99 (p.8), Christian95 (p.29)] because basal planes in twinned and untwinned region form an angle of 86.3°. On the other hand, $\{10\bar{1}2\}$ twinning mode should not be easily activated in multi-pass rolling process since most of the grains tend to be oriented with c-axis almost perpendicular to the plane of the sheet. In this preferred orientation of crystallites, $\{10\bar{1}2\}$ twinning tends to

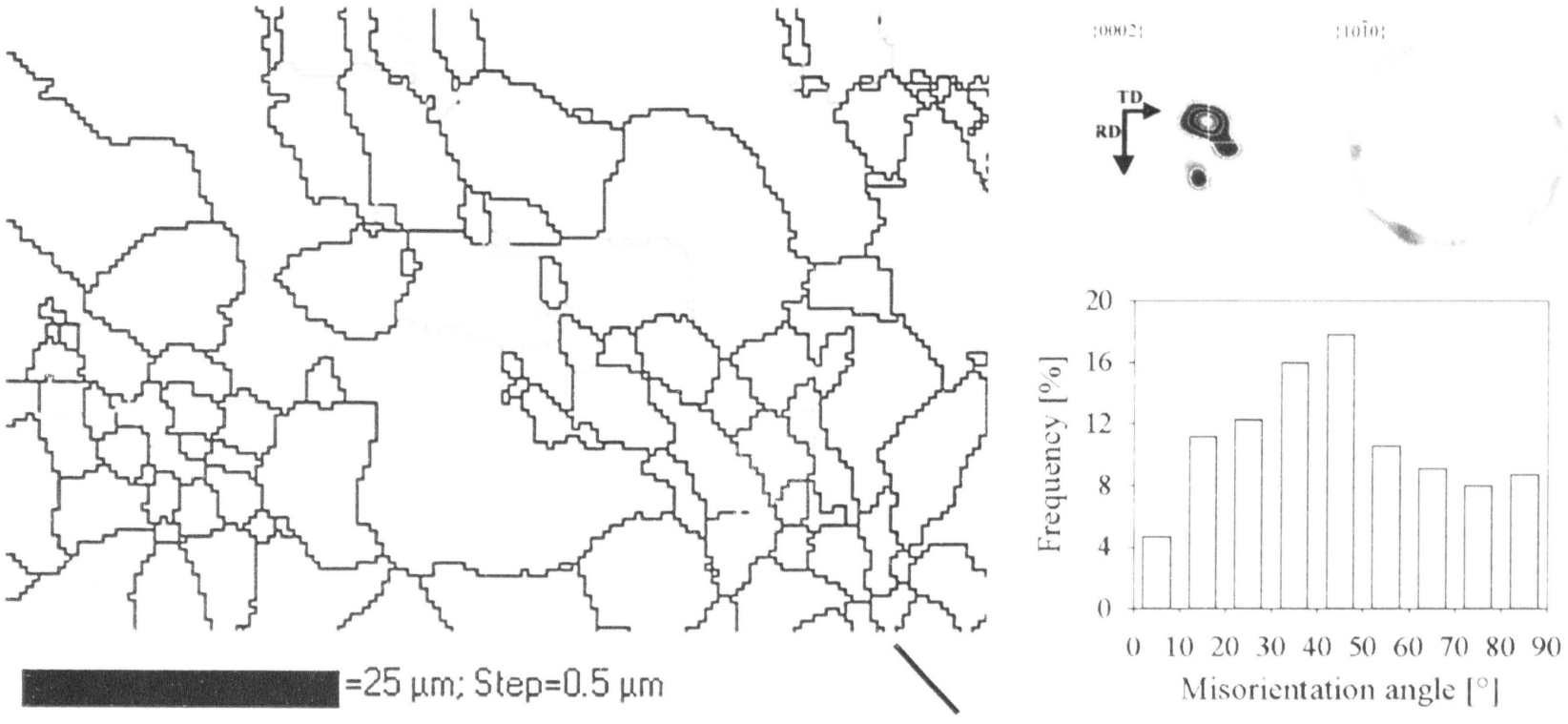

***Fig. 5.4**: Left: Orientation map (SEM-EBSD) of specimen annealed at 200 °C for 1h; RD in the left figure is horizontal and normal direction (ND) is perpendicular to the plane of orientation map. Right: Distribution of misorientation angles between nearest grains and direct pole figures from orientation map [Jager06].*

increase the thickness of the sheet and, thus, it is not able to accommodate compressive strain caused by rolling. Many authors, e.g. Wonsiewicz & Backofen [Wonsiewicz67] and Yoo & Lee [Yoo91], clearly demonstrated impossibility of strain accommodation by $\{10\bar{1}2\}$ twining in compression along the c-axis. Twining in the other systems, like $\{10\bar{1}1\}$, is also possible but more difficult and needs a higher elastic stress concentration to occur. The merit of $\{10\bar{1}1\}$ twinning follows from the ability to accommodate a strain imposed by rolling due to lowering of the sheet thickness and reorients crystals such that they may continue deforming by basal slip and/or secondary twinning. Secondary twinning on $\{10\,1\,1\}$ planes was demonstrated experimentally by Nave & Barnett [Nave04] and geometrical analysis was given by Wonsiewicz & Backofen [Wonsiewicz67].

The influence of annealing at 300 °C on the microstructure is shown in **Figs. 5.5a,b**. The mechanisms of the microstructure changes seem to be the same as at 200 °C, but the process of recrystallization is much quicker. By comparison of **Figs. 5.3** and **5.5a** it is clearly visible that the most significant changes occur within a few minutes. Two minutes of annealing at 300 °C are enough to fully recrystallize the microstructure and eliminate most of the twins, **Fig. 5.5a**. Further annealing results in a more homogenous microstructure with triple junctions in angle about 120°, **Fig. 5.5b.**

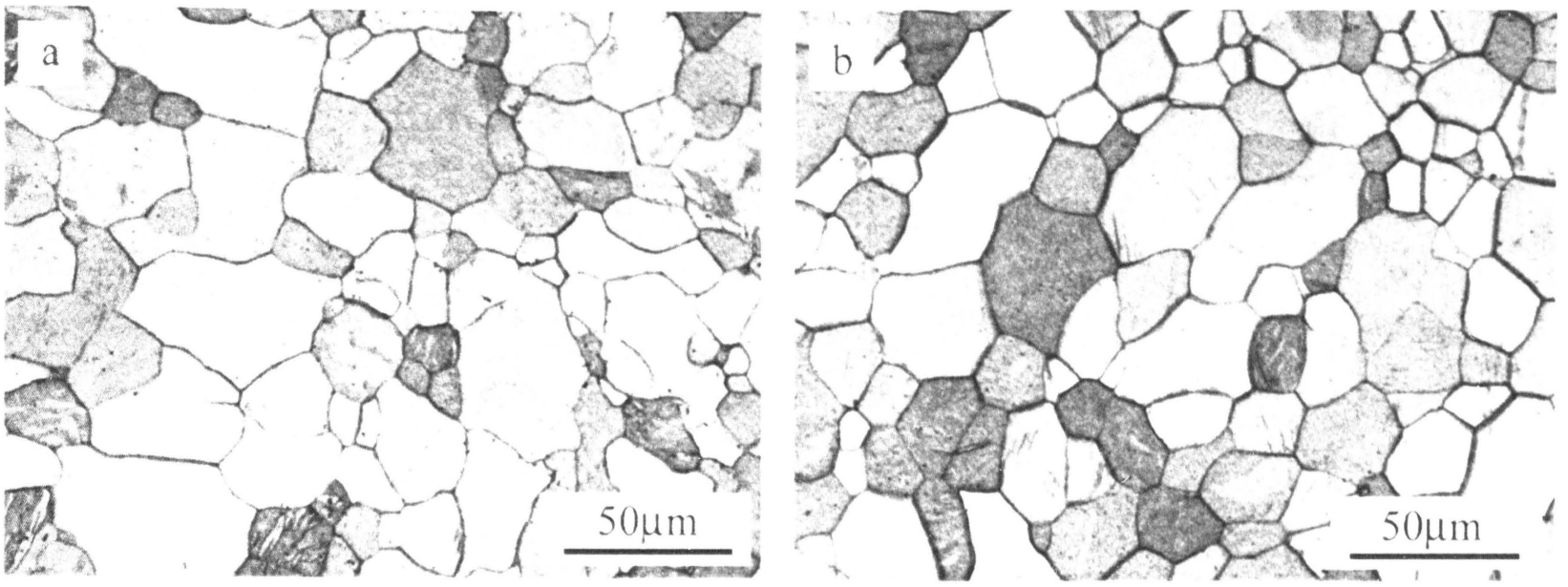

***Fig. 5.5a,b**: Typical microstructures of the annealed specimens at 300 °C for 2 min (a) and 24 h (b). The rolling direction is horizontal.*

Figures 5.6a,b,c demonstrate the role of twins during exposure of specimen to temperature. Mutual crossing of twins often nucleates new grains (**Fig. 5.6a**). The newly formed grains grow along the mutual crossing twins and exhibit like rectangular

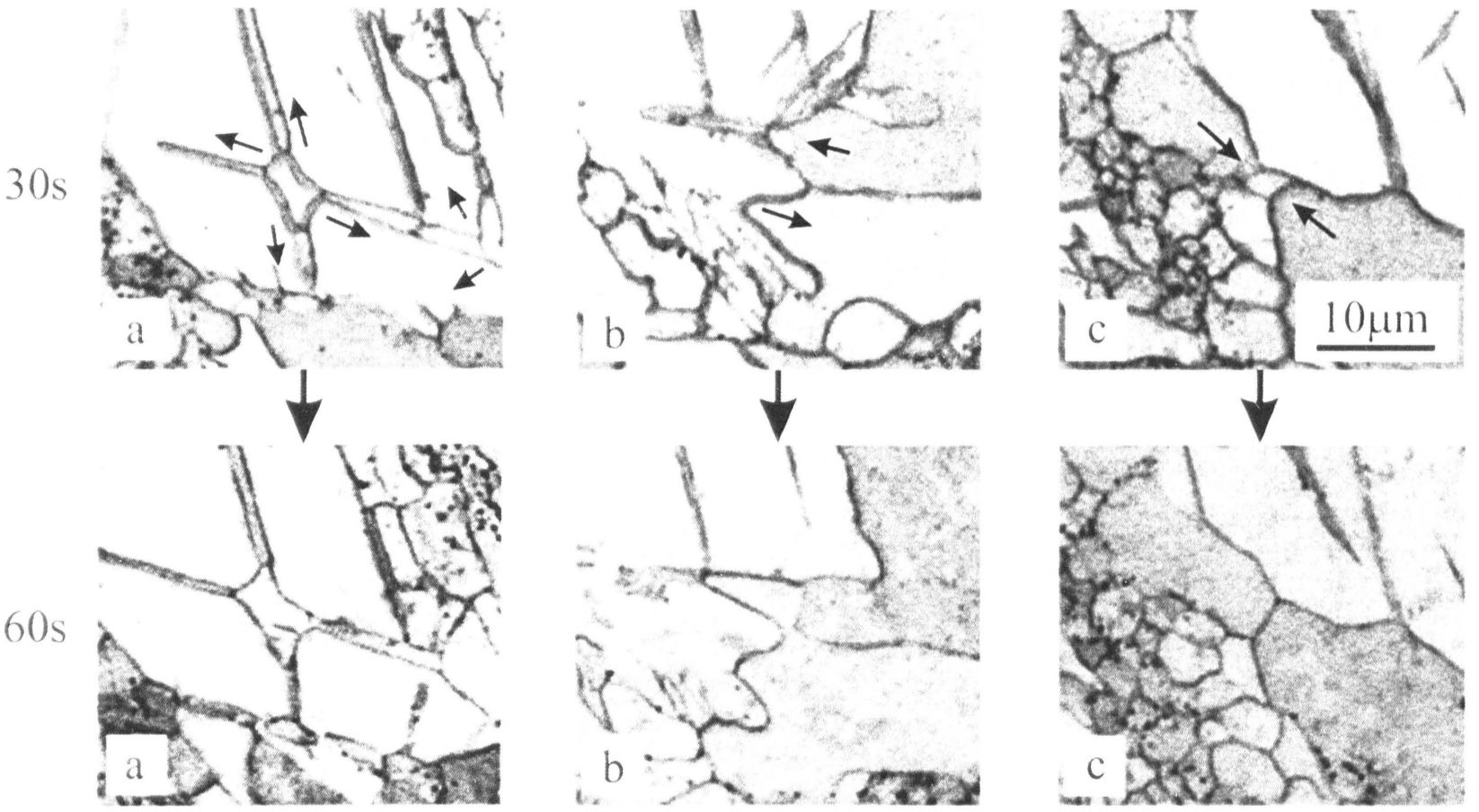

***Fig. 5.6a,b,c**: Microstructure evolution of the same sites after annealing for 30 and 60 s at 300 °C. The arrows in figures indicate moving of GB during annealing in the time range from 30 to 60 s (Light microscope).*

shape. Twins play no less important role during the grain growth (**Fig. 5.6a,b**). While a new grain boundary (GB) grows along a twin (**Fig. 5.6b** upper arrow), another one has no support for growing and, at least, decreases the GB energy by straightening (**Fig. 5.6b** lower arrow). Note that while twins facilitate grow of new grains, etching contrast on the twin/grain boundary indicates that crystallographic orientation may not be necessarily identical (**Fig. 5.6a,b**). This is because orientation of a new grain is

determined by crystallography of mutual twin intersection and influenced by internal stresses. It is worthy to note, that "predator" effect takes place as well, as can be seen in **Fig. 5.6c**. Some grains can grow from others, which are smaller and/or inconveniently oriented grains. Disorientation of grains is possible only by means of internal stresses accumulated in the material during previous straining and relaxed by increasing temperature. It was also recognised that some grains originate from twin lamellae and twin may be a nucleation site for several grain. It appears that twin planes serve as initial stages of the incoming high angle boundaries of recrystallized grains. This may be well seen in the upper right corner of **Fig. 5.6a**. Consequently, GB migration, rotation and diffusional processes build grains with high angle GBs and triple junction.

At 400 °C, annealing only for 60 s is sufficient to change the microstructure. It is evident that the onset of the microstructural changes had to occur during an increase of temperature from rt to 400 °C. The texture of the annealed (400 °C/2 h) sample is introduced in **Fig. 5.7**.

By comparison of **Figs. 5.2** and **5.7** it can be seen that pole figures prior and after static recrystallization show some differences. The as-received sample has a stronger (0001) preferred orientation. After SRX, the axis of "fiber" texture remains several degrees tilted from the direction perpendicular to the sample surface but not as tilted as the as-received sample. Due to the satisfactory symmetry of basal texture in RD-ND plane and TD-ND plane, distribution of crystallites around the dominant preferred orientation direction (0001) was approximated with 2D Gaussian function. Fitted values are shown in **Tab. 5.2**.

In the last two columns of **Tab. 5.2**, the **f**ull **w**idth in **h**alf of **m**aximum (FWHM calculated from the Gaussian function fit) in RD and TD direction is given. It is clearly seen from the measured pole figures (0002) and the FWHM in **Tab. 5.2** that the intensity is not rotational symmetrical, but is in one direction slightly broader; the (0001) pole intensity of as-received sample is more spread to the TD and recrystallized sample to the RD. After annealing, the maximum intensity of the (0002) pole figure significantly decreases and the FWHM of the Gaussian function approximating the distribution of crystallites around the dominant preferred orientation direction increases mainly in RD, **Tab. 5.2**. Symmetrical maxima observed in $(10\bar{1}1)$ and $(10\bar{1}3)$ pole figures (**Fig. 5.2**) disappear indicating disorientation of the $\langle 11\bar{2}0 \rangle$ direction. It is

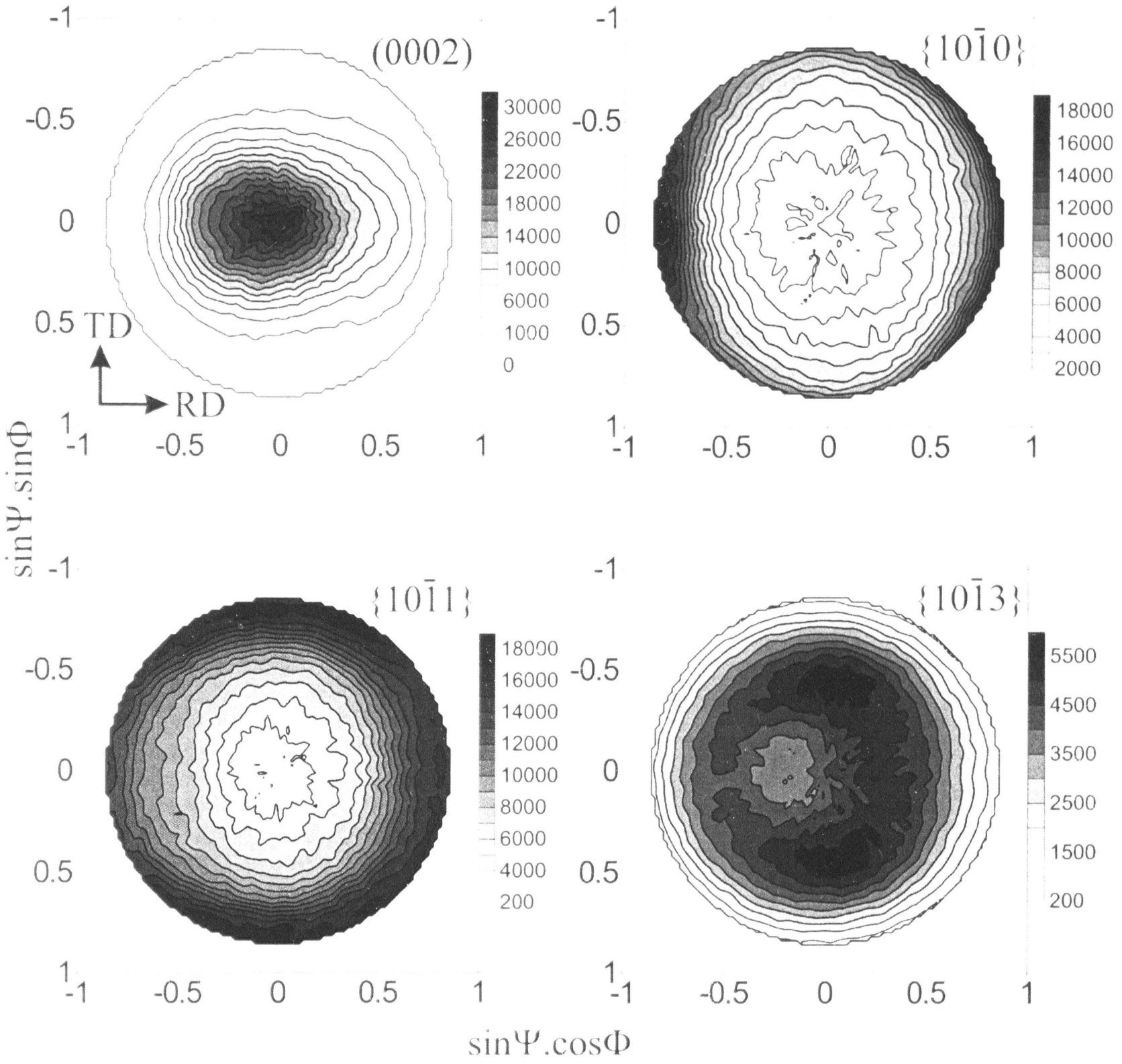

***Fig. 5.7**: Direct pole figures performed by X-ray diffraction technique on recrystallized specimen (annealed at 400 °C/2 h). RD and TD indicate rolling and transversal direction, respectively [Jager06].*

Sample	Imax [counts]	FWHM(RD) [deg]	FWHM(TD) [deg]
As-received	64902	17	26
Recrystallized	26959	44	33

***Tab. 5.2**: Parameters of the (0002) pole figures for as-received and recrystallized material; Imax refers about maximum intensity and FWHM(RD) and FWHM(TD) means **f**ull **w**idth of the peak in **h**alf of **m**aximum calculated from the Gaussian function fit in RD and TD, respectively.*

reasonable to expect that the lattice reorientation by twinning process must contribute to the weakening of the strong basal texture formed by rolling due to nucleation of grains from twins during SRX.

5.1.4. Deformation behaviour

The deformation behaviour was examined by uniaxial tension at a constant crosshead speed as described in chapter 4. Specimens with gauge dimensions 1.6x5x25 mm^3 were cut from the sheet with the tensile axis parallel to the rolling direction, **Fig. 5.8**. Kaiser et al. [Kaiser03] and Bohlen et al. [Bohlen04] showed that the deformation behaviour varies with orientation of the tensile axis to the rolling direction as a result of crystallographic anisotropy. They put forward clear evidence that both characteristic stresses (σ_{02} and σ_{max}) are systematically lower in rolling direction (RD) than those in transversal direction (TD) between rt – 300 °C.

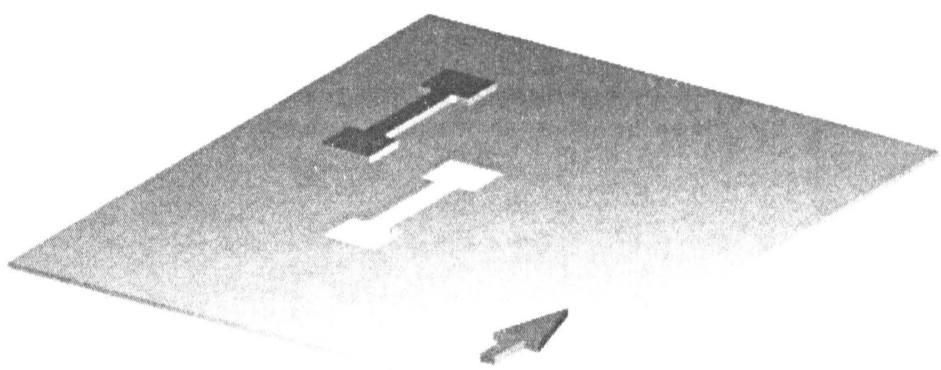

***Fig. 5.8**: Orientation of the tensile axis to the rolling direction (arrow) in AZ31 alloy.*

The tensile tests were conducted in a wide temperature range (rt-400 °C) and strain rates between $1.3x10^{-4}$-$4.5x10^{-2}$ s^{-1}. Typical true stress – true strain curves measured over the temperature range rt-400 °C at selected strain rate of $\dot{\varepsilon} = 4.5x10^{-2}\,s^{-1}$ are shown in **Fig. 5.9** (left). The effect of the strain rate on plastic deformation at temperature T = 350 °C is shown in **Fig. 5.9** (right). Similar true tress – true strain

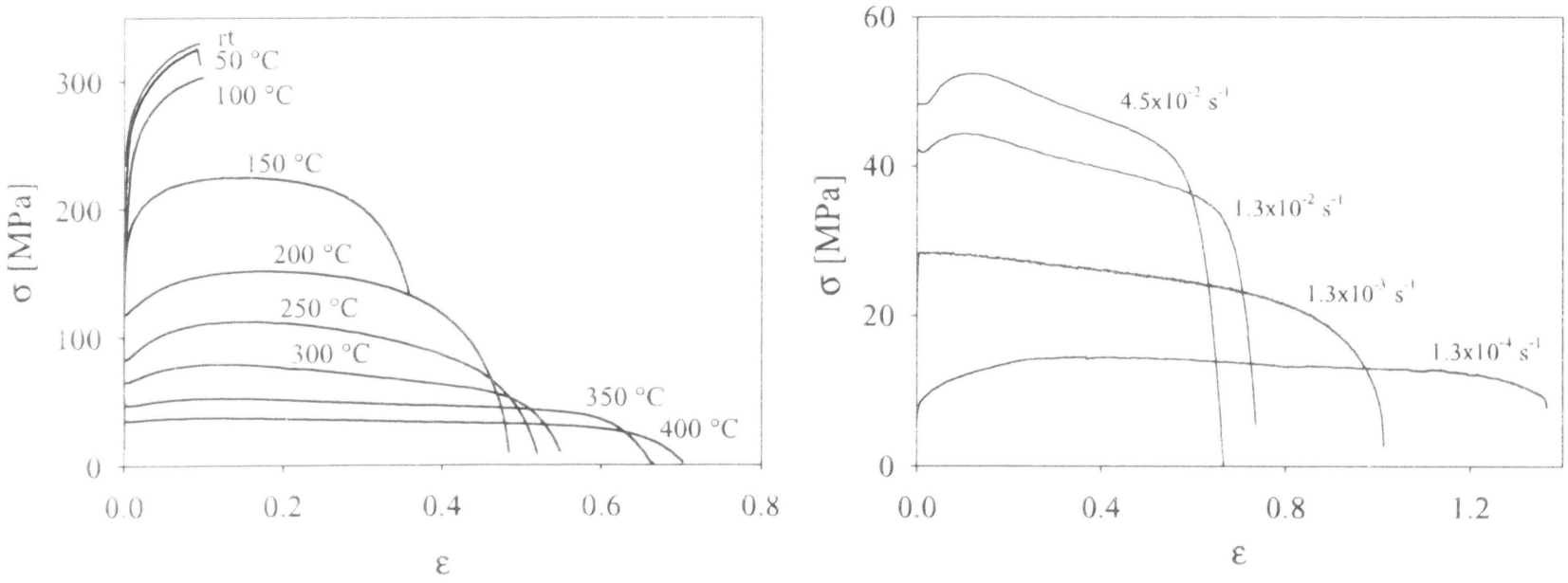

***Fig. 5.9**: True stress-true strain curves at a selected strain rate $\dot{\varepsilon} = 4.5x10^{-2}\,s^{-1}$ (left) and temperature T=350 °C (right).*

curves were obtained for the specimens tested at other combinations of the temperatures and the strain rates. It can be seen that deformation behaviour is influenced by the temperature and the strain rate. With increasing temperature and/or decreasing strain rate the deformation stress decreases, ductility increases and the course of $\sigma(\varepsilon)$ curves is getting flattened. Strain hardening dominates at temperatures rt-100 °C. Above 250 °C the work hardening rate is close to zero.

5.1.4.1. Influence of the temperature on plastic deformation

It has been stated in section 2.1 that one of the most important materials characteristic is the yield stress σ_{02} and the maximum stress σ_{max}. The temperature dependence of the both characteristic stresses at different strain rates $\dot{\varepsilon}$ is shown in **Fig. 5.10**.

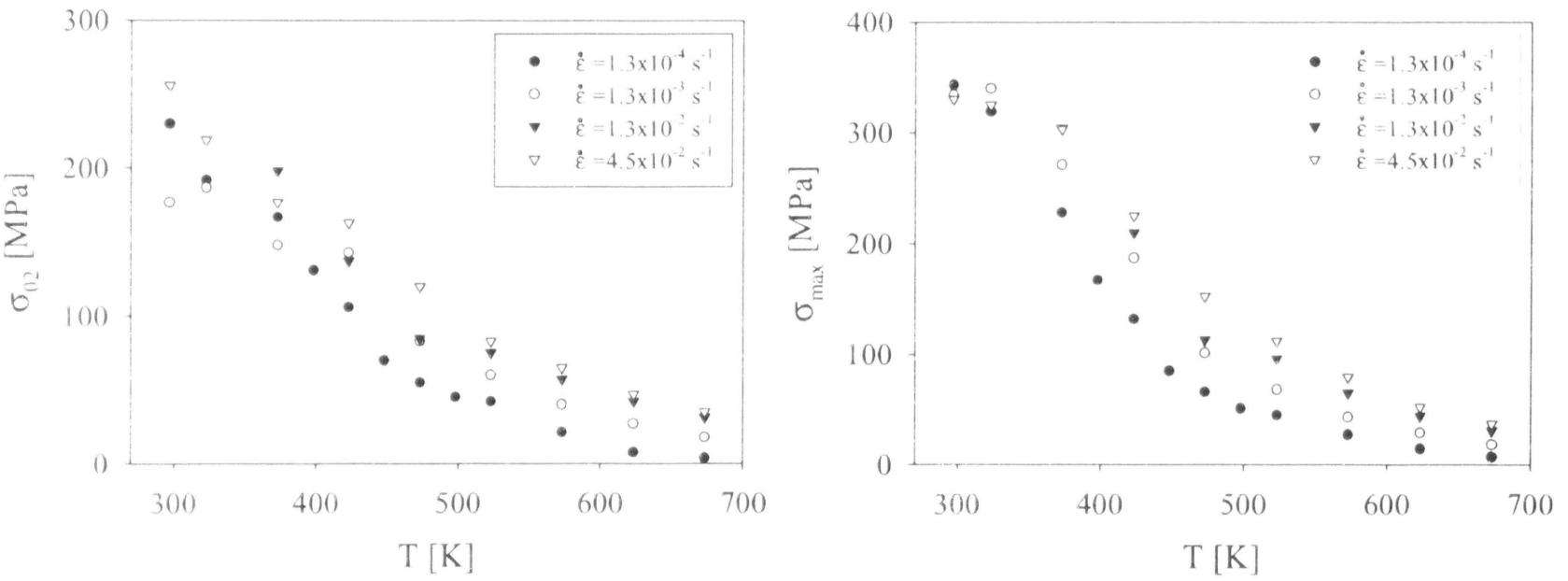

***Fig. 5.10**: The yield stress σ_{02} (left) and the maximum stress σ_{max} (right) as a function of temperature T at different strain rates.*

Both stresses gradually decrease with increasing temperature. The most apparent decrease takes place between 100 and 200 °C. Poor mechanical stability at higher T is attributed to the lack of an element that is able to trap the dislocations and stabilize the microstructure (see section 1.1.3). Hence, softening occurs. The mechanisms of softening are very probably cross slip and climb of dislocations.

For further treatment the maximum stress σ_{max} is considered. Logarithm and rearrangement of the relation 2.15 (or its modifications 2.16-2.17) described in section 2.2 yields proportionality

$$\ln(\sigma) \sim \frac{1}{T}$$

and the change of the slope in this plot indicate the change of Q and/or n. **Fig. 5.11** shows the dependence between $\ln(\sigma)$ and T^{-1}. It is readily seen that several regions may be discerned. At temperatures between rt and 50 °C the maximum stress σ_{max} is not significantly influenced by strain rate $\dot{\varepsilon}$ and temperature T. This indicates that the effect of thermally activated phenomena on plastic flow between rt and 50 °C is minor. At about 100 °C thermally activated phenomena begin to influence deformation process.

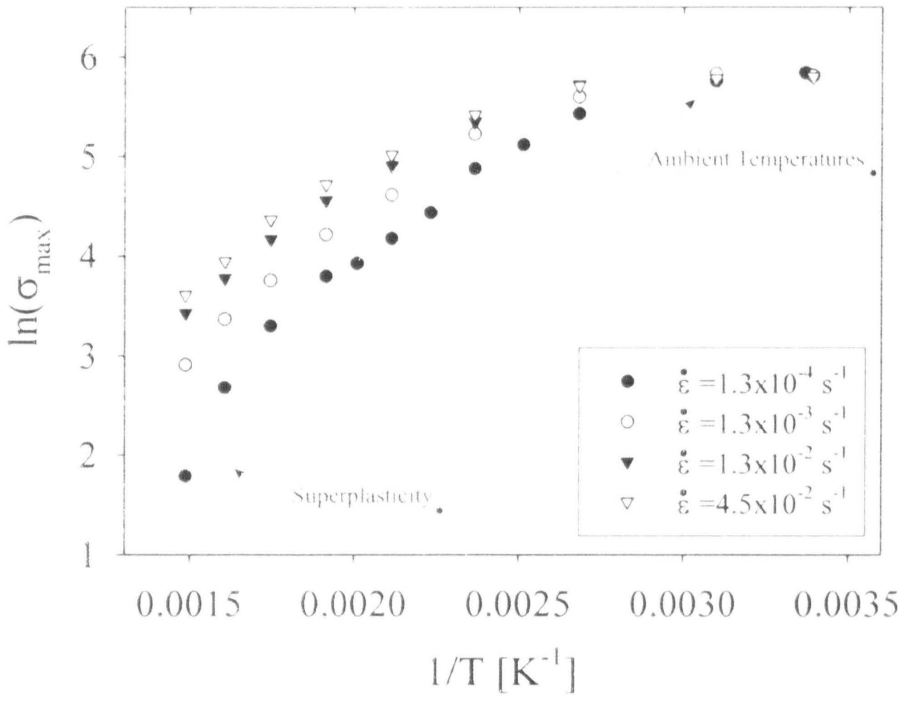

Fig. 5.11: Logarithm of the values σ_{max} as a function of T^{-1}.

In other words, the deformation behaviour starts to be very sensitive to the test temperature and imposed strain rate. This leads to the "splitting" of $\sigma(T)$ curves for different $\dot{\varepsilon}$ as may be seen in **Fig. 5.11**. At the highest temperatures (T > 300 °C) and the lowest strain rate $\dot{\varepsilon} = 1.3\text{x}10^{-4}\,s^{-1}$, the points markedly deviate from the rest of data. It will be shown bellow that this region corresponds with the superplastic behaviour. Therefore, the change of n and/or Q is apparent.

5.1.4.2. Influence of the strain rate on plastic deformation

As indicated in **Fig. 5.11**, the maximum stress at higher temperatures is sensitive not only to the test temperature T but also to the strain rate $\dot{\varepsilon}$. Taking into account a relation between σ and $\dot{\varepsilon}$, the best fit was obtained for $\sigma_{max} \sim \ln\dot{\varepsilon}$. The plot σ_{max} against $\ln\dot{\varepsilon}$ is shown in **Fig. 5.12**. If we consider creep equation at high stresses 2.7 (section 2.2) or the equation for activation energy 2.20 (section 2.2.1), then we can express the stress σ as a function of strain rate $\dot{\varepsilon}$. Logarithm and rearrangement leads to the same proportionality as observed by experiment, i.e. $\sigma \sim \ln\dot{\varepsilon}$. Quality of the fit

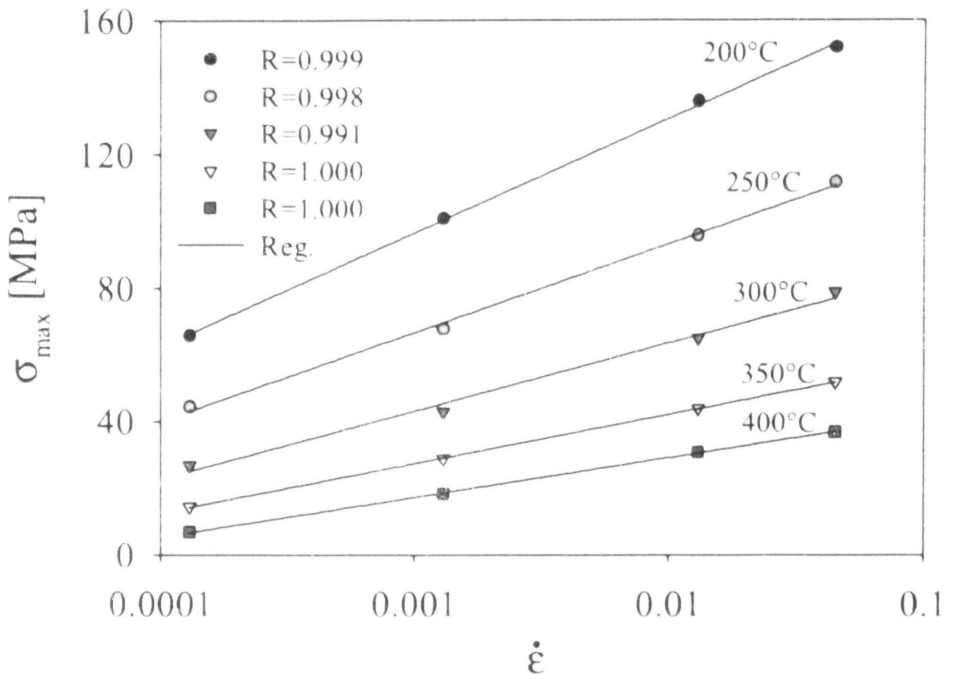

***Fig. 5.12**: Dependence of the maximum stress on the strain rate (in logarithmic scale) at high temperatures. Inset indicates quality of the fit.*

expressed by R-parameter in **Fig. 5.12** shows that proposed dependence is in excellent agreement with experimental data in the strain rate range $1.3\text{x}10^{-4}$-$4.5\text{x}10^{-2}$ s^{-1}. This is not surprising; it is well known that creep data at high stresses (i.e. high strain rates as well) correlate with proportionality $\sigma \sim \ln\dot{\varepsilon}$ [Sherby68 (p.341, 360)]. **Fig. 5.13** shows the slope χ of the regression curves in **Fig. 5.12** as a function of the temperature. It can be seen that the slope χ monotonically decreases with increasing temperature.

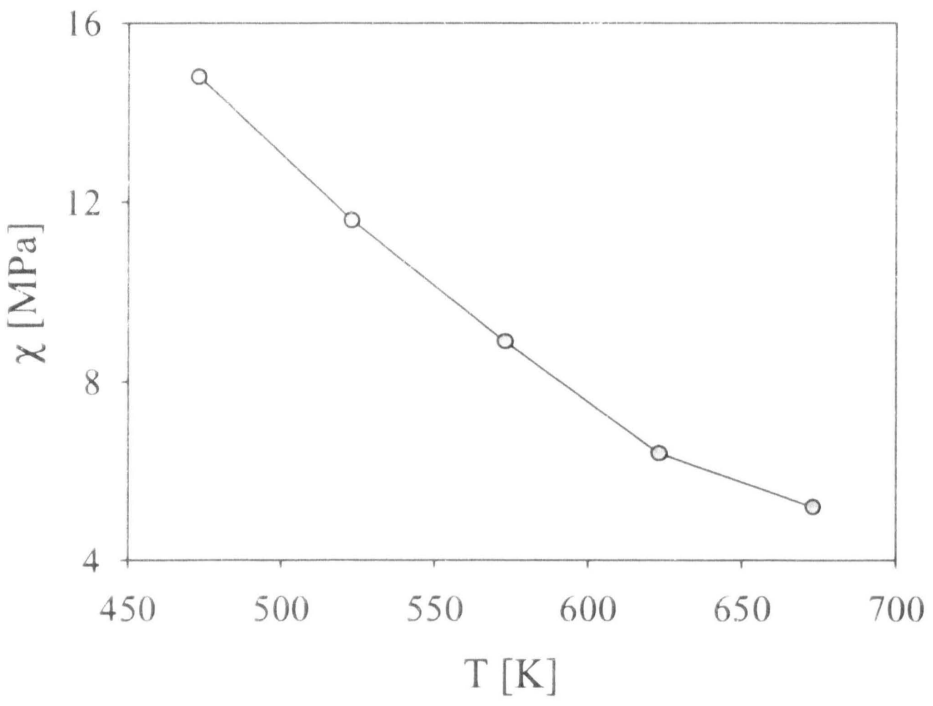

***Fig. 5.13**: Slope of the regression curves in **Fig. 5.12**.*

According to equation 2.20 (section 2.2.1) the slope χ of the regression curves corresponds with

$$\chi = \frac{R_m T}{V} . \qquad 5.1$$

Since increasing temperature in equation 5.1 results in an increase of the slope χ, experimentally observed decreasing dependence in **Fig. 5.13** should be compensated by an increase in the activation volume V.

5.1.4.3. Micromechanisms of plastic deformation at ambient temperatures

In order to study micromechanisms of plastic deformation at ambient temperatures we used the stress-strain curves measured at rt and at strain rate of $\dot{\varepsilon} = 1.3\text{x}10^{-4}\,\text{s}^{-1}$. For different initial microstructures **(Fig. 5.3)** significant differences in the course of the stress-strain curves were observed as shown in **Fig. 5.14a**. Substantial differences indicate changes in the obstacle density hindering motion of dislocations. It is expected that the dislocation density in the annealed specimen is lower than that in as-received specimen.

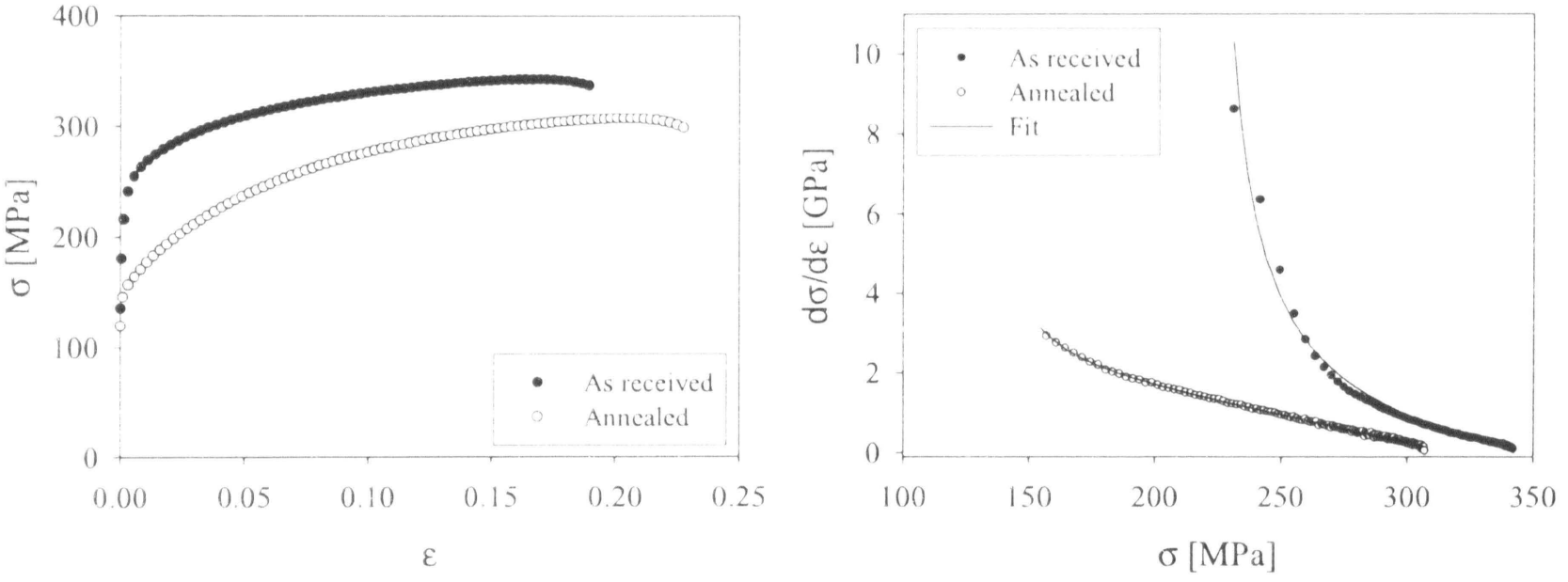

Fig. 5.14a,b: *a) True stress - true strain curves at rt and* $\dot{\varepsilon} = 1.3\text{x}10^{-4}\,\text{s}^{-1}$ *for two different initial microstructures: as-received and annealed (400 °C/2h). b) The dependence of hardening coefficient* $\vartheta = d\sigma/d\varepsilon$ *on the true stress* σ*. Experimental results (circles) fitted by Lukac-Balik model (eq. 5.2).*

In comparison with the $\sigma(\varepsilon)$ dependence for annealed alloy, as-received specimen does not show so intensive strain hardening. Flat shape of the $\sigma(\varepsilon)$ curves is a characteristic feature observed in the materials previously submitted to the intensive deformation. Since a material already contains a high density of the obstacles (twins, dislocations,...) prior deformation, its defect-accumulation abilities are limited. Stress fields from these defects and mutual interaction of moving and sessile dislocations make a straining more difficult. Moreover, twin boundaries may serve as effective barriers for moving dislocations. In order to support our assumptions, $\sigma(\varepsilon)$ data were fitted with the help of Lukac-Balik model

$$\vartheta = \frac{d\sigma}{d\varepsilon} = A/(\sigma - \sigma_y) + B - C(\sigma - \sigma_y) - D(\sigma - \sigma_y)^3 \qquad 5.2$$

where A describes obstacles of non-dislocation type (grain boundaries, twin boundaries,...), B is connected with obstacles of dislocation type, C describes cross slip, D climb of dislocations and σ_y should be of the same magnitude as the yield stress σ_{02}. The constants A and B are temperature independent. A detailed description of the model is published in [Lukac94]. The application of Lukac-Balik model on experimental data supports our considerations. Due to complexity of the AZ31 alloy and simplicity of Lukac-Balik model, which describes deformation behaviour by means of five fitting parameters (A, B, C, D and σ_y), it is reasonable to elucidate fitted results only qualitatively, **Tab. 5.3** and **Fig.5.14b**. The higher value of coefficient A for as-received alloy in comparison with annealed one favours the stress fields around grain boundaries and twins as a major hardening mechanism. In contrast, dislocations serve as dominant obstacles in annealed alloy as indicated by differences in coefficient B. Parameter C is practically the same for both microstructures. This indicates a similar activity of the cross slip in both specimens. Climb of dislocations is negligible at rt and thus a low value of D parameter connected with diffusion processes can be accepted. Lower value of R in **Tab. 5.3** for as-received alloy may be a consequence of non-equilibrium state.

Specimen	σ_{02} [MPa]	σ_{max} [MPa]	A_0 [%]	A [MPa^2]	B [MPa]	C	D [MPa^{-2}]	σ_y [MPa]	R
As-received	212±18	338±5	21±1	131000	5.2e-5	8	1.2e-11	218	0.98
Annealed	151±2	308±1	26±1	31500	1978	10	3.3e-5	132	0.998

Tab. 5.3: *Characteristic stresses (σ_{02}, σ_{max}) and elongation to fracture A_0 for specimens deformed at rt ($\dot{\varepsilon} = 1.3\text{x}10^{-4}\ s^{-1}$) for two different initial microstructures; A, B, C, D and σ_y are fitting parameters and R-values introduce a quality of the fit.*

Similar procedure was performed on the as-received specimens in the temperature range from rt to 125 °C, **Tab. 5.4**. At higher temperatures the microstructure may change due to recrystallization that is not involved in the model. Therefore, 125 °C was selected as an upper fitting limit.

It can be seen that parameters C and D increase with increasing temperature which is consistent with the model. Temperature independence of the A and B is roughly fulfilled as well. A is constant up to 100 °C but decrease at 125 °C and B is

constant up to 50 °C, then decreases and it is constant again. Since a correlation coefficient R indicating quality of the fit is not high, the fits may only serve as a support for the results at rt.

Temperature [°C]	σ_{02} [MPa]	σ_{max} [MPa]	A_0 [%]	A [MPa^2]	B [MPa]	C	D [MPa^{-2}]	σ_y [MPa]	R
rt	212±18	338±5	21±1	131000	5.2e-5	8	1.2e-11	218	0.98
50	202±7	316±3	33±2	112000	5.2e-5	10.1	2.0e-11	203	0.98
100	166±4	228±5	48±1	130000	3.3e-5	23.8	5.5e-11	156	0.97
125	131	167	52	51000	3.3e-5	28.6	2.7e-10	123	0.97

***Tab. 5.4**: Characteristic stresses (σ_{02}, σ_{max}) and elongation to fracture A_0 for as-received specimens deformed in the temperature range rt-125 °C ($\dot{\varepsilon} = 1.3\text{x}10^{-4}\ s^{-1}$); A, B, C, D and σ_y are fitting parameters and R-values introduce a quality of the fit.*

The elongation to fracture at rt for as received (A_0 = 21%) and annealed (A_0 = 26%) specimens is unusual for Mg alloys and it is not possible to explain these values only by the activity of basal dislocations or $\{10\bar{1}2\}$ twinning. It is evident from pole figures (**Figs. 5.2** and **5.7**) that orientation of the basal planes and $\{10\bar{1}2\}$ twinning to the tensile axis is not appropriate for easy deformation. On the other hand, dislocations lying in pyramidal planes are oriented properly. But the critical resolved shear stress (CRSS) for the non-basal slip of Mg single crystals at room temperature was reported to be much higher (~100x) than that for the basal slip, e.g. [Stohr72, Akhtar69, Akhtar69a]. However, this value can be lowered e.g. by texture, by alloying and, in case of polycrystals, by stress fields coming from dislocation pile-ups at GBs. Indeed, Lukac [Lukac81] put forward evidence that alloying modifies the CRSS ratio of the basal to the non-basal slip. Similarly, Koike et al. [Koike03] showed that non-basal dislocations are much more active in the AZ31 alloy prepared by equal channel angular pressing if deformed at rt. They determined the CRSS ratio of the basal slip to non-basal slip to be of the two orders of magnitude lower than that of single crystals [Koike03]. Deformation simulations presented in the literature also assume much smaller value of the CRSS for rolled AZ31 than reported for single crystals, e.g. [Styczynski04, Agnew03]. It means that structural parameters and composition play an important role in the activity of slip systems. The lower value of A_0 for as received alloy in comparison

with annealed one is likely caused by the stress concentrations, which, on the one hand, may serve as a support for activity of non-basal slip system, but on the other hand can initialise the crack.

It is worth to note negligible deviation of A_0 from mean value (two specimens tested for each microstructure and/or temperature), **Tab. 5.4**. The elongation to fracture is, in general, very sensitive to the defects (cavities, inclusions) introduced during production process. It is apparent that such insignificant deviation refers about high quality of the material studied.

5.1.4.4. Ductility at high temperatures and superplasticity

The effects of strain rate $\dot{\varepsilon}$ and temperature T on plastic flow is analysed in this section. A particular attention is dedicated to the ductility, which is a function of temperature and initial strain rate. It is shown that strain rate and temperature strongly influence neck-free deformation and microprocesses acting during plastic deformation.

Detailed microstructural evolution of the rolled AZ31 alloy exposed to the influence of temperature is described in section 5.1.3. Herein it is sufficient to mention that as-received microstructure undergo to the static recrystallization at T~>200 °C, thereby the microstructure during heating to the set temperature is losing the defects (twins, dislocations) accumulated in rolling. The grain size, however, remains more or less unchanged after complete recrystallization (**Fig. 5.3**, section 5.1.3). Strong texture, the characteristic feature of all wrought Mg alloys, is weakened upon static recrystallization but does not disappear. It follows that unfavourable orientation of basal planes, which are almost parallel to the tensile axis, is partially maintained at the beginning of the tensile tests at higher temperatures.

Fig. 5.15 illustrates typical plots of the true stress σ versus true strain ε at higher homologous temperatures (at $T \geq 0.5T_m$, T_m being melting point of Mg) and at different initial strain rates (1.3×10^{-4} to 4.5×10^{-2} s^{-1}). As strain rate decreases and/or temperature increases the course of the $\sigma(\varepsilon)$ curves is getting flattened and the maximum stress σ_{max} approaches yield stress σ_{02}. Thus, close values of both characteristic stresses indicate steady state flow stress or, in other words, dynamic equilibrium between hardening and softening processes occurs.

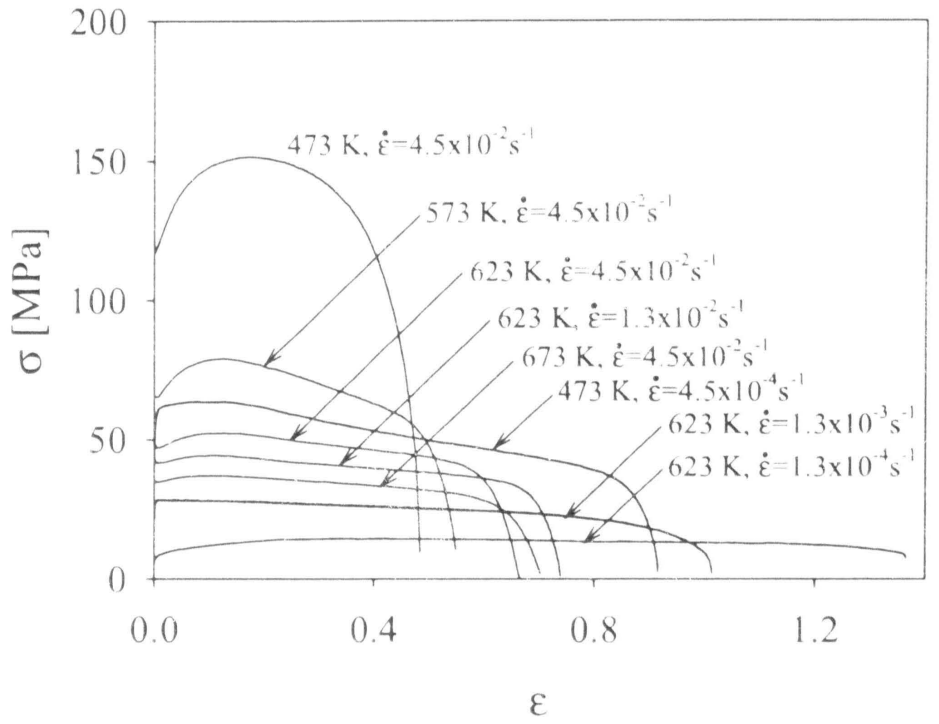

***Fig. 5.15**: Characteristic tensile true stress-true strain curves at different initial strain rates and temperatures. Note flattening of the curves as strain rate decrease and/or temperature increase.*

While at $1.3x10^{-4}s^{-1}$ σ_{02} and σ_{max} coincide at and above 523 K, their overlapping is shifted to a temperature of 623 K at $4.5x10^{-2}s^{-1}$, **Fig. 5.16**.

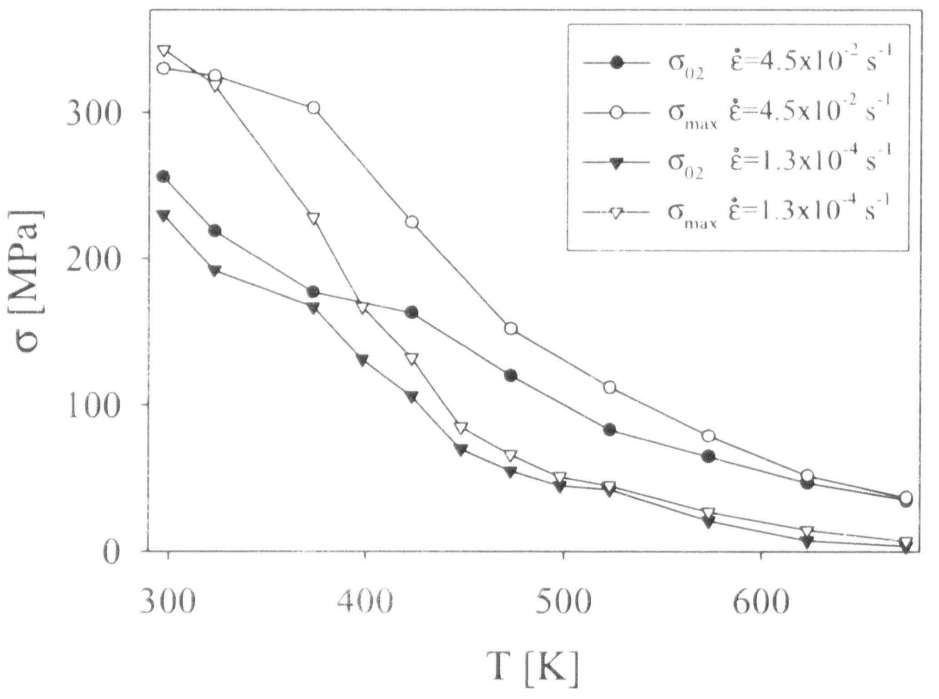

***Fig. 5.16**: Maximum true stress σ_{max} and yield stress σ_{02} as a function of temperature T at $1.3x10^{-4}s^{-1}$ and $4.5x10^{-2}s^{-1}$ [Jager04, Jager04a].*

As pointed above, a steady state flow stress at high temperatures indicates the dynamic equilibrium between hardening and softening but does not refer about strain accommodation mechanisms. Differences in the elongation to fracture A_0 and plateau stress σ_{max} indicate miscellaneous micromechanisms acting during plastic deformation and their sensitivity to the external conditions. **Fig. 5.17a** shows the temperature dependence of the elongation to fracture A_0. The higher the temperature the higher the ductility is observed. This is consistent with the fact that softening processes, which are activated at higher T, promote ductility. It is also observed that as strain rate decreases

ductility increases. For further elaboration it is useful to consider contribution of the failure region (i.e. necking) to overall elongation. **Fig. 5.17b** depicts necking Y as observed after deformation. The values of Y were calculated by using the relation $Y= s_b/s_n-1$, where s_b is a width of the uniaxially deformed part and s_n is a width (necking) near the fracture surface, see inset in **Fig. 5.17b**. The s_n values were measured as close as possible to the fracture and the s_b values were measured in the middle part of the uniaxially deformed specimen. Necking is usually determined by the ratio of undeformed and deformed cross sections but flat shape of the specimens caused

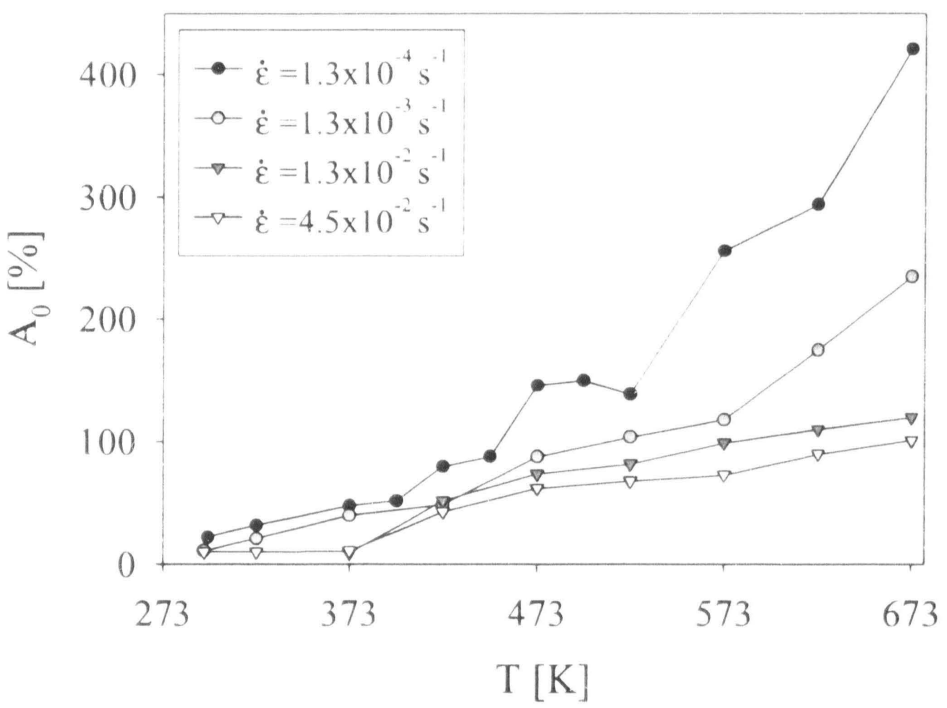

Fig. 5.17a: *Ductility A_0 as a function of temperature T at different strain rates.*

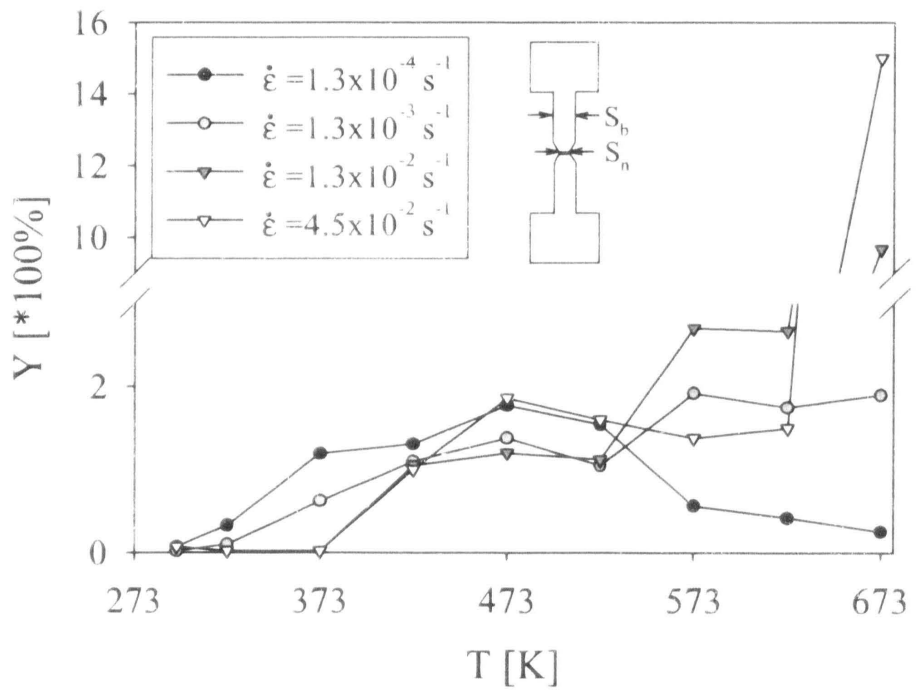

Fig. 5.17b*: Necking Y after fracture for different temperatures and initial strain rates. Necking was determined from the width of specimen and computed according to the relation $Y= s_b/s_n-1$, where s_b and s_n are uniaxially deformed and necked width, respectively, as sketched in the inset.*

difficulties with accurate determination of the specimen thickness after deformation. The lower the number on y-axis the lower contribution of necking and vice versa; hence, necking-free deformation indicates either abrupt fracture in the strain hardening

region or superplasticity; in contrast, necking (i.e. high Y) is one of the modes of ductile flow in materials deformed in tension (**Figs. 5.18** and **5.19**).

As it is seen in **Fig. 5.17a,b**, at ambient temperatures, the fracture occurs suddenly in the strain hardening region. However, at temperatures near the upper limit of usability of AZ31 (~400 K) and at low strain rates ($\leq 10^{-3}$ s^{-1}), slight tendency to necking (Y~1) can be seen. Note the local maxima of Y at 473 K for the all strain rates tested. The specific reason for its occurrence is under further investigation but as the most probable seems to be the microstructure development. This may be caused by recrystallization, by the activity of non-basal dislocations or by the change of deformation mechanism. At T > 523 K the behaviour strongly depends on the strain rate applied. While at $1.3x10^{-4}$ s^{-1} and T = 673 K necking-free deformation was observed and the elongation to fracture A_0 reached 420% (**Fig. 5.18**), at a strain rate of $4.5x10^{-2}$ s^{-1} and T = 673 K needle-like necking was observed with A_0 = 100% (**Fig. 5.19**) [Jager04, Jager04a]. The elongation to failure at $\dot{\varepsilon} = 1.3x10^{-4}$ s^{-1} and above 300 °C indicates superplastic behaviour, **Fig. 5.18**. It means that grain boundary sliding is the rate controlling process during superplastic flow accumulated by dislocation glide and/or diffusion.

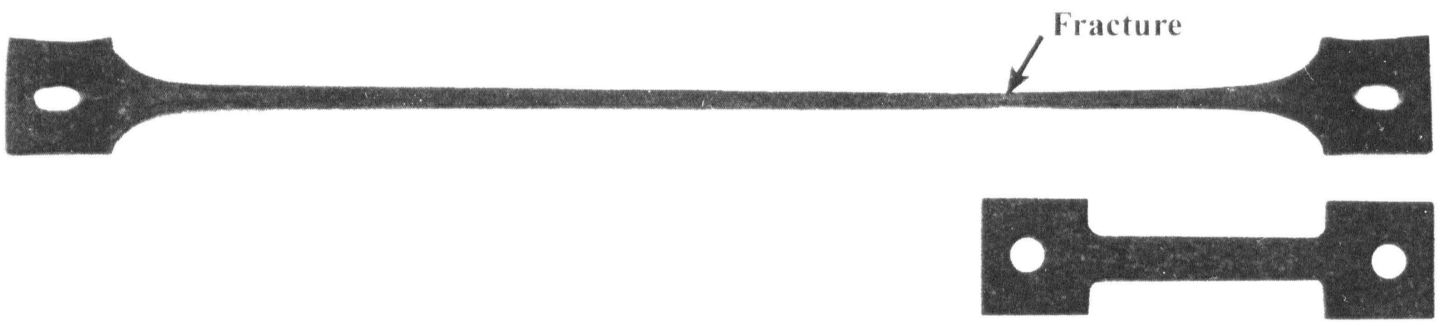

***Fig. 5.18**: Superplasticity of AZ31 alloy at T = 400 °C and* $\dot{\varepsilon} = 1.3x10^{-4}$ s^{-1}.

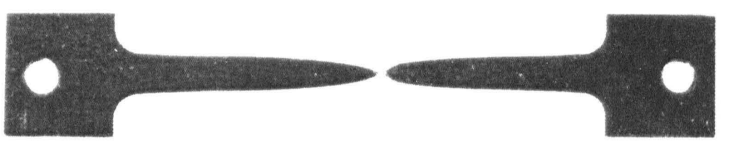

***Fig. 5.19**: Very ductile specimen with needle-like necking deformed at T = 400 °C and* $\dot{\varepsilon} = 4.5x10^{-2}$ s^{-1}.

The strain rate sensitivity m calculated according to equation 1.7a (section 1.2.5) is shown as a function of the temperature in **Fig. 5.20**. Relatively low strain rate sensitivity m at a strain rate ~10^{-2} s^{-1} (**Fig. 5.20**) is not able to "protect" material against deformation instabilities such as necking and this once initiated will further develop up to the failure. The m value at $\dot{\varepsilon} = 1.3x10^{-4}$ s^{-1} and T = 300 °C is almost equal to 0.3,

which is believed to be a minimum value for the occurrence of superplasticity and gradually increases up to 0.7 at 400 °C.

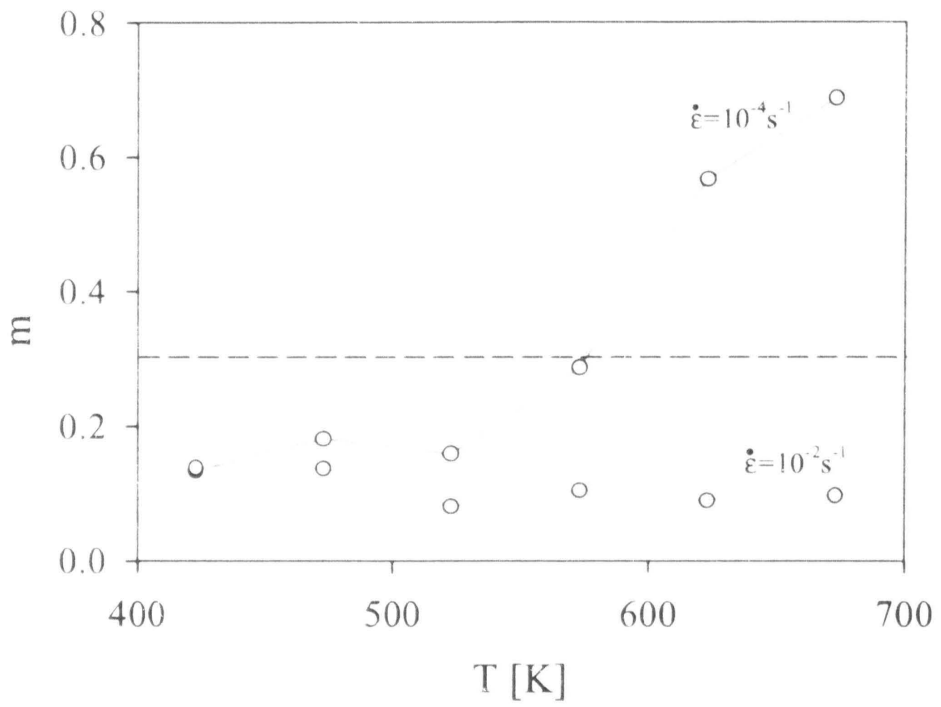

***Fig. 5.20**: Strain rate sensitivity m as a function of the test temperature T at two markedly different strain rates indicated in figure. Dashed line depicts "limit of SP".*

The above results (**Figs. 5.17b** and **5.19**) clearly indicate that necking is formed at high strain rates $\dot{\varepsilon}$ and high temperatures T. Wray [Wray70] recognised that several active necks may form along the length of specimen at both low and high strain rates. Unlike the tests at low strain rates, the high strain rate deformation involve unequal rate of grow of concurrently active necks, resulting in the final ascendancy of a single neck [Wray70]. Thereafter, deformation is concentrated to the necking region and elsewhere in the length gradually ceases as neck develops. Nevertheless, the exact onset of plastic instability can be hardly discerned [Padmanabhan80 (p.22)] since it is hindered by the amount of overall strain attained in a deformation beyond a slight maximum stress σ_{max} (post-uniform elongation). Hutchinson & Neale [Hutchinson77] showed that post-uniform elongation strongly depends on the strain rate sensitivity m; even negligible increase in m may result in a ductility enhancement of tens percent. Therefore, a ductility enhancement beyond σ_{max} at higher strain rates ($\sim 10^{-2}$) and $T \geq 573$ K in **Fig. 5.15** may be correlated with the m value of about 0.1, which is not sufficient to prevent material from necking, but it is enough to postpone failure.

At relatively high strain rates $\sim 10^{-2}$ s^{-1} and high temperatures, the main contribution to the overall strain from grain boundary (GB) processes such as diffusion along GBs and GB sliding is not expected since they are generally characterized by high strain rate sensitivity m that often approaching one. Taking into account grain size of the material investigated, these processes may be typical for low deformation rates and

high T. Low strain rate sensitivity for $\dot{\varepsilon} \sim 10^{-2}\ s^{-1}$ in **Fig. 5.20** indicates rather frequently observed dislocation mechanisms (glide and/or climb). On the other hand, it is reasonable to expect that GB sliding and diffusion may operate concurrently with motion of dislocations.

A sufficient number of available slip systems may significantly contribute to the homogeneity and, thus, postpone a fracture. The activity of non-basal slip systems accompanied with rapid recovery at higher homologous T is essential to explain the elongation to fracture $A_0 \sim 100\%$ at $\dot{\varepsilon} \sim 10^{-2}\ s^{-1}$. It is speculated in literature [Stohr72, Obara73] that the activity of second-order pyramidal slip systems with components $\{11\bar{2}2\}$ and **c+a** Burgers vector with direction $\langle 11\bar{2}3 \rangle$ is of prime importance to insure arbitrary shape change desirable for homogeneous deformation since this type of slip can easily accommodate any strain along the c-axis. It may be seen from **Fig. 5.15** that deformation at $\dot{\varepsilon} \sim 10^{-2} s^{-1}$ and $T \geq 573$ K requires the activity of sufficient number of slip systems (because A_0 is relatively high) acting simultaneously with recovery processes (because strain hardening is negligible). The activity of the second order pyramidal slip systems may lead to the interaction between **a** and **c+a** dislocations. Some dislocation reactions may result in annihilation of dislocations and, therefore, to an increase in the elongation to failure.

It has been demonstrated that the course of the stress-strain curves at elevated temperatures is very sensitive to the testing temperature and initial strain rate. In order to obtain a steady state flow stress, however, a decrease of the strain rate may be partly replaced by an increase of temperature and vice versa. But strain accommodation mechanisms, homogeneity of plastic deformation, elongation to fracture A_0 and stress of the plateau σ_{max} may significantly differ.

5.1.4.5. Constitutive analysis at high temperatures

In the constitutive analysis, the effects of temperature T and strain rate $\dot{\varepsilon}$ on flow stress σ_{max} were adequately expressed by the following equation [Mwembela97, Myshlyaev02] (see eq. 2.14 in section 2.2 and eq. 2.21 in section 2.2.2)

$$k_8 \sinh(\alpha\sigma)^n = \dot{\varepsilon} \exp\left(\frac{Q}{R_m T}\right) = Z \qquad 5.3$$

where k_8, n, α and Q are materials constants. The activation energy Q of magnesium for GB diffusion and dislocation core diffusion is 92 kJ/mol and for lattice self-diffusion 135 kJ/mol [Frost82 (p.44)]. A broad collection of creep results has been correlated with Q = 135 kJ/mol the activation energy for lattice self-diffusion of magnesium, e.g. [Kassner00 (p.16), Myshlyaev02, Shi94]. This value was used to fit coefficient α in equation 5.3 by using of the "solver" routine in MS Excel. The procedure consists in a series of iterative least-squares analysis aimed at the optimisation of data fit by a proper selection of Q. The results of the fit are shown in **Fig. 5.21**.

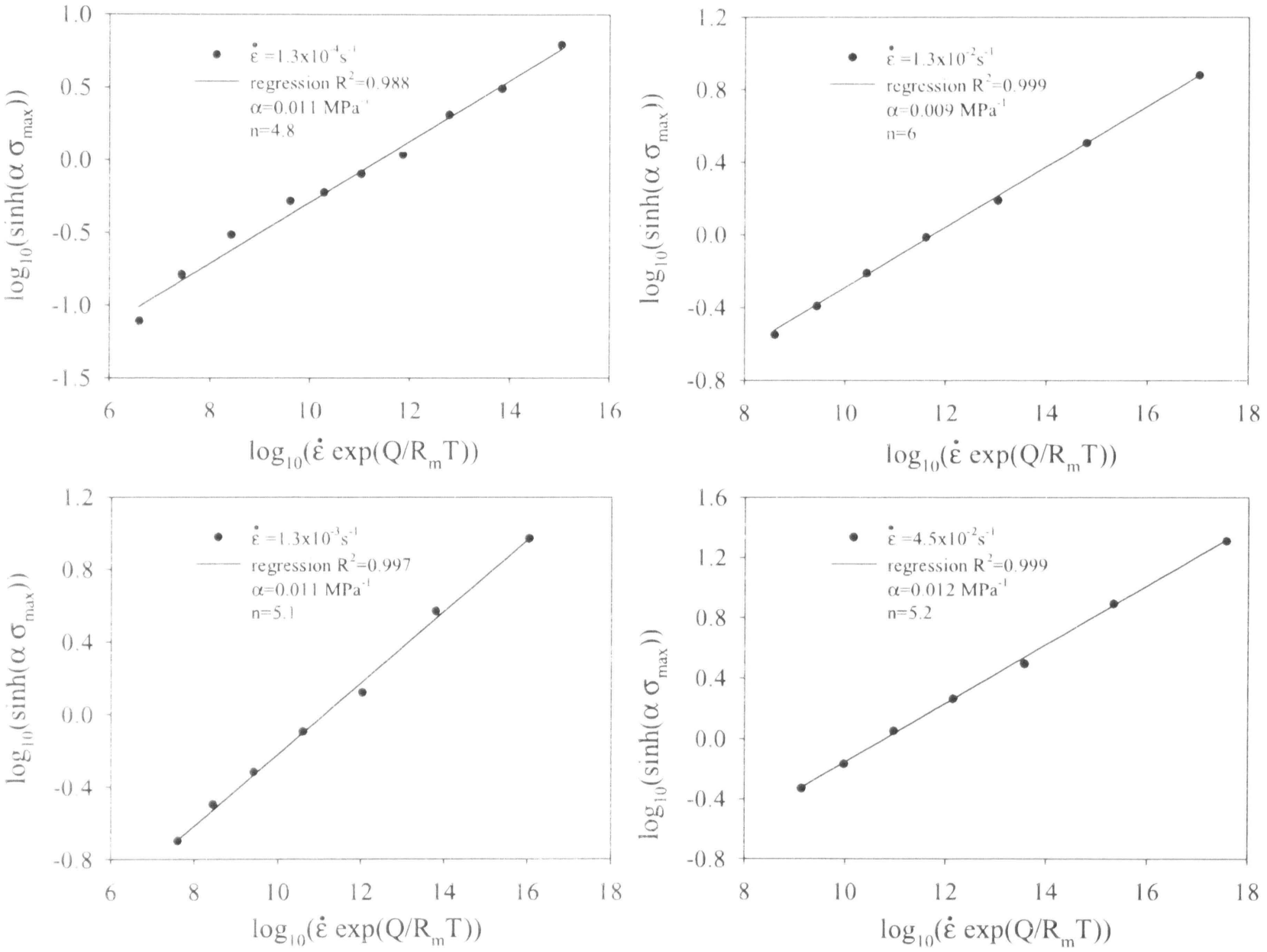

***Fig. 5.21**: Constitutive analysis according to the equation 5.3 for Q=135 kJ/mol. Quality of the fit expressed by a correlation coefficient R, fitted α-values and exponent n are given in graphs.*

It is readily seen from correlation coefficient R that the proposed dependence describes well (much better than [Mwembela97] for torsion) experimental data but for the lowest strain rate. Deficiency in the fit at $\dot{\varepsilon} = 1.3\text{x}10^{-4}\ s^{-1}$ follows from the scatter of points on the line likely because deformation consists of two regions: „conventional" at intermediate temperatures and superplastic at high temperatures. Taking into account strain rate sensitivity m (**Fig. 5.20**) as a parameter separating both regions, we obtain

two temperature intervals, which should be solved separately: $T < 300$ °C and $T \geq 300$ °C. It is reasonable to expect that these two regions are described by different values of materials parameters. Reciprocal values of the slope in **Fig. 5.21** determine exponent n in equation 5.3. It may be seen that the exponent n is about 5 for all the strain rates $\dot{\varepsilon}$. According to Nieh et al. [Nieh97 (p.37)], Čadek [Cadek88 (p.135, 173)] and Sherby & Burke [Sherby68 (p.347)] this value correlates with climb-controlled creep. Recently, it has been pointed out by Kassner & Pérez-Prado [Kassner00 (p.12, 30)] that the exponent n in many alloys and pure metals is about five over a relatively wide range of temperatures and strain-rates. In our case - tensile deformation at a constant crosshead speed - the climb of dislocations can also be considered as a deformation mechanism.

It is interesting to find how equation 2.15 describes the experimental data given above. The exponent n fitted with the help of equation 2.15 also supports the value of n about 5. At temperatures 250 °C and 300 °C where quality of the fit is rather high ($R^2 \geq 0.995$) the exponent n is 6.3 and 5.4, respectively. In general, the exponent n computed according to equation 2.15 monotonically decreases from n = 6.9 at 200 °C to n = 3.3 at 400 °C but correlation coefficient at temperatures 200 °C, 350 °C and 400 °C is low ($R^2 \leq 0.98$). Thus, the results at these temperatures should be considered with some caution.

5.1.4.6. Deformation energy

The energy necessary to fracture per unit volume (i.e. toughness U_t) may be calculated by using the following relation (see eq. 2.3 in section 2.1)

$$U_t = \frac{1}{V_0} \int_{l_0}^{l_f} F ds \qquad 5.4$$

where F is the loading force, s is deformation length of the specimen ($s \subset l_o, l_f$), l_o (l_f) is initial (fractured) length and V_0 is initial volume.

The toughness U_t refers to work that is necessary for failure of the specimen at given temperature and strain rate. A typical dependence of U_t on the temperature for $\dot{\varepsilon} = 1.3 \times 10^{-3} s^{-1}$ is shown in **Fig. 5.22**.

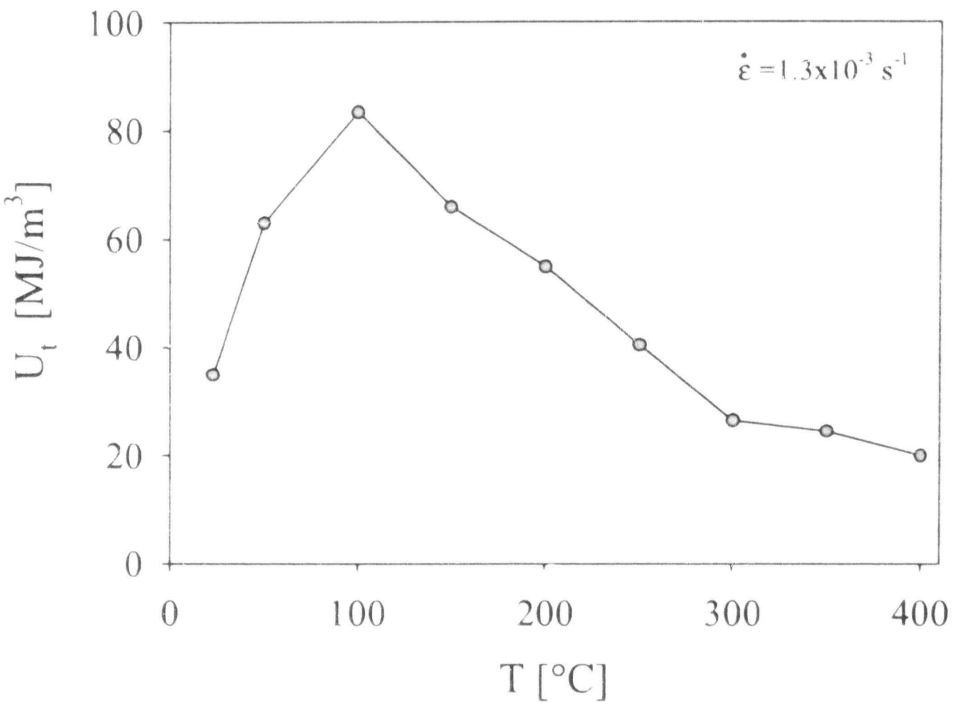

***Fig. 5.22**: Work necessary to fracture (i.e. the deformation energy) per unit volume in the temperature range rt-400 °C calculated from eq. 5.4; strain rate* $\dot{\varepsilon} = 1.3\text{x}10^{-3}\ \text{s}^{-1}$.

The dependence is not monotonous but shows maximum at 100 °C and then gradually decreases. The maximum corresponds with the highest toughness. The toughness increases between rt and 100 °C because the decrease in the yield stress and the maximum stress is "overwhelmed" by increasing ductility. However, at T > 100 °C toughness is gradually decreasing. The maximum in **Fig. 5.22** is accompanied by the change of the course of stress-strain curves as can be seen in **Fig. 5.23**. If fracture occurs abruptly in the strain hardening region, then toughness increases. But as the temperature increases, softening processes operate, fracture is postponed beyond σ_{max} (at and above 100 °C in **Fig. 5.23**) and toughness begins to decrease.

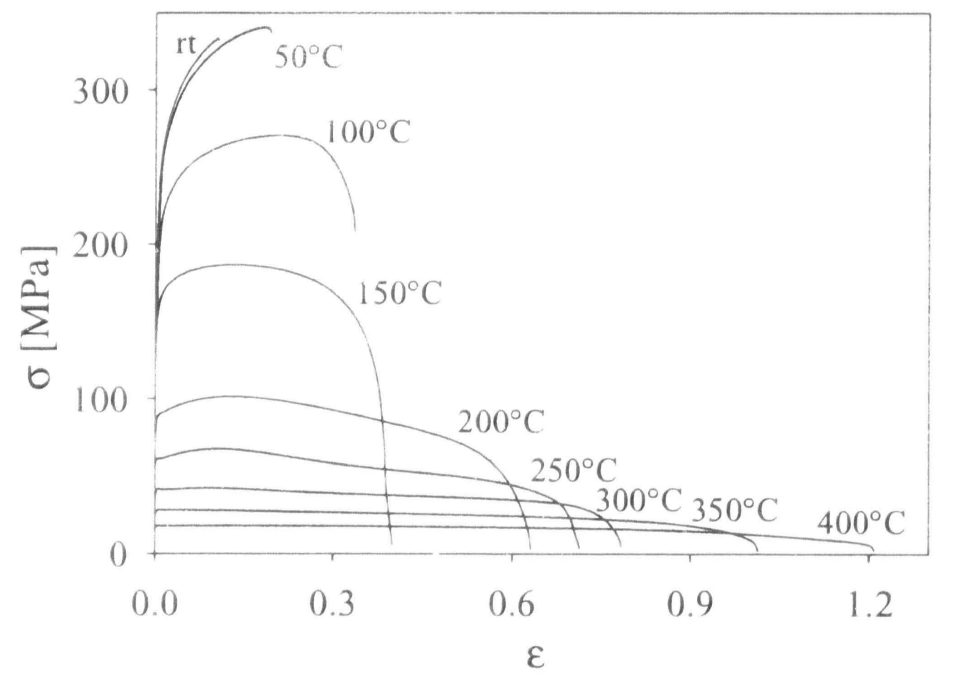

***Fig. 5.23**: True stress-true strain curves at* $\dot{\varepsilon} = 1.3\text{x}10^{-3}\text{s}^{-1}$.

It is therefore likely that maximum of the toughness is observed at temperatures at which the onset of softening occurs. Releasing of the stress concentrations due to

softening processes enable to delay the onset of cracking. However, near the peak toughness the softening may be localized into the evolution of necked region as indicated by **Fig. 5.17b** (section 5.1.4.4). Such softening may be accommodated by the progressive activity of non-basal dislocation glide. As early as Bridgman [Bridgman44] pointed out that the stress concentrations in the necking region are expected to be higher than in the uniaxially deformed specimen and, thus, enhanced dislocation activity in this site can be more prone. In other words, the stress concentrations give arise to the multi-axial stress fields, at which the CRSS for non-basal slip system may be easily reached and may result in the observed activity of softening processes. Ion et al. [Ion82] reported about concentration of deformation in Mg-0.8wt.%Al into the shear zones for specimens deformed in compression. Complex processes in the vicinity of the shear zones resulted in non-basal slip and twinning on various planes. Similar behaviour can be preferred in this alloy due to crystallographic anisotropy and strong texture. Activity of the slip in non-parallel planes can lead to the different dislocation reactions and enable their annihilation resulting in softening.

Similar maxima in $U_t(T)$ dependence were observed for all strain rates. The temperatures T_U at which these maxima were detected are shown as a function of the initial strain rates in **Fig. 5.24**. The higher the strain rate the higher the temperature

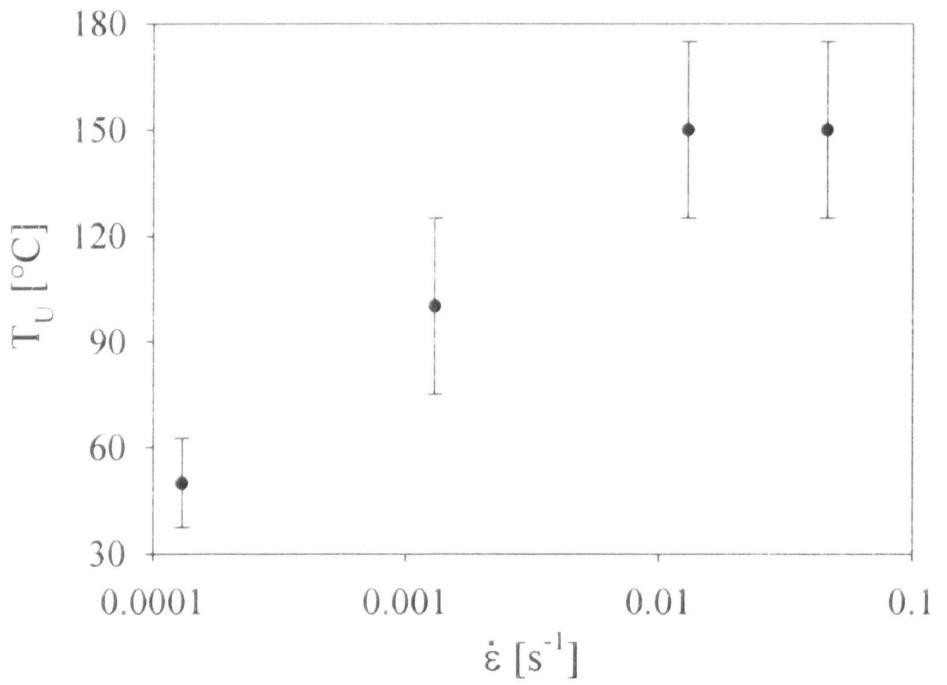

***Fig. 5.24**: Temperature T_U of maximum energy for different initial strain rates $\dot{\varepsilon}$.*

indicating the maximum in toughness; that is the onset of softening on the stress-strain curves. It is stressed, however, that softening may be (at least near the peak temperature) concentrated in the region of localized strain.

5.2. AA6082 aluminium alloy

5.2.1. Composition and properties

Wrought aluminium alloy matching with AA6082 was used in this study. Extruded bars with a twelve mm in diameter were produced. A scheme of direct extrusion process is shown in **Fig. 5.25**. The thermal treatment of as-extruded rods comprised annealing at 350 - 400 °C for 2 hours with subsequent cooling in the furnace (cooling rate <50 °C/h) [VUK06]. The specimens have been supplied by Research Institute for Metals, Czech Republic [VUK06].

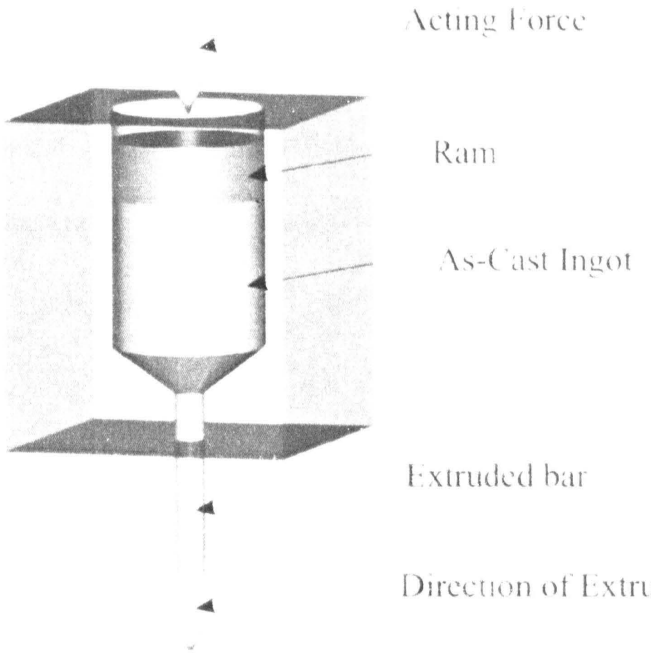

***Fig. 5.25**: Scheme of direct extrusion process.*

Composition of AA6082 alloy is summarised in **Tab. 5.5**. 6xxx series alloys represent material with medium strength and good formability [ASMAluminum94 (p.61)]. This alloy belongs to the group of commercial aluminium alloys, in which relative volume, chemical composition and morphology of structural constituents exert significant influence on its useful properties.

Element	Si	Fe	Cu	Mn	Mg	Cr	Zn	Sc	Zr
Typical AA6082	0.7-1.3	0.5	0.1	0.4-1.0	0.6-1.2	0.25	0.20	-	-
Alloy in this study	0.79	0.16	0.068	0.88	0.93	0.12	0.033	-	-

***Tab. 5.5**: Composition of AA6082 alloy and alloy used in this study [VUK06]; content in wt%.*

Silicon significantly improves casting characteristic whereas cooper decreases cast ability. On the other hand, copper substantially improves strength in both as-cast

and heat-treated conditions. Iron improves casting process but high concentration of iron is accompanied by decreased ductility. Manganese is normally considered an impurity in casting compositions but offers some benefits in wrought alloys such us preventing grain grow and slowing recovery. Magnesium is the basis for strength in heat treated Al-Si alloys since hardening phase Mg_2Si is formed. Chromium is usually added in low concentrations to suppress grain grow tendencies by formation of $CrAl_7$. No significant technical benefits are obtained by the addition of zinc to aluminium. Accompanied by the addition of cooper and/or magnesium, however, zinc results in attractive heat-treatable or naturally aging compositions [ASMAluminum94 (p.91)].

Considering all aluminium alloys, the strength is not as high as 2xxx and 7xxx series alloys [ASMAluminum94 (p.61)]. In automotive industry, the heat-treatable 6xxx alloys are preferred for outer panel applications whereas the highly formable 5xxx alloys are used mostly for inner panel applications [Miller00]. AA6082 is appreciated for very good corrosion resistance, very good weldability (lowered strength values in the zone of welding), good machinability, good cold formability in T4 temper and medium high fatigue strength [EAA01]. AA6082 alloy offers strength somewhat higher than common AA6061 [EAA01].

5.2.2. Microstructure

Fig 5.26 shows as-received microstructure of the AA6082 alloy in the plane parallel with extrusion direction. A weak contrast of grain boundaries is caused by slow cooling rate after annealing that results in overaging of the alloy [VUK06]. Elongated grains in **Fig.5.26** are a consequence of extrusion process.

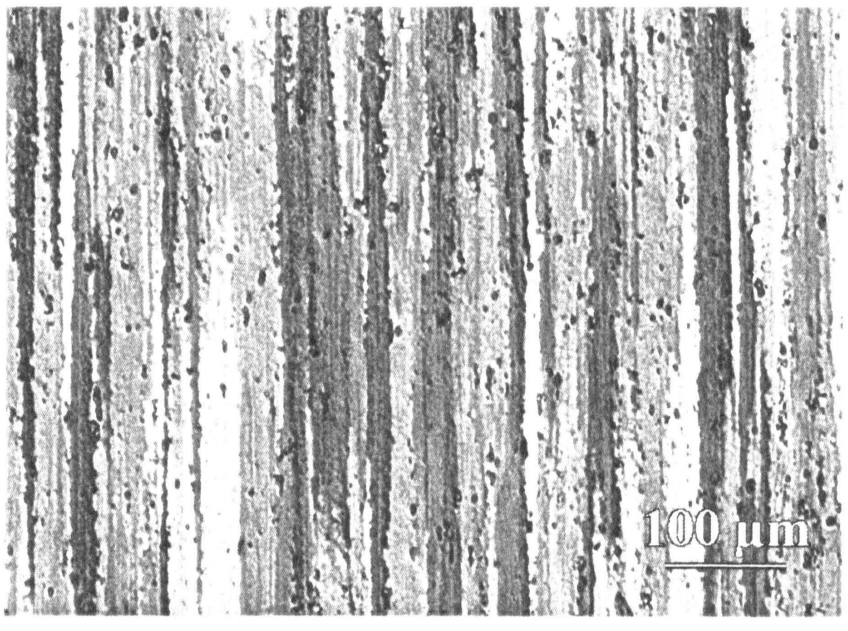

***Fig.5.26**: As-received microstructure of the AA6082 alloy. Extrusion direction is vertical. Light microscopy, etched [VUK06].*

Aluminium alloys AA6xxx contain a large volume fraction of various intermetallic particles (typically 1%) with sizes typically ranging between 1 and 10 μm. These coarse particles have a direct effect on formability. The exact composition of the alloy and the casting condition will directly influence the selection and volume fraction of intermetallics phases [Sha01]. The most typical are the plate-like β-Al_5FeSi particles and the rounded α-$Al_{12}(Fe,Mn)_3Si$ particles [Lassance07 (p.65)].

Alloys in the 6xxx series contain Si and Mg approximately in the proportions (see **Tab. 5.5**) required for formation of magnesium silicide (Mg_2Si), thus making them heat-treatable [ASMAluminum94 (p.18, 44)]. Alloys may be formed in the T4 temper (solution heat-treated but not precipitation heat-treated) and strengthened after forming by precipitation heat-treatment (T6 temper).

Distribution of the intermetallic phases is shown in **Fig.5.27**.

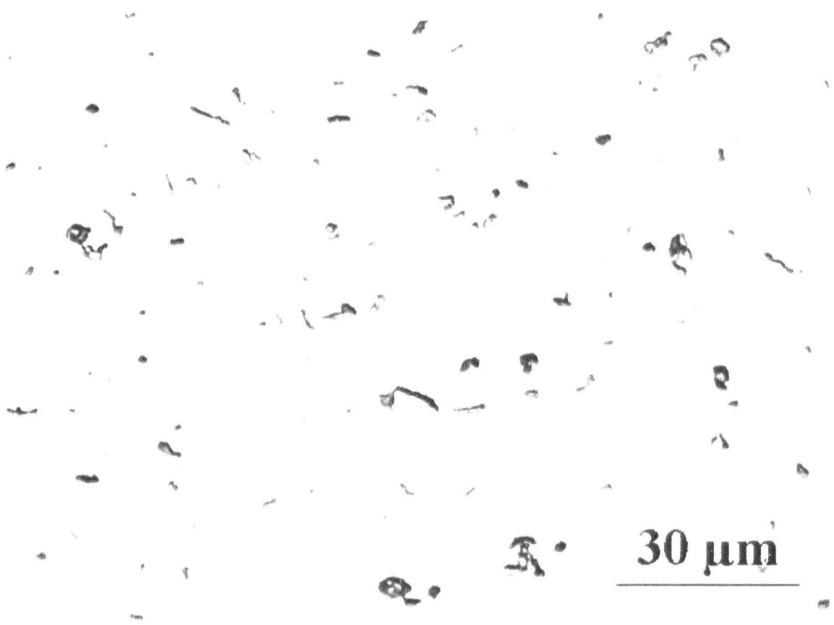

***Fig.5.27**: As-received microstructure of the AA6082 alloy showing distribution of intermetallic phases. Micrograph is taken in the plane perpendicular to the extrusion direction. Light microscopy [VUK06].*

While relatively a lot of data is available on microstructure and microstructure evolution in 6xxx series alloys, limited amount of data seems to be published on the deformation behaviour of AA6082 alloy. Therefore, following sections deal with deformation analysis.

5.2.3. Deformation behaviour- σ(ε) curves

Cylindrical specimens for tensile tests, 5 mm in diameter with a gauge length of 30 mm, were machined from annealed rods by [VUK06]. The true stress – true strain curves measured at different temperatures and at a strain rate of $\dot{\varepsilon} = 10^{-3}\ s^{-1}$ are shown

in **Fig. 5.28**. Up to 200 °C strong hardening is observed, and at and above 250 °C steady state flow stress prevail. The effect of strain rate on the true stress-true strain curves of AA6082 alloy at 400 °C is shown in **Fig. 5.29**. As expected, the higher the strain rate the higher the flow stress.

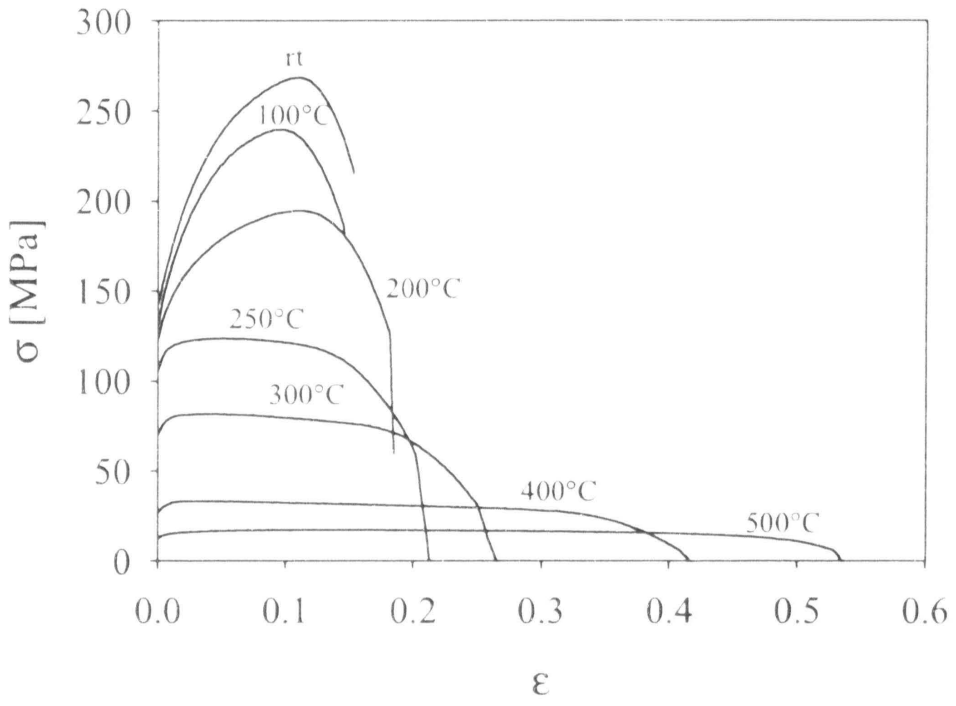

***Fig. 5.28**: True stress – true strain curves tested over a range of temperatures from rt to 500 °C and at strain rate* $\dot{\varepsilon} = 10^{-3}\ s^{-1}$.

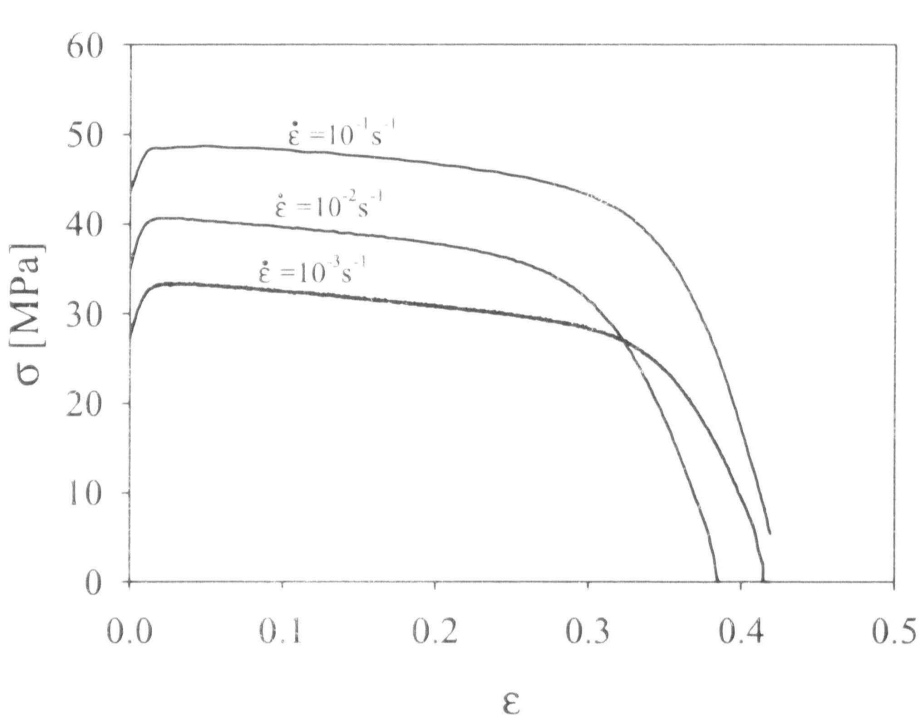

***Fig. 5.29**: Typical true stress – true strain curves at T = 400 °C and at different strain rates.*

The steady state flow stress observed at elevated temperatures indicates dynamic equilibrium between hardening and softening processes. Spigarelli et al. [Spigarelli03] analysed high-temperature plasticity of a heat-treated AA6082 aluminium alloy in torsion in a wide range of temperatures and strain rates. The alloy was solution treated at 530 °C for 2 h, and then aged for 24 h at the temperature selected for the torsion test. They suggest that, as in many others Al-based alloys, the high temperature deformation of the AA6082 with a stable dispersion of precipitates, is recovery-controlled.

The temperature dependences of the yield stress σ_{02} and the maximum stress σ_{max} for specimens deformed at $\dot{\varepsilon} = 10^{-3}\ s^{-1}$ are shown in **Fig. 5.30a**. Mechanical stability is observed up to ~200 °C. At higher temperatures both characteristic stresses

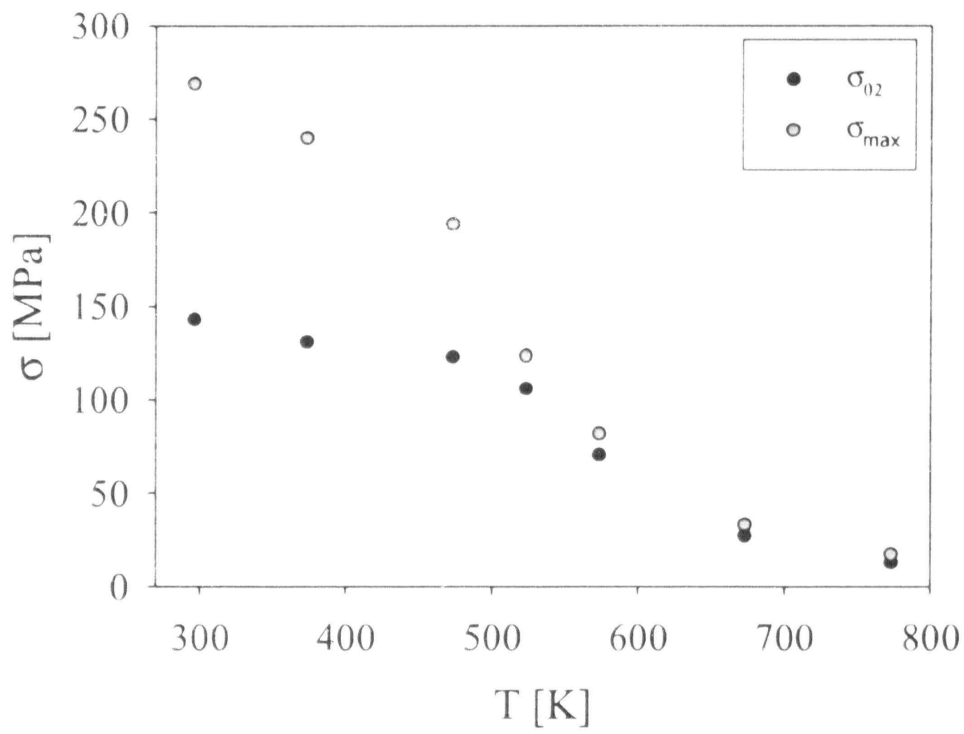

***Fig.5.30a**: Yield stress σ_{02} and maximum stress σ_{max} as a function of temperature T at $\dot{\varepsilon} = 10^{-3}\ s^{-1}$.*

sharply decrease with increasing temperature. Close values of the both characteristic stresses at and above 250 °C indicate dynamic equilibrium between hardening and softening processes and, as already mentioned, this may be observed on the $\sigma(\varepsilon)$ curves as a steady state flow stress. The effect of strain rate on σ_{02} and σ_{max} for specimens deformed at 300, 400 and 500 °C is shown in **Fig. 5.30b**. An increase in strain rate at

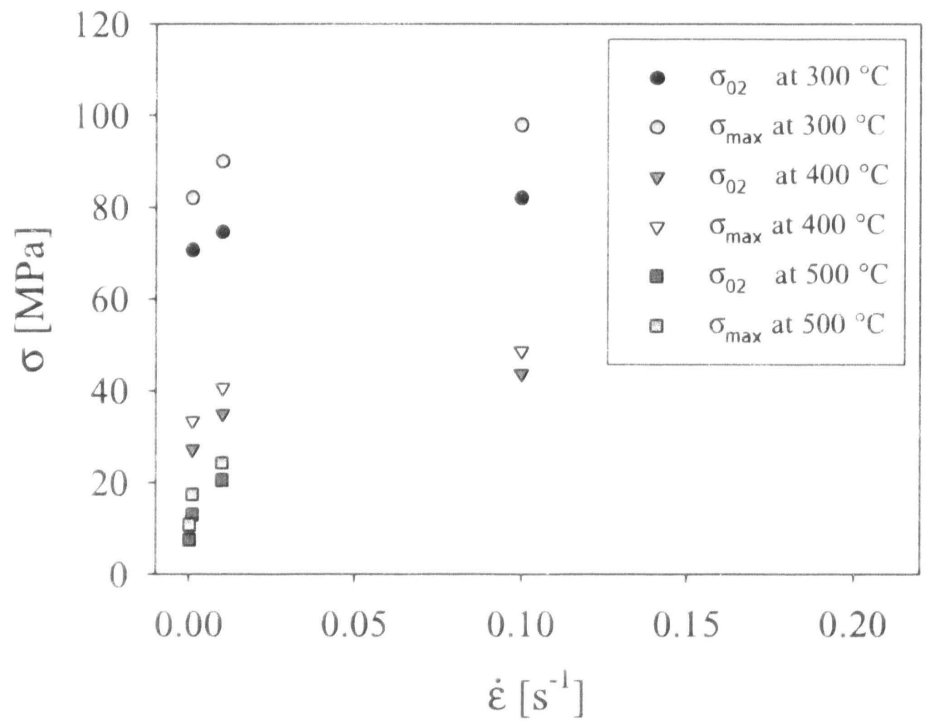

***Fig. 5.30b**: Yield stress σ_{02} and maximum stress σ_{max} as a function of strain rate $\dot{\varepsilon}$ at 300, 400 and 500 °C.*

selected temperature causes gradual increasing of the both stresses. A higher sensitivity of the both stresses to the strain rates is observed for lower strain rates.

5.2.4. Ductility and necking

Fig. 5.31 shows the elongation to failure A_0 for all temperatures and strain rates tested. Up to 200 °C failure occurs at ~20% and then increases with an increase of the temperature. Insensitivity of the A_0 to the test temperature up to 200 °C is in accordance with mechanical stability of the yield stress σ_{02}. The strain rate dependence of A_0 was not observed but for $\dot{\varepsilon} = 10^{-4}\ s^{-1}$. The highest elongation (A_0~100%) was obtained at T = 500 °C and at $\dot{\varepsilon} = 10^{-4}\ s^{-1}$. This may indicate additional deformation process acting at the lowest strain rate that contributes to postpone failure.

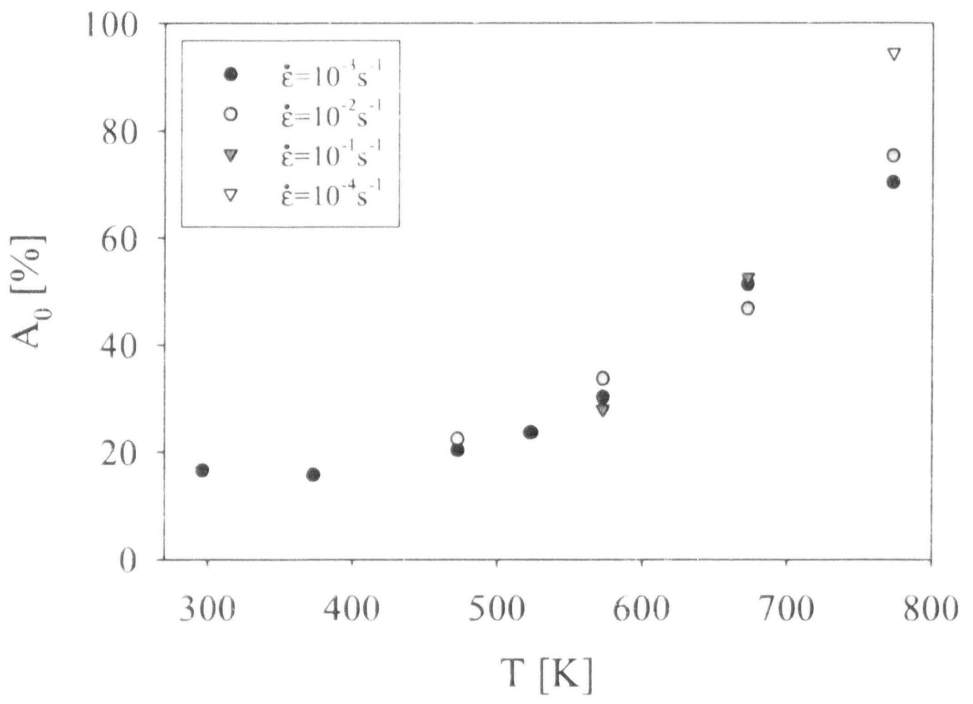

Fig. 5.31: Elongation to fracture A_0 versus temperature at different strain rates $\dot{\varepsilon}$ as depicted in figure.

The necking was measured in the same way as described in section 5.1.4.4. The necking was obvious at all temperatures, most markedly at T = 400 °C and $\dot{\varepsilon} = 10^{-2}\ s^{-1}$. It is worth to mention that up to 300 °C necking seems to be insensitive to the strain rate range tested (**Fig. 5.32**).

This alloy shows rather moderate ductility at elevated temperatures. Even at the highest temperatures (~500 °C) and the lowest strain rates (~$10^{-4}\ s^{-1}$) the ductility is less than 100%. One of the possible reasons may be unstable structure such as grain coarsening at high temperatures. Lee et al. [Lee02] studied the influence of scandium and zirconium on the microstructural stability and superplastic behaviour in Al-3%Mg

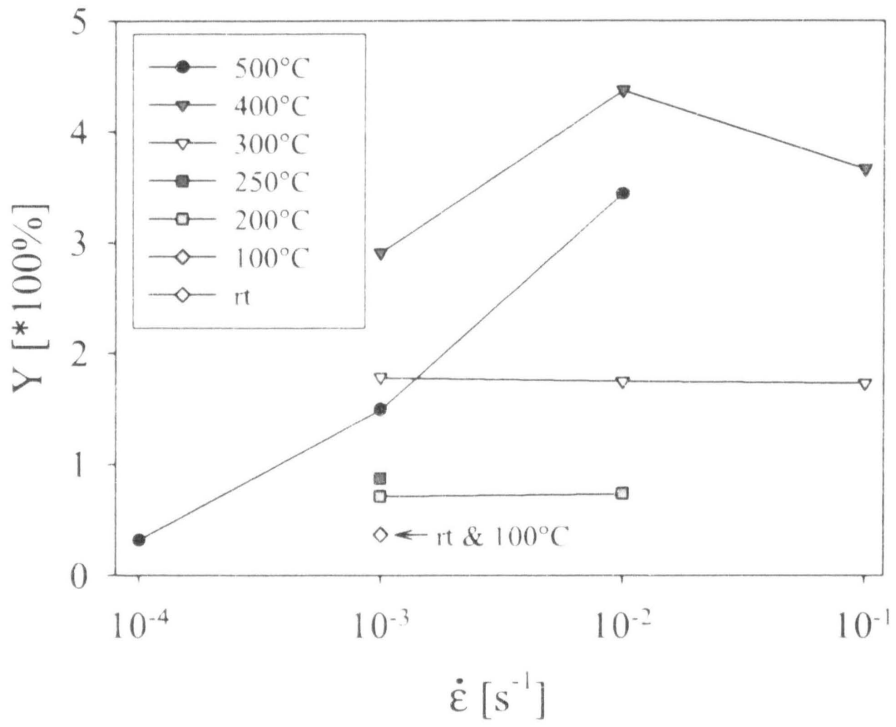

***Fig. 5.32**: Necking Y after fracture for different temperatures and initial strain rates $\dot{\varepsilon}$. Measurement of the necking is sketched in the inset of **Fig. 5.17b** (section 5.1.4.4). The lower the number on y-axis the lower contribution of the necking and vice versa.*

alloy. Right these two elements (Zr and Sc) have not been detected in this alloy (**Tab. 5.5**). Lee et al. pointed out that Sc and Zr addition play a critical role by providing precipitates, which impede grain growth at elevated temperatures and, thus, enable superplasticity. At the highest temperatures (~500°C) the both elements were needed to stabilize microstructure by formation of $Al_3(Zr_xSc_{1-x})$ precipitates [Lee02]. Cherry & Leo [Cherry05] studied the effect of Sc and Zr on the microstructure and precipitation strengthening in the AA6082 alloy subjected to the intensive deformation. While artificial aging in extruded AA6082 alloy with Sc and Zr addition led to the significant increase in hardness due to precipitates, artificial aging in the material after ECAP either exhibits a decrease in hardness with time (at higher aging temperatures) or remains almost constant (at lower aging temperatures). Cherry & Leo attributed such behaviour to the softening of the matrix (such as recovery or recrystallization) that could occur during annealing of the severely strained microstructure.

Regarding the composition of the alloy studied, low ductility at ambient temperatures may be due to the formation of intermetallic compounds (section 5.2.2). Lassance et al. [Lassance07 (p.65)] reported that the brittle, monoclinic β-Al_5FeSi phase, which is insoluble during solution heat treatment, is associated with poor workability. Moreover, damage during deformation initiates by decohesion or fracture of these inclusions. Uniaxial tensile tests performed on two aluminium alloys wherein the content in β versus α particles was systematically varying revealed that the ductility

increases with decreasing amount of β particles, increasing temperature and strain rates [Lassance07 (p.62)]. Thus, the resistance to fracture depends directly on the nature, shape, distribution and volume fraction of the second phase particles.

In situ tensile tests revealed that, at ambient temperature, the α particles and the β particles oriented with the long axis perpendicular to the main loading direction undergo interface decohesion, while the β particles oriented perpendicular to the loading direction break into several fragments. At high temperatures, only interface decohesion is observed [Lassance07 (p.62)].

The negative effect of the β-Al_5FeSi particles can be alleviated by a long homogenisation heat treatment at a sufficiently high temperature. During this process the β-Al_5FeSi phase transforms into the more rounded meta-stable cubic α-$Al_{12}(Fe,Mn)_3Si$ phase or into the equilibrium hexagonal α' phase [Kuijpers02, Lassance07 (p.65)]. On the other hand, Sha et al. [Sha01] pointed out that at higher growth velocities during directional solidification the formation of α-AlFeSi phase by the eutectic reaction dominates the phase selection. Therefore, it is likely that type of these phases depends mainly on the cooling rate and exact composition.

5.2.5. Stress as a function of temperature and strain rate

Constitutive analysis was performed in a similar way as demonstrated in section 5.1 for AZ31 magnesium alloy. The using of equation 2.15 (or its modifications 2.16-2.17) described in section 2.2 leads to the proportionality

$$\ln(\sigma) \sim \frac{1}{T}.$$

Fig. 5.33 shows proposed dependence. It can be seen that qualitative course corresponds with **Fig. 5.11** (section 5.1.4.1) for AZ31 magnesium alloy. For AA6082, however, the plateau is observed up to ~200 °C followed by decreasing at higher temperatures. At about 200 °C thermally activated phenomena start to influence the deformation process that begins to be very sensitive to the test temperature and imposed strain rate.

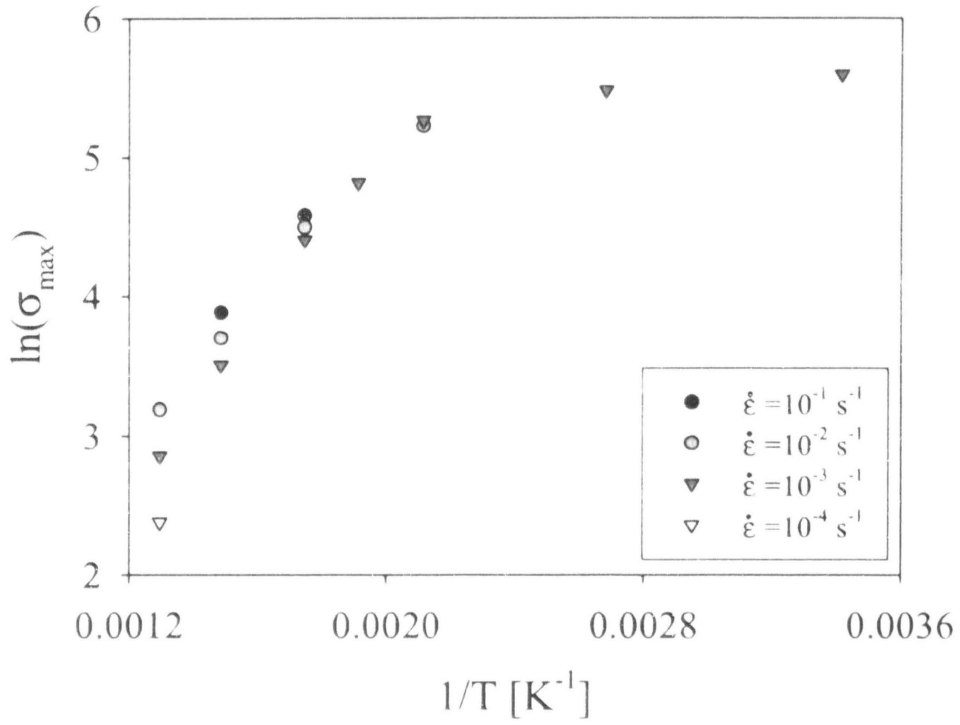

***Fig. 5.33**: Logarithm of σ_{max} as a function of T^{-1}. The inset shows initial strain rates used for deformation.*

The plots of the maximum stress, σ_{max}, against the logarithm of the strain rate are shown in **Fig. 5.34**. Quality of the fit expressed by R-parameter in **Fig. 5.34** shows that proposed dependence is in excellent agreement for the strain rates and the alloy tested. Since the same quality of the fit was observed for AZ31 magnesium alloy (**Fig. 5.12**), it is evident that the constitutive equation 2.7 introduces a useful description of

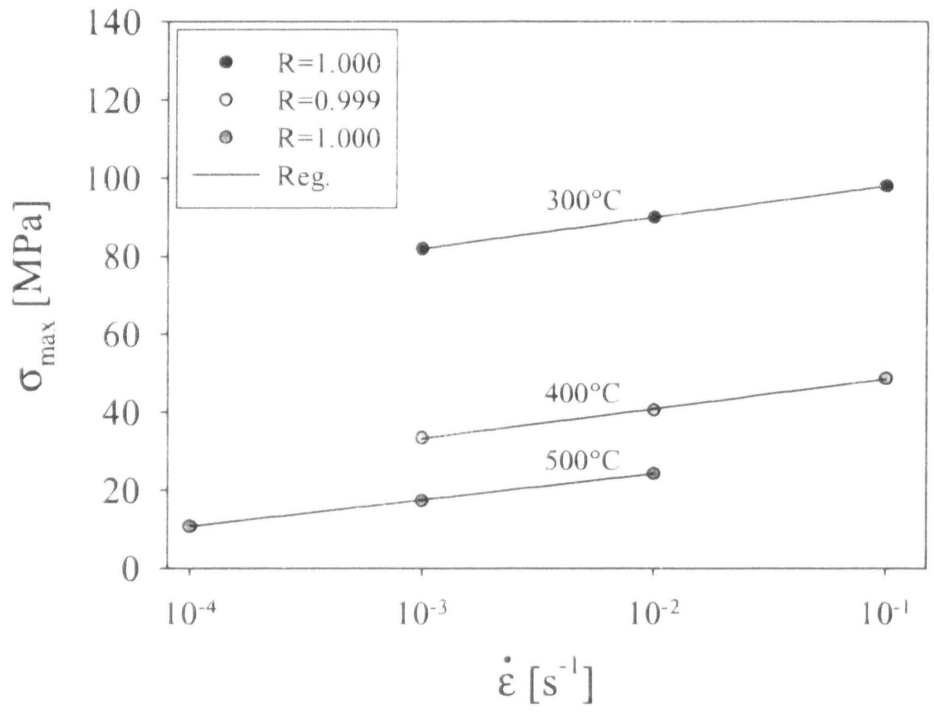

***Fig. 5.34**: Dependence of the maximum stress on the strain rate (in logarithmic scale) at high temperatures. Inset indicates quality of the fit.*

the deformation behaviour in both alloys. The slope χ of the regression curves in **Fig. 5.34** is shown in **Fig. 5.35**. The higher the temperature the lower the slope. According to the Arrhenius equation (eq. 2.20 in section 2.2.1), the slope χ may be expressed as a function of the activation volume V

$$\chi = \frac{R_m T}{V} \quad . \qquad 5.1$$

The observed decrease of the slope with temperature may be explained under assumption that the activation volume V increases with increasing temperature. But the increase of V with temperature is expected because annihilation of dislocations occurs. It means that the distance between obstacles increases and therefore the activation volume increases, too. It is worth to mention that decreasing dependence was also observed for AZ31 magnesium alloy (section 5.1.4.2). For AA6082, however, decreasing of the slope with temperature in **Fig. 5.35** is not so profound.

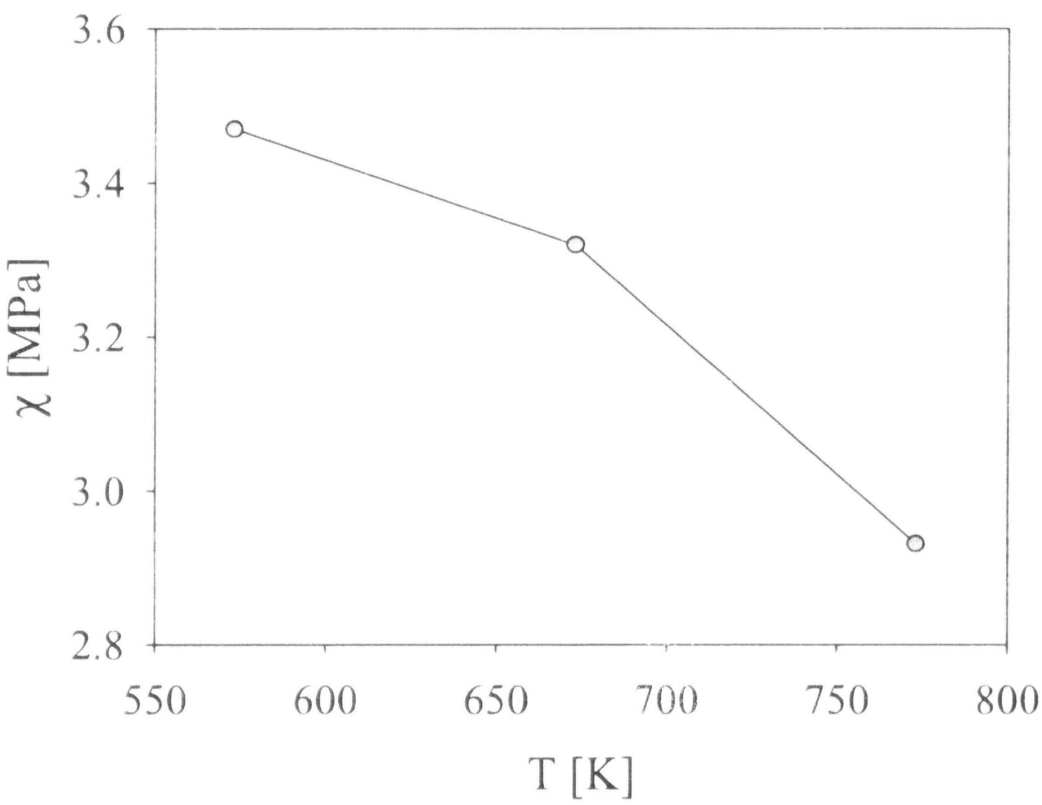

***Fig. 5.35**: Slope of the regression curves χ in **Fig. 5.34**.*

It is well known that deformation at elevated temperatures for most metals and alloys often obey a *power-law creep*, i.e. $\dot{\varepsilon} \propto \sigma^n$ with n frequently ~5, e.g. [Kassner00 (p.12, 30)]. As pointed out by e.g. Sherby & Burke [Sherby68 (p.360)], at higher stress levels the power law breaks down, and the dependence fulfils equation 2.7. Indeed, this study indicates that both AZ31 alloy and AA6082 alloy are described very well by equation 2.7 for the test temperatures and imposed strain rates.

6. Conclusions and perspectives

6.1. Conclusions

Two commercially available alloys have been studied in this work: AZ31 magnesium alloy and AA6082 aluminium alloy. The most important results are summarised as follows.

It was shown for rolled *AZ31 magnesium alloy*:

- Static recrystallization took place at temperatures above 150 °C. Twins play very important role during recrystallization and serve as nucleation sites and fast growing paths.
- AZ31 sheets prepared by rolling exhibit distinct texture. In this preferred orientation of the crystallites is the c-axis of many grains almost perpendicular to the surface and $\langle 11\bar{2}0 \rangle$ direction is parallel to the rolling direction. The texture is markedly weakened by static recrystallization but partial preferred orientation of the c-axis is still evident.
- AZ31 sheets show enhanced ductility even at room temperature (rt). The elongation to failure about 21% for as-received specimens and 26% for recrystallized specimens were observed.
- The yield strength σ_{02} for as-received alloy is about 220 MPa at rt and decreases with increasing temperature. Recrystallized alloy shows σ_{02} about 130 MPa at rt.
- Relation $\sigma_{max} \sim \ln \dot{\varepsilon}$ fits very well the deformation behaviour at elevated temperatures ($T \geq 200$ °C).
- The model of Lukac and Balik provides reasonable description of the micromechanisms of plastic deformation at rt.
- The temperature dependence of the toughness at all strain rates show maxima. These maxima are strain rate sensitive. The higher the strain rate the higher the temperature at which toughness maximum is observed.

- Superplasticity was identified at the lowest strain rate $\dot{\varepsilon} = 1.3x10^{-4}\ s^{-1}$ and the highest temperatures (T > 300 °C). The elongation to failure reached 420% at T = 400 °C and m = 0.7.
- The shape of the stress-strain curves is very sensitive to the testing temperature and initial strain rate.

The deformation behaviour of extruded *AA6082 aluminium alloy* was investigated at different temperatures and at different strain rates. It can be concluded:

- A significant hardening is observed bellow 200 °C. Both characteristic stresses (σ_{02}, σ_{max}) show moderate sensitivity to the strain rate.
- The elongation to fracture A_0 seems to be insensitive to the strain rate in the range 10^{-3}-$10^{-1}\ s^{-1}$ but for $\dot{\varepsilon} = 10^{-4}\ s^{-1}$.
- The elongation to fracture A_0 is roughly constant (~20%) up to 200 °C and then gradually increases. The highest elongation (A_0 ~100%) was obtained at T = 500 °C and at $\dot{\varepsilon} = 10^{-4}\ s^{-1}$.
- Necking was developed at all temperatures, most markedly at T = 400 °C and $\dot{\varepsilon} = 10^{-2}\ s^{-1}$. Up to 300 °C the necking seems to be insensitive to the strain rate.
- Relation $\sigma_{max} \sim \ln\dot{\varepsilon}$ fits very well the deformation behaviour at elevated temperatures (T ≥ 200 °C).

6.2. Perspectives

Magnesium and aluminium alloys are often considered to be a promising material due to a superior strength/density ratio. For example, in the transport industry they can replace Fe alloys and, thus, reduce fuel consumption by the weight reduction. In general, light alloys are very attractive structural materials for applications where environmental protection plays essential role. Therefore, it is of interest to investigate microstructure and its changes during plastic deformation (PD) because it helps to understand the nature of solute effect and processes taking place during PD.

Currently, a lot of research effort is dedicated to the grain refinement that is followed by microstructural analysis and PD characterisation of the grain-refined material. Easily scalable "Severe plastic deformation" methods such as ARB and ECAP offer powerful tools to obtain very fine structures in relatively sufficient amount. The main motivation for grain refinement follows from improved properties such us increased strength and enhanced ductility.

It is necessary to further improve a ductility of magnesium alloys by introducing of new compositions and thermomechanical treatments at sustainable production costs. It is evident that from "ductility" point of view hcp structures remains always inferior to fcc metals. However, up-to-date results indicate that there are some ways to overcome limited ductility of Mg alloy. The knowledge of dislocation mechanisms together with the influence of alloying on non-basal slip activity would be appreciated in this effort.

Creep resistance is a major requirement for high temperature applications of magnesium alloys (up to 300 °C). The development is aimed at replacing RE additions to magnesium with other elements. Most promising elements for new creep resistant alloys seem to be strontium and calcium. As a result various alloys have been introduced and thoroughly studied, e.g. AX51 (Mg-Al-Ca) and AJ51 (Mg-Al-Sr).

An improvement of the corrosion resistance without enormous increase of the production cost is one of the main targets of magnesium research nowadays.

Aluminium is versatile metal that is able to form glasses, crystalline solids and even quasicrystals [Inoue00]. Recently, "bulk" single Al-based icosahedral quasicrystals were reported, e.g. [Yokoyama00, Graber00]. It is anticipated that formation of the quaicrystals may result in new applications. As for all materials, systematic improving of the properties (yield point, superplasticity) is desirable.

Due to the development of new alloys it is important to study the relation between microstructure, composition and properties. The micromechanisms taking place during plastic deformation should be primarily investigated on *binary* and *ternary alloys* varying in composition and thermomechanical treatment since a better understanding of the influence of alloying elements can be achieved. Commercially available alloys contain rarely less than three alloying elements; this make a detailed analysis of micromechanisms on "atomic level" infeasible. In this regard, study of the solid solution hardening in single crystals may inject important insight into the problem.

7. References

[Aghion06] E. Aghion: The Viability of Mg Alloy with Nano/Submicron Structure as a New Material for Practical Applications, ed. K.U. Kainer, 7th International Conference on Magnesium and their Applications, organized by DGM, 6-9 November, Dresden, 2006, oral presentation.

[Agnew01] S. R. Agnew, M. H. Yoo, C. N. Tome, Acta Mater., *49*, 2001, p. 4277.

[Agnew03] S.R. Agnew, C.N. Tom, D.W. Brown, T.M. Holden, S.C. Vogel: Scripta Mater., *48*, 2003, p. 1003.

[Akhtar69] A. Akhtar, E. Teghtsoonian: Acta. Metall., *17*, 1969, p. 1351.

[Akhtar69a] A. Akhtar, E. Teghtsoonian: Acta. Metall., *17*, 1969, p. 1339.

[Akhtar71] A. Akhtar, E. Teghtsoonian: Phil. Mag., *25*, 1972, p. 897.

[Appleby70] E.J. Appleby: J. Appl. Phys., *41*, 1970, p. 4902.

[ASMAluminum94] ASM Specialty Handbook: Aluminum and Aluminum Alloys, ed.: J.R. Davis, 3rd printing, ASM International, Materials Park, OH, 1994.

[Aust52] K.T. Aust, F.M. Krill, F.R. Morral: Trans AIME, *194*, 1952, p. 865.

[Avedesian99] M.M. Avedesian, H. Baker (Eds): ASM Specialty Handbook Magnesium and Magnesium Alloys, ASM International, Materials Park, OH, 1999.

[Avery65] D. H. Avery, W A. Backofen: Trans ASM, *58*, 1965, p. 551.

[Backofen64] W.A. Backofen, I. R. Turner and D. H. Avery: Trans. ASM, *57*, 1964, p. 980; however, probably inspirited by Russian literature.

[Backofen68] W.A. Backofen, F.J.Azzarto, G.S. Murty, S.W. Zehr: Superplasticity, in: Ductility, seminar of the ASM, ASM Ohio, 1968, p. 279.

[Barnett04] M.R. Barnett, M.D. Nave, C.J. Bettles: Mater. Sci. Eng. A, *386*, 2004, p. 205.

[Barnett04a] M.R. Barnett, Z. Keshavarz, A.G. Beer, D. Atwell: Acta Mater., *52*, 2004, p. 5093.

[Birchon65] D. Birchon: Dictionary of Metallurgy, George Newnes Limited, London, 1965.

[Bohlen04] J. Bohlen, F. Chmelík, P. Dobroň, F. Kaiser, D. Letzig, P. Lukáč, K.U. Kainer: J. Alloys and Comp., *378*, 2004, p. 207.

[Bridgman44] P.W. Bridgman: Trans ASM, *32*, 1944, p. 553.

[Brungs06]: D. Brungs, A. Mertz: Die Casting, in: Magnesium Technology, eds: H.E. Friedrich, B.L. Mordike, Springer, Berlin, 2006, p. 234.

[Burton77] B. Burton: Diffusional Creep of Polycrystalline Materials, Trans Tech Publications, Aedermannsdorf, Switzerland, 1977.

[Cadek88] J. Čadek: Creep in Metallic Materials, Elsevier, Amsterdam, 1988.

[Cannon64] P. Cannon, E.T. Conlin: Science, *145*, 1964, p. 487.

[Cerry05] E. Cerry, P. Leo: Mater. Sci. Eng. A, *410-411*, 2005, p. 226.

[Coble63] R.L. Coble: J. Appl. Phys., *34*, 1963, p. 1679.

[Conrad61] H. Conrad in: Mechanical Behavior of Materials at Elevated Temperatures, ed. J.E. Dorn, McGraw-Hill, New York, 1961, p. 149.

[Cottrell48] A. H. Cottrell: Bristol Conference on the Strength of Solids, Physical Society, London, England, 1948, p. 30, Adopted from [Mott56].

[Crocker62] A. G. Crocker: Phil Mag, *7*, 1962, p. 1901.

[Crocker94] A. Crocker in: Twinning in Advanced Materials, ed: M.H. Yoo and M. Wuttig, Proceedings of a symposium, TMS, Pittsburg, 1993, p. 5.

[Dieter76] G.E. Dieter: Mechanical Metallurgy, 2nd ed., McGraw-Hill, New York, 1976.

[Dimitrov78] O. Dimitrov, R. Fromageau, C. Dimitrov: Effect of Trace Impurities on Recrystallization Phenomena, 2nd ed., in: Recrystallization of Metallic Materials, ed. F. Haessner, Dr. Riederer Verlag GmbH, Stuttgart, 1978.

[Doherty97] R.D. Doherty, D.A. Hughes, F.J. Humphreys, J.J. Jonas, D. Juul Jensen, M.E. Kassner, W.E. King, T.R. McNelley, H.J. McQeen, A.D. Rollet: Mater. Sci. Eng. A, *238*, 1997, p. 219.

[EAA01] http://aluminium.matter.org.uk/aluselect/01_applications.asp?alloyid=25

[Edax] http://www.edax.com/technology/EBSD/OIM/index.html

[Fleischer64] R. Fleischer: Strengthening of Metals, Reinhold Publishing Corp., New York, 1964, p. 93.

[Frank50] F.C Frank, W.T Read: Phys. Rev., *79*, 1950, p. 722.

[Frost82] H. J. Frost, M. F. Ashby: Deformation-Mechanism Maps, Pergamon Press, Oxford, 1982, adopted from H. Watanabe et al.: Acta Mater., *47*, 1999, p. 3753.

[Furui05] M. Furui, Ch. Xu, T. Aida, M. Inoue, H. Anada, T.G. Langdon: Mater. Sci. Eng. A, *410–411*, 2005, p. 439.

[Galiyev04] A. Galiyev, R. Kaibyshev: Scripta Mater., *51*, 2004, p. 89.

[Garofalo63] F. Garofalo: Trans. AIME, *227*, 1963, p. 351.

[Gerold79] V. Gerold: in: Dislocations in Solids, *vol.4*, ed. F.R.N. Nabarro, North-Holland, Amsterdam, 1979.

[GKSS02] GKSS-Research Centre, Institute for Materials Research, Max-Planck-Str. 1, D-21502 Geesthacht, Germany.

[Graber00] M. Gräber, R.U. Barz, P. Dreier, P. Gille: Mater. Sci. Eng. A, *294–296*, 2000, p.143.

[Guyot91] P. Guyot, G. M. Raynaud: Acta Metall. Mater., *39*, 1991, p. 317.

[Hall51] E.O. Hall: Proc. Phys. Soc. London, *B64*, 1951, p. 747.

[Hall54] E.O.Hall: Twinning and Diffusionless Transformations in Metals, London Butterworths, 1954.

[Hauser55] F.E. Hauser, C.D. Starr, L. Tietz, J.E. Dorn: Trans. ASM, *47*, 1995, p. 102.

[Herring50] C. Herring: J. Appl. Phys., *21*, 1950, p. 437.

[Hertzberg83] R.W. Hertzberg: Deformation and Fracture Mechanics of Engineering Materials, 2nd ed., John Wiley and Sons, New York, 1983.

[Hill57] R.E. Reed-Hill, W.D. Robertson: Acta Metall., *5*, 1957, p. 717.

[Hill60] R.E. Reed-Hill: Trans. AIME, *218*, 1960, p. 554.

[Hill73] R.E. Reed-Hill: Physical Metallurgy Principles, 2nd ed., Litton Educational Publishing, New York, 1973.

[Hollomon45] J.H. Hollomon: Trans. AIME, *162*, 1945, p. 268; adopted from [Hertzberg83 (p. 18)].

[Horita02] Z. Horita, K. Matsubara, K. Makii, T.G. Langdon: Scripta Mater., *47*, 2002, p. 255.

[Humphreys04] F.J Humphreys, M. Hatherly: Recrystallization and Related Annealing Phenomena, 2nd ed., Elsevier Science, Oxford, 2004.

[Humphreys77] F.J. Humphreys: Acta Metall., *25*, 1977, p. 1323.

[Humphreys95] F.J Humphreys, M. Hatherly: Recrystallization and Related Annealing Phenomena, Elsevier Science, Amsterdam, 1995.

[Humphreys99] F.J. Humhreys, P.B. Prangnell, R. Priestner: in The Fourth International Conference on Recrystallization and Related Phenomena, ed. T. Sakai, H.G Suzuki, JIM, 1999, p. 69.

[Hutchinson77] J.W. Hutchinson, K.W. Neale: Acta Metall. *25*, 1977, p. 839.

[Chen03] M. Chen, E. Ma, K.J. Hemker, H. Sheng, Y. Wang, X. Cheng: Science, *300*, 2003, p. 1275.

[Christian95] J.W. Christian, S. Mahajan: Progress in Materials Science, *39*, 1995, p. 1.

[Inoue00] A. Inoue, H.M. Kimura, T. Zhang: Mater. Sci. Eng., *294-296*, 2000, p. 727.

[Ion82] S.E. Ion, F.J. Humphreys, S.H. White, Acta Metall., *30*, 1982, p. 1909.

[Jager04] A. Jäger, P. Lukáč, V. Gärtnerová, J. Bohlen, K. U. Kainer, J. Alloys Comp. *378*, 2004, p. 184.

[Jager04a] A. Jäger, P. Lukáč, V. Gärtnerová, Kovove Mater., *42*, 2004, p. 165.

[Jager06] A. Jäger, P. Lukáč, V. Gärtnerová, J. Haloda, M. Dopita: Mater. Sci. Eng. A, *432*, 2006, p. 20.

[Kaibyshev02] O.A. Kaibyshev: Mater. Sci. Eng. A, *324*, 2002, p. 96.

[Kaiser03] F. Kaiser, J. Bohlen, D. Letzig, K. Kainer, A. Styczynsky, C. Hartig: Advanced Engineering Materials, *5*, 2003, p. 891.

[Kammer00] K. Kammer: Magnesium Taschenbuch, Aluminium-Zentrale Düsseldorf, 2000.

[Karim69] A. Karim: in: Ultrafine Grain Metals; ed.: J.J. Burke, V. Weiss; Proceedings of the 16th Sagamore Army Materials Research Conference, Syracuse University press, New York, 1969, p. 298.

[Kassner00] M.E. Kassner, M.T. Pérez-Prado: Five-power-law creep in single phase metals and alloys, Progress in Materials Science, *45*, 2000, p. 1.

[Kaufman00] J.G. Kaufman: Introduction to Aluminum Alloys and Tempers, ASM International, Materials Park, OH, 2000.

[Kelly00] A. Kelly, G.W. Groves, P. Kidd: Crystallography and Crystal Defects, 2nd ed., John Wiley and Sons, Chichester, 2000.

[Kettunen03] P.O. Kettunen, V.T. Kuokkala: Plastic Deformation and Strain Hardening, Trans Tech Publications, Zurich, 2003.

[Klassen64] M.V. Klassen-Neklyudova: *Mechanical Twinning of Crystals*, Translation from Russian by J.E.S. Bradley, Consultants Bureau, New York, 1964.

[Kocks87] U.F. Kocks in: Unified Constitutive equations for Creep and Plasticity, ed. A.K. Miller, Elsevier Science, London, 1987, p. 1.

[Koike03] J. Koike, T. Kobayashi, T. Mukai, H. Watanabe, M. Suzuki, K. Maruyama, K. Higashi: Acta Mater., *51*, 2003, p. 2055.

[Kuijpers02] N.C.W. Kuijpers, J. Tirel, D.N. Hanlon, S. van der Zwaag: Mater. Characterisation, *48*, 2002, p. 379.

[Labusch70] R. Labusch: Phys. Stat. Sol., *41*, 1970, p. 659.

[Langdon94] T.G. Langdon: Mechanisms of Superplastic Flow, in: Superplasticity: 60 Years after Pearson, ed.: N. Ridley, The Institute of Materials, London, England, 1995, p. 9.

[Lapovok05] R. Lapovok, P.F. Thomson, R. Cottam, Y. Estrin: Mater. Sci. Eng. A, *410-411*, 2005, p. 390.

[Lassance07] D. Lassance, D. Fabregue, F. Delannay, T. Pardoen: Progress in Materials Science, *52*, 2007, p. 62.

[Lee02] S. Lee, A. Utsunomiya, H. Akamatsu, K. Neishi, M. Furukawa, Z. Horita, T.G. Langdon, Acta Mater., *50*, 2002, p. 553.

[Li63] J.C.M. Li: Trans. AIME, *227*, 1963, p. 239.

[Lin05] H.K. Lin, J.C. Huanga, T.G. Langdon: Mater. Sci. Eng. A, *402*, 2005, p. 250.

[Lucke73] K. Lücke, H. Mecking: Dynamic recovery, in: The Inhomogeneity of Plastic Deformation, ed. R. E. Reed-Hill, ASM, 1973, p. 223.

[Ludwik09] P. Ludwik: Elemente der technologischen Mechanik, Verlag Julius Springer, Berlin, 1909, adopted from [Nadai50].

[Lukac81] P. Lukáč: Czech. J. Phys., *B31*, 1981, p. 135.

[Lukac94] P. Lukáč, J. Balík: Key Eng. Mater., *97–98*, 1994, p. 307.

[Mabuchi99] M. Mabuchi, K. Ameyama, H. Iwasaki, K. Higashi: Acta Mater. , *47*, 1999, p. 2047.

[Mahajan02] S. Mahajan: Deformation Twinning, in: Encyclopedia of Materials: Science and Technology, Elsevier Science, 2002, p. 1.

[Matsubara03] K. Matsubara, Y. Miyahara, Z. Horita, T.G. Langdon: Acta Mater., *51*, 2003, p. 3073.

[McFadden99] S.X. McFadden R.S. Mishra, R.Z. Valiev, A.P. Zhilyaev, A.K. Mukherjee: Nature, *398*, 1999, p. 684.

[McQueen02] H.J. McQueen, N.D. Ryan: Mater. Sci. Eng. A, *322*, 2002, p. 43.

[Miller00] W.S. Miller, L. Zhuang, J. Bottema, A.J. Wittebrood, P. De Smet, A. Haszler, A. Vieregge: Mater. Sci. Eng. A, *280*, 2000, p. 37.

[Mises28] R. von Mises: Z. Ang. Math. Mech., *8*, 1928, p. 161.

[Mitchell02] T.E. Mitchell, J.P. Hirth, A. Misra: Acta Mater, *50*, 2002, p. 1087.

[Miyahara06] Y. Miyahara, Z. Horita, T. G. Langdon: Mater. Sci. Eng. A, *420*, 2006, p. 240.

[Montheillet02] F. Montheillet, J. Le Coze: Phys.Stat. Sol. (a), *189*, 2002, p. 51.

[Mordike06] B.L. Mordike, P.Lukáč: Physical Metallurgy, in: Magnesium Technology, eds: H.E. Friedrich, B.L. Mordike, Springer, Berlin, 2006, p.63.

[Morozumi76] S. Morozumi, M. Kikuchi, H. Yoshinaga: Trans. JIM, *17*, 1976, p. 158.

[Mott56] N.F.Mott: Atomic Structure and the Strength of Metals, Pergamon Press, London, 1956.

[Mukai95] T. Mukai, K. Ishikawa, K. Higashi: Mater. Sci. Eng. A, *204*, 1995, p. 12.

[Mukai98] T. Mukai, M. Kawazoe, K. Higashi: NanoStructured Materials, *10*, 1998, p. 755.

[Mukherjee02] A.K. Mukherjee: Mater. Sci. and Eng. A, *322*, 2002, p. 1.

[Mukherjee69] A.K. Mukherjee, J.E. Bird, J.E. Dorn: Trans. ASM, *62*, 1969, p. 155.

[Mwembela97] A. Mwembela, E.B. Konopleva, H.J. McQueen: Scripta Mater., *37*, 1997, p. 1789.

[Myshlyaev02] M.M. Myshlyaev, H.J. McQueen, A. Mwembela, E. Konopleva: Mater. Sci. Eng. A, *337*, 2002, p. 121.

[Nadai50] A. Nadai: Theory of Flow and Fracture of Solids, 2nd ed., McGraw-Hill, New York, 1950.

[Nave04] M.D. Nave, R. Barnett: Scripta Mater., *51*, 2004, p. 881.

[Nieh05] T.G. Nieh: Plasticity and Strength of Nanocrystalline Ni and Ni-W alloys, Seminar held in January 18th , 2005, Tsukuba, Japan.

[Nieh97] T.G. Nieh, J.Wadsworth, O.D. Sherby: Superplasticity in Metals and Ceramics, Cambridge University Press, Cambridge, 1997.

[Nowick51] A.S. Nowick: J. Appl. Phys., *42*, 1951, p. 118.

[Obara73] T. Obara, H. Yoshinaga, S. Morozumi: Acta Metall., *21*, 1972, p. 845.

[Ono03] N. Ono, R. Nowak, S. Miura: Mater. Letters, *58*, 2003, p. 39.

[Padmanabhan80] K.A. Padmanabhan, G.J. Davies: Superplasticity, Springer, Berlin, 1980.

[Petch53] N.J. Petch: J. Iron Steel Inst.: *174*, 1953, p. 25.

[Poirier85] J.P. Poirier: Creep of Crystals, Cambridge University Press, Cambridge, 1985.

[Polmear92] I.J. Polmear: Light Alloys, in: Magnesium Alloys and Their Applications, eds.: B.L. Mordike, F. Heheman, DGM, Oberursel, 1992, p. 216.

[Polmear94] I.J. Polmear: Mater. Sci. Tech., *10*, 1994, p. 1.

[Polmear96] I.J.Polmear: Mater. Trans., JIM, *37*, 1996, p. 12.

[Randle04] V. Randle: Acta Mater., *52*, 2004, p. 4067.

[Serra91] A. Serra: Phil Mag A, *63*, 1991, p. 1001.

[Serra96] A. Serra: Phil Mag A, *73*, 1996, p. 333.

[Sha01] G. Sha, K. O'Reilly, B. Cantor, J. Worth, R. Hamerton: Mater. Sci. Eng. A, *304–306*, 2001, p. 612.

[Sharp65] J.V. Sharp, A. Mitchell, J.W. Christian: Acta Metall., *13*, 1965, p. 965.

[Shechtman84] D. Shechtman, I. Blech, D. Gratias, J.W. Cahn: Phys. Rev. Lett., *53*, 1984, p. 1951.

[Sherby68] O.D. Sherby, P.M. Burke: Progress in Materials Science, *13*, 1968, p. 323.

[Sherby89] O.D. Sherby, J. Wadsworth: Superplasticity-Recent Advantages and Future Directions, Progress in Material Science, *33*, 1989, p. 169.

[Shi94] L. Shi, D. O. Northwood: Acta Metall. Mater., *42*, 1994, p. 871.

[Shunk69] F.A. Shunk: Constitution of Binary Alloys, McGraw-Hill, New York, 1969.

[Schwartz00] A.J. Schwartz, M. Kumar, B.L. Adams (Eds.): Electron Backscatter Diffraction in Materials Science, Kluwer Academic/Plenum Publishers, New York, 2000.

[Spigarelli03] S. Spigarelli, E. Evangelista, H.J. McQueen: Scripta Mater., *49*, 2003, p. 179.

[Stohr72] J.F. Stohr, J.P. Poirier: Phil. Mag., *25*, 1972, p. 1313.

[Styczynski04] A. Styczynski, Ch. Hartig, J. Bohlen, D. Letzig: Scripta Mater., *50*, 2004, p. 943.

[Swygenhoven02] H. von Swygenhoven: Science, *296*, 2002, p. 66.

[Tegart68] W.J. McG. Tegart in: Ductility, Seminar of the ASM, October 14 and 15 1967, ASM, Metals Park, Ohio, 1968, p. 133.

[Titorov92] D.B. Titorov: The Physics of Metals and Metallography, *74*, 1992, p. 58.

[Uematsu06] Y. Uematsu, K. Tokaji, M. Kamakura, K. Uchida, H. Shibata, N. Bekku: Mater. Sci. Eng. A, *434*, 2006, p. 131.

[VUK06] Research Institute for Metals s.r.o., Panenské Břežany 50, CZ - 250 70 Odolena Voda, Czech Republic.

[Wang06] Y.N. Wang, C.I. Chang, C.J. Lee, H.K. Lin, J.C. Huang: Scripta Mater., *55*, 2006, p. 637.

[Watanabe01] H. Watanabe, T. Mukai, M. Mabuchi, K. Higashi: Acta Mater., *49*, 2001, p. 2027.

[Watanabe02] H. Watanabe, T. Mukai, K. Ishikawa, K. Higashi: Scripta Mater., *46*, 2002, p. 851.

[webelements] http://www.webelements.com

[Wiedersich64] H. Wiedersich: J. Metals, *16*, 1964, p. 425.

[Wigley71] D.A. Wigley: Mechanical Properties of Materials at Low Temperatures, Plenum Press, New York, 1971.

[wikipedia1] http://en.wikipedia.org/wiki/Magnesium

[wikipedia2] http://en.wikipedia.org/wiki/Aluminium

[wikipedia3] http://en.wikipedia.org/wiki/Thorium

[Wonsiewicz67] B.C. Wonsiewicz, W.A. Backofen: Trans. AIME, *239*, 1967, p. 1422.

[Woodford69] D.A. Woodford: Trans. ASM, *62*, 1969, p. 291.

[Wray68] P.J. Wray, O. Richmond: J. Appl. Phys., *39*, 1968, p. 5754.

[Wray70] J.P. Wray: J. Appl. Phys., *41*, 1970, p. 3347.

[Yan03] F. Yan, K. Wu, G.L. Wu, B.L.Lee, M. Zhao: Mater. Letters, *57*, 2003, p. 1992.

[Yokoyama00] Y. Yokoyama, K. Fukaura, H. Sunada, R. Note, K. Hiraga, A. Inoue: Mater. Sci. Eng. A, *294-296*, 2000, p. 68.

[Yoo91] M.H. Yoo, J.K. Lee: Phil. Mag., *63*, 1991, p. 987.

[Young91] D.A. Young: Phase Diagrams of the Elements, University of California Press, Berkeley, 1991.

[Zaefferer] S. Zaefferer: JEOL News, 39, no.1, p. 10 or in electronic form http://www.jeol.com/jeolnews/391.pdf

[Zener44] C. Zener, J.H. Hollomon: Trans. ASM, *33*, 1944, p. 163.

[Zener44a] C. Zener, J.H. Hollomon: J. Appl. Phys., *15*, 1944, p. 22.

[Zou05] H. Zou, X. Zeng, C. Zhai, W. Ding: Mater. Sci. Eng. A, *392*, 2005, p. 229.